SEARCH FOR A LIGHT HIGGS BOSON AND LOW MASS DARK MATTER AT THE BELLE EXPERIMENT

A DISSERTATION SUBMITTED TO THE GRADUATE DIVISION
OF THE UNIVERSITY OF HAWAIʻI AT MĀNOA IN PARTIAL
FULFILLMENT OF THE REQUIREMENTS FOR THE DEGREE
OF

DOCTOR OF PHILOSOPHY

IN

PHYSICS

JULY 2017

By

Ilsoo Seong

Dissertation Committee:

Sven E. Vahsen, Chairperson
Thomas E. Browder
Jason Kumar
Philip von Doetinchem
Paul G. Lucey

Acknowledgements

I came to the University of Hawaii in 2011. Six years later, I finally got my doctorate in high energy physics. There were a lot of difficulties in this journey, but with the help of many people, I was able to withstand this moment. I am grateful to all people who have helped and supported me to this end.

First of all, I would like to thank my advisor, Prof. Sven Vahsen. His patience, advice from his experience, and knowledge of physics have helped me to deeply learn about physics. His enthusiasm in particle physics always encouraged and inspired me. It was an honor to work with him during my Ph.D. I would like to be a physicist like him in the future.

I would like to appreciate my lab colleagues Michael, Jeff, Tom, Dr. Peter, and Dr. Igal. I am grateful that I could study and discuss together. Especially, I want to give a special thank to our Berkeley team. The Berkeley trip was a wonderful and a useful experience. Maybe, we would have done better if we had less beer.

I am thankful to Prof. Robero Mussa and Prof. Tom Browder. I received useful advice to consider my thesis topic in various perspectives. And I also want to thank the Belle internal referees and people who helped me to solve issues on this study in the Belle collaboration.

I also want to thank Prof. Jason Kumar, Dr. Stengel, and Nicolas. The projects we have been done were a unique experience and helped me to understand much about my topic.

I have not been able to contact often since I left Korea, but I would like to thank Prof. Sun Kee Kim and Prof. Stephen Olsen. Without them, I would not have been able to start study in Hawaii. Experience in Seoul National University has helped me get started research right away in Hawaii.

I appreciate for supports from my family. I am able to reach here because my family is always sustained me. And I would like to tell my Father that I received my doctorate. Although I cannot show this moment, I deeply appreciate his faith in me. I could continue my studies because of his support. Thanks to my father.

Finally, I express my sincere gratitude to my wife, Jinhee Yoon. I can not put into words my gratitude for my wife. As I promised you, I will take you to the country you've long dreamed of. Jjaong!!

Abstract

We report a search for a light CP-odd Higgs boson A^0, which can be produced in Υ decays and decay to low mass dark matter, χ. We search for evidence of the on-shell process, $\Upsilon(1S) \rightarrow \gamma A^0$,$A^0 \rightarrow \chi\chi$, and the off-shell process, $\Upsilon(1S) \rightarrow \gamma\chi\chi$, via the dipion transition $\Upsilon(2S) \rightarrow \Upsilon(1S)\pi^+\pi^-$. We present the first Belle search for final states with a single photon and missing energy in the mass range of $M_{A^0} < 9.0$ GeV/c^2 and $M_\chi < 4.5$ GeV/c^2 with a data sample of 157.3×10^6 $\Upsilon(2S)$ decays. We find no evidence for a signal and set limits on branching fractions for such processes. We also use the limit on the off-shell process to set competitive limits on WIMP-nucleon scattering cross sections.

Contents

Acknowledgements iii

Abstract v

List of Tables ix

List of Figures x

1. Introduction 1

2. Dark matter 3

- 2.1. Observational evidence 3
  - 2.1.1. Galactic evidence 3
  - 2.1.2. Cosmic microwave background 7
- 2.2. Dark matter candidates 8
  - 2.2.1. Properties of dark matter 8
  - 2.2.2. Axions 8
  - 2.2.3. Weakly interacting massive particles 9
- 2.3. Detection of dark matter 11
  - 2.3.1. Direct detection 12
  - 2.3.2. Indirect detection 14
  - 2.3.3. Collider searches 16

3. CP-odd Higgs boson and low mass dark matter 18

- 3.1. Standard model 18
- 3.2. Supersymmetry 20
  - 3.2.1. Minimal sypersymmetric standard model 20
  - 3.2.2. Next-to-minimal sypersymmetric standard model 21

3.2.3. Low mass dark matter 22
3.3. Search for CP-odd Higgs boson and low mass dark matter 23

4. **The Belle experiment** **25**
4.1. The KEKB accelerator 25
4.2. The Belle detector 27
4.2.1. Silicon vertex detector (SVD) 28
4.2.2. Central drift chamber (CDC) 32
4.2.3. Aerogel Čherenkov counter (ACC) 33
4.2.4. Time-of-flight counter (TOF) 35
4.2.5. Electromagnetic calorimeter (ECL) 37
4.2.6. K_L and muon detector (KLM) 38
4.3. Trigger system 40
4.3.1. Level 1 (L1) trigger 41
4.3.2. Level 3 (L3) trigger 43
4.3.3. Level 4 (L4) trigger 43

5. **Data analysis** **45**
5.1. Data samples 46
5.1.1. $\Upsilon(2S)$ experimental data 46
5.1.2. Monte Carlo simulation of signal events 46
5.1.3. Monte Carlo simulation of $\Upsilon(2S)$ decays 47
5.1.4. $\Upsilon(4S)$ off-resonance data 49
5.2. Trigger selection 49
5.2.1. Trigger efficiency 50
5.3. Event selection 54
5.3.1. Initial selection 54
5.3.2. Particle identification and photon selection 55
5.4. Background suppression 56
5.4.1. Di-pion selection 56
5.4.2. Photon vetos 56
5.4.3. K_L veto 58
5.4.4. Remaining backgrounds 60
5.5. Signal efficiency 66
5.6. Probability density functions 69
5.6.1. Recoil mass PDF 69
5.6.2. Photon energy PDF 71

5.7. Determination of branching fractions 80

5.7.1. Yield Extraction 80

5.7.2. Limit Calculation 80

5.7.3. Results of the fits to MC 81

5.7.4. Fit to experimental data 81

5.8. Systematic uncertainties 90

6. Conclusion and implication 94

6.1. Upper limits on branching fractions 94

6.2. WIMP-nucleon cross section limit 94

A. Decay table for the $\Upsilon(2S)$ inclusive MC sample 101

B. Figure of merits for the selection 103

C. Photon energy spectrum for the signal MC samples 106

C.1. On-shell signal sample 106

C.2. Off-shell signal sample 108

D. Results of fit bias test 110

D.1. Fit bias for the on-shell signal 111

D.2. Fit bias for the off-shell signal 112

Bibliography 114

List of Tables

3.1. Summary of previous invisible decay searches with a single photon final state. 24

4.1. Comparison of SVD1 and SVD2. 31

4.2. Total cross section and typical Belle trigger rates at $\mathscr{L} = 10^{34}$ cm^{-2} s^{-1}. 40

5.1. The dominant L1 triggers in this analysis 49

5.2. Estimated number of background in the signal region 65

5.3. Summary of selection with N-1 efficiency 67

List of Figures

1.1. Feynman diagram for physics process of interest. 1

2.1. Rotation curve for the galaxy NGC6503. The dotted, dashed, and dashed-dotted lines are contributions from the gas, disk, and dark matter halo, respectively. The black dots are the measured rotational velocities as a function of distance from the center of the galaxy. . . . 4

2.2. Composite image of the galaxy cluster known as the Bullet Cluster. Gravitational lensing measurements determine the mass map shown in blue. X-ray observations by Chandra indicates the hot gas component shown in pink. 5

2.3. The temperature anisotropies of the CMB as observed by the Plank Collaboration 6

2.4. The temperature angular power spectrum of the CMB detected by Planck at different multipole moments corresponding to various angular scales on the sky. 6

2.5. Comoving number density Y and thermal relic density Ω_X as a function of temperature T and time t. The solid black line is for an annihilation cross section that produces the observed relic density, while the shaded regions are for cross sections that differ by 1, 2, and 3 orders of magnitude. 10

2.6. Diagram for the unknown interaction of two dark matter and two standard model particles. The blue arrows indicate the direction of time for each dark matter detection method. 12

2.7. WIMP-nucleon spin-independent (top) and spin-dependent (bottom) cross section limits. 15

3.1. The standard model of elementary particles 19

4.1. The KEKB accelerator. 26

4.2. Cross section for inclusive production of the Υ resonances. 27

4.3. Integrated luminosity of B factories. 28

4.4. The Belle detector. 29

4.5. Silicon vertex detector (SVD). 30

4.6. Impact parameter resolution of SVD1 (reversed triangle) and SVD2 (triangle) in the r-ϕ plane (left) and the z direction (right). 31

4.7. Overview of the central drift chamber (CDC). 32

4.8. Measured mean of dE/dx versus momentum for different particles. . 34

4.9. Aerogel Čherenkov counter (ACC). 35

4.10. Calculated masses of π, p, and K from TOF measurement for particle momenta below 1.2 GeV/c. 36

4.11. Geometry of the electromagnetic calorimeter (ECL). 37

4.12. Cross section of a RPC superlayer in the KLM detector. 39

4.13. Overview of the trigger system 41

4.14. Schematic of the Level-1 trigger system 42

5.1. Generated photon energy spectra in the $\Upsilon(1S)$ frame. (a): on-shell process $M_{A^0} = 0.1$ GeV/c^2 (red) and 9.2 GeV/c^2 (green). (b): off-shell process $M_\chi = 0.1$ GeV/c^2 (blue) and 4.5 GeV/c^2 (magenta). 48

5.2. Relative efficiency of hie (a) and e_had (b) as a function of E_{ECL}^{trg}. Black dots are experimental data and red open-squares and green open-triangles are MC events with and without beam background contribution in the triggers, respectively. 51

5.3. Trigger efficiency versus energy deposit on the ECL for $M_\chi = 0.1$ GeV/c^2. Green circles show the L1 trigger efficiency and red dots show the total trigger efficiency with L1 and L4 triggers. 52

5.4. Trigger efficiency as a function of E^*_γ. Black filled-squares and green open-squares are the $\epsilon_{\text{trig}}(E^*_\gamma)$ of using the two trigger and all triggers, respectively. 53

5.5. Angular distributions for signal MC and background events. (a): opening angle between the two pion candidates in the $\Upsilon(1S)$ frame, (b): Bremsstrahlung photon distribution, (c): azimuthal angle difference between the dipion system and a photon. The dotted vertical red line indicates the cut values, and the arrow shows which events are kept by the cut. 57

5.6. E^{2*}_γ versus E^*_γ distribution. The red dashed line indicates our selection. 59

5.7. Remaining energy deposited in ECL versus E^*_γ distribution. The red dashed line indicates our selection. 59

5.8. $|\Delta\phi_{\gamma N}|$ distribution for the neutral particle candidate. (a): absolute azimuthal angle difference versus $|\Delta\phi_{\gamma N}|$ with $\Upsilon(1S) \to \gamma K^0_L K^0_L$ MC, (b): 1D histogram for signal MC, (c): for exclusive background MC. . 61

5.9. Optimization of K_L veto with $M_{A^0} = 0.1$ GeV. Instead of using exclusive background MC samples, $\Upsilon(2S)$ inclusive MC and $\Upsilon(4S)$ off-resonance data are used. Left: Figure of Merit, right: signal efficiency as a function of $|\Delta\phi_{\gamma N}|$. 62

5.10. Categorized remaining backgrounds, estimated from 400 million $\Upsilon(2S)$ inclusive MC events. Left: photon energy spectrum in the $\Upsilon(1S)$ frame. Right: $\Upsilon(1S)$ recoil mass distribution. 63

5.11. Distributions for the photon energy spectrum in $\Upsilon(1S)$ frame (left) and the $\Upsilon(1S)$ recoil mass (right) from $\Upsilon(4S)$ off-resonance data. . . . 63

5.12. Invariant mass distributions with loose recoil mass selection. (a): $M_{\pi\pi}$ distribution, (b): $M_{\pi\pi\gamma}$ distribution, (c): $M_{\pi\pi\gamma}$ vs. E^*_γ 64

5.13. Reconstruction efficiency for the on-shell and the off-shell process versus M_{A^0} and M_{χ}, respectively, after all selections. Black filled-squares and green open-squares are the efficiency when using two triggers and using all triggers, respectively. Red solid lines are the Spline functions used for interpolation. 68

5.14. Recoil mass distribution with PDF for the signal and background from $\Upsilon(1S)$ decays. Top: linear scale, bottom: log scale. 70

5.15. Continuum background PDF in the recoil mass distribution. 71

5.16. Photon energy spectrum with a CB PDF for $M_{A^0} = 0.1$ GeV. Top: log scale, bottom: linear scale. 73

5.17. Photon energy spectrum with a CB PDF for $M_{A^0} = 8.5$ GeV. Top: log scale, bottom: linear scale. 74

5.18. Dependence of Crystal Ball (CB) parameters on M_{A^0}. (a) The mean of the Gaussian term in the CB function, (b) the sigma of the Gaussian term , (c) the cutoff term of the CB tail, and (d) the power-law of the CB tail. 75

5.19. The off-shell signal PDF with the $M_{\chi} = 0.1$ GeV (top) and 4.0 GeV (bottom). 76

5.20. Dependence of the off-shell signal PDF parameters on M_{χ}. (a) s, the slope parameter, (b) β, the cutoff term, (c) k ($s' = k \cdot s$), the relative slope parameter, and (d) β', the second cutoff term. 77

5.21. Photon energy spectrum of background samples. Left: $\Upsilon(1S)$ leptonic decays, right: $\Upsilon(1S)$ hadronic decays. 78

5.22. Photon energy spectrum of continuum background. 79

5.23. The results of unbinned likelihood fit to the mixed events with the $\Upsilon(2S)$ inclusive MC events and $\Upsilon(4S)$ off-resonance experimental data. 82

5.24. An example of the result of likelihood as a function of signal yield at $M_{A^0} = 2.0$ GeV ($E^{*}_{\gamma} \approx 4.5$ GeV). 83

5.25. Expected upper limits for the branching fractions at 90% C.L. 84

5.26. Recoil mass distribution with a loose selection (top). The sideband regions are defined as $9.415 < M_{recoil} < 9.44$ GeV/c^2 and $9.485 < M_{recoil} < 9.51$ GeV/c^2 shown in green and the signal region is shown in blue. Photon energy spectrum of continuum background from the sideband regions (bottom). 85

5.27. An example of the fit results in the experimental data with M_{A^0}=2.946 GeV signal: M_{recoil} (top) and E^*_γ (bottom) distribution. The fitted lines are continuum backgrounds (cyan dashed line), $\Upsilon(1S)$ decay backgrounds (magenta dashed line), and the on-shell signal (red dashed line), which corresponds to the 2.078σ significance. 86

5.28. An example of the fit results in the experimental data with M_{A^0}=8.487 GeV signal: M_{recoil} (top) and E^*_γ (bottom) distribution. The fitted lines are continuum backgrounds (cyan dashed line), $\Upsilon(1S)$ decay backgrounds (magenta dashed line), and the on-shell signal (red dashed line), which corresponds to the 2.067σ significance. 87

5.29. Results of comparison between experimental and pseudo-experimental data with all triggers. Black dots are $\Upsilon(2S)$ on-resonance data and filed histograms are pseudo-experimental data, which is mixed with the $\Upsilon(4S)$ off-resonance (green) and $\Upsilon(2S)$ inclusive MC sample (red) 88

5.30. Results of comparison between experimental and pseudo-experimental data with all triggers. Black dots are $\Upsilon(2S)$ on-resonance data and filed histograms are pseudo-experimental data, which is mixed with the $\Upsilon(4S)$ off-resonance (green) and $\Upsilon(2S)$ inclusive MC sample (red) 89

5.31. Measured N_{sig} from toy MC as a function of input N_{sig}. Black dashed line shows the expected value and red solid line is the linear fit result. Left: for $M_{A^0} = 0.1$ and right: 9.0 GeV. 92

5.32. Average fit bias for the on-shell signal (top) and the off-shell (bottom). 93

6.1. 90% C.L. upper limits on the BFs for $\Upsilon(1S) \to \gamma A^0, A^0 \to \chi^0\chi^0$ (left) and $\Upsilon(1S) \to \gamma\chi^0\chi^0$ process (right). Blue dashed lines are the results of Babar and orange solid lines and dash-dotted purple lines are the Belle limits with and without including the systematic uncertainty. . 95

6.2. Belle 90% C.L. upper limits on the BFs for $\Upsilon(1S) \to \gamma A^0, A^0 \to \chi^0\chi^0$ (left) and $\Upsilon(1S) \to \gamma\chi^0\chi^0$ process (right). 95

6.3. Zoomed plot of the 90% C.L. upper limit on the BF for $\Upsilon(1S) \to \gamma A^0, A^0 \to \chi^0\chi^0$ in the M_{A^0} region of 6 - 9.5 GeV. Blue dashed lines are the results of Babar and orange solid lines and dash-dotted purple lines are the Belle limits with and without including the systematic uncertainty. 96

6.4. Lower limit on the mediator scale Λ as a function WIMP mass M_χ. . 97

6.5. WIMP-nucleon spin-independent scattering cross-section limit at 90% C.L. 98

6.6. Belle II prospects for WIMP-nucleon spin-independent scattering cross-section limit at 90% C.L. 99

6.7. Belle II prospects for WIMP-nucleon spin-dependent scattering cross-section limit at 90% C.L. 100

B.1. Figure of Merit and efficiency with N-1 calculation for $M_{A^0} = 0.1$ GeV/c^2. The rows are listed as follows: the FOM, $\Upsilon(4S)$ off-resonance data, the $\Upsilon(2S)$ inclusive MC sample, the signal sample, and the efficiency of the signal sample. 104

B.2. Figure of Merit and efficiency with N-1 calculation for $M_{A^0} = 9.2$ GeV/c^2. The rows are listed as follows: the FOM, $\Upsilon(4S)$ off-resonance data, the $\Upsilon(2S)$ inclusive MC sample, the signal sample, and the efficiency of the signal sample. 105

C.-2. Photon energy spectrum with the final PDF for the off-shell production 109

D.1. Results of toy MC for the on-shell signal 111

D.2. Results of toy MC for the off-shell signal 112

Chapter 1

Introduction

The present understanding of the universe suggests that more than 73% of its energy density is in the form of dark energy, about 23% is dark matter, and only a remaining fraction, below 4%, is ordinary matter. Unknown form of dark energy and dark matter components are an important missing part in our understanding of the universe. It is a challenging goal of modern particle physics to reveal their nature.

A primary interest in this thesis is a search for a particle type dark matter candidate, especially a low mass dark matter particle. In the following thesis, searches for low mass dark matter particles, χ, and CP-odd Higgs boson, A^0, at the electron-positron collider experiment, Belle, are described. The CP-odd Higgs boson is required as a mediator to produce dark matter particles from standard model particles as shown in the Feynman diagram in Figure 1.1.

This thesis presents two approaches to search for dark matter particles and CP-odd Higgs boson: the on-shell process, $\Upsilon(1S) \to \gamma A^0, A^0 \to \chi\chi$, and the off-shell process, $\Upsilon(1S) \to \gamma\chi\chi$, via the dipion transition $\Upsilon(2S) \to \Upsilon(1S)\pi^+\pi^-$. We find no

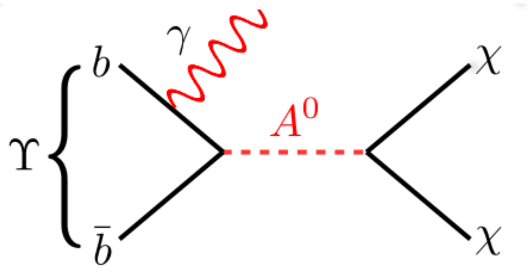

Figure 1.1.: Feynman diagram for physics process of interest.

evidence for a signal and set limits on branching fractions for such processes. The limit on the off-shell process is also interpreted to limits on dark matter and nucleon scattering cross section.

In this thesis, we begin with observational evidence for the existence of dark matter, popular dark matter candidates, and detection methods of dark matter particles. In Chapter 3, we introduce brief features of the standard model of particle physics and extensions of the standard model. This chapter also presents previous searches at different experiments. Next, in Chapter 4, the Belle experiment is described. Details of method to search for low mass dark matter particles and a CP-odd Higgs boson are shown in Chapter 5. Limits on branching fractions for two processes and a limit on dark matter nucleon scattering cross section are presented in Chapter 7.

Chapter 2

Dark matter

Dark matter is a long-standing unsolved problem in astronomy and particle physics. There is much observational evidence to indicate the existence of dark matter, which is a form of non-luminous matter in the universe. We know few facts about dark matter: it makes up 85% of the matter energy density of the universe, and it does not interact with the electromagnetic force. These facts make dark matter a mystery and an unsolved problem. This chapter describes evidence for the existence of dark matter, and candidates that are consistent with the evidence.

2.1. Observational evidence

2.1.1. Galactic evidence

The first observational evidence for dark matter was provided in 1933 by the astronomer Fritz Zwicky [1]. He used Doppler shifts to measure the velocities of galaxies moving toward the center of the Coma cluster. The cluster mass was estimated with the virial theorem, which provides the relation between the average total kinetic energy and gravitational potential energy, and it had to be much larger than the observed mass. Since the observed mass is estimated from the observed luminous matter, he concluded that the Coma cluster contains more non-luminous *dark* matter than luminous.

In a similar way, rotation curves of galaxies are widely recognized as evidence for the existence of dark matter. The Doppler shifts of the spectral lines from galaxies

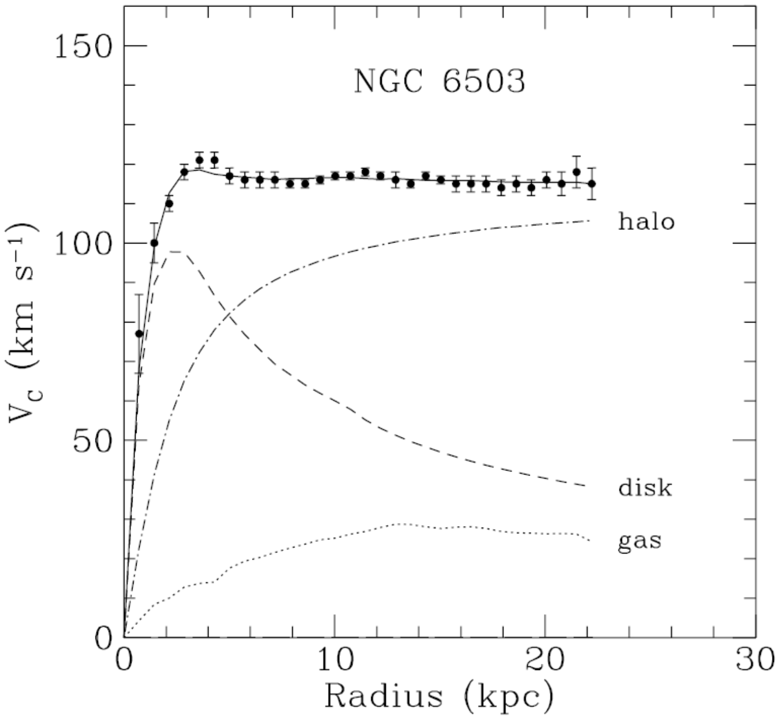

Figure 2.1.: Rotation curve for the galaxy NGC6503 from [2]. The dotted, dashed, and dashed-dotted lines are contributions from the gas, disk, and dark matter halo, respectively. The black dots are the measured rotational velocities as a function of distance from the center of the galaxy.

as a function of radius from the center of a galaxy have been used to measure the rotational velocities of galaxies, which have revealed that the rotational velocity curves are nearly constant at high radii, as shown in Figure 2.1. The circular motion of stars in a galaxy should have rotational velocities that scale as

$$v \propto \sqrt{\frac{M(r)}{r}}\,, \tag{2.1}$$

where r is the radius from the center of a galaxy and $M(r)$ is the enclosed mass within the radius r. Thus, if most of the luminous matter is contained within a radius of r_0, the velocities should fall off with increasing $r > r_0$. However, the observations yield velocity curves which remain flat even for the outermost luminous matter. This can be explained by the presence of a halo of dark matter surrounding the disk of visible matter in the galaxy.

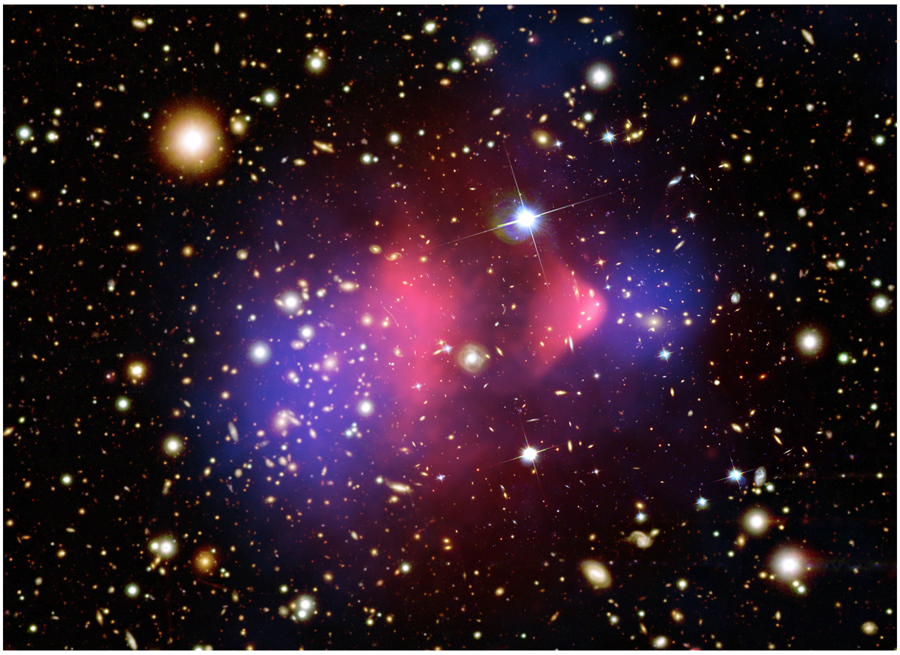

Figure 2.2.: Composite image of the galaxy cluster known as the Bullet Cluster. Gravitational lensing measurements determine the mass map shown in blue. X-ray observations by Chandra indicates the hot gas component shown in pink. From [?, 3].

Another famous sign of the presence of dark matter is provided by the Bullet Cluster [?,3], which is made up of two colliding clusters of galaxies. When two galaxy clusters merge, the gas clouds which consist of ordinary matter become extremely hot by colliding each other. It causes the hot gas clouds to decelerate and to emit more X-rays, which are used to determine where the ordinary matter is located. Gravitational lensing is the effect of gravity which acts as a lens due to bending of the path of light by any mass. Weak gravitational lensing makes distorted images that allow us to infer the distribution of the total cluster mass, including both dark matter and ordinary matter. Figure 2.2 shows an optical image of the Bullet Cluster with the observations of X-rays (pink) and gravitational lensing (blue) superimposed, and it shows that the mass distributions are clearly separated from the gas clouds. This provides the evidence that the majority of the mass in the clusters consists of dark matter, which is non-luminous and collisionless.

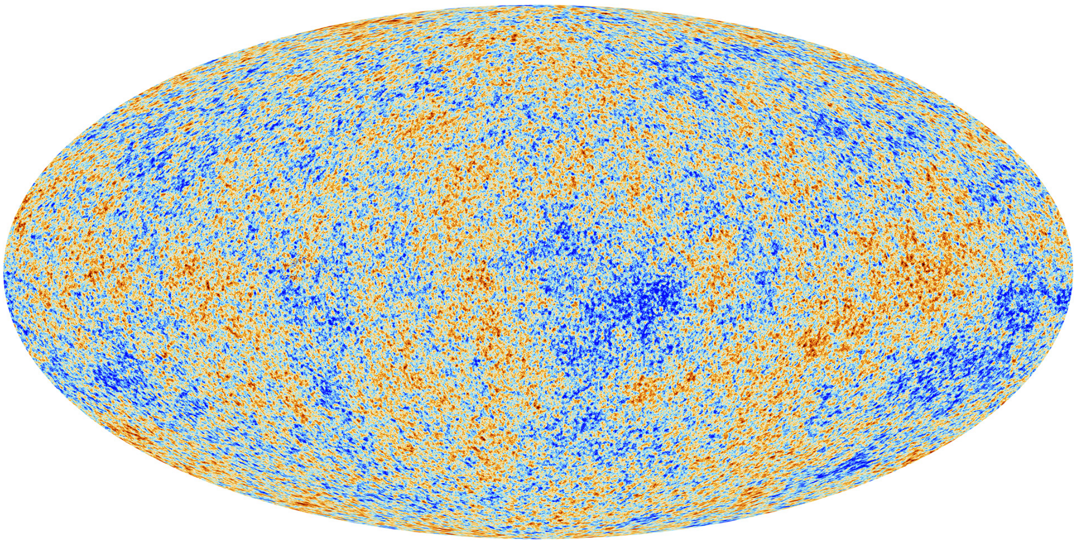

Figure 2.3.: The temperature anisotropies of the CMB as observed by the Planck Collaboration (Image from ESA and the Planck Collaboration).

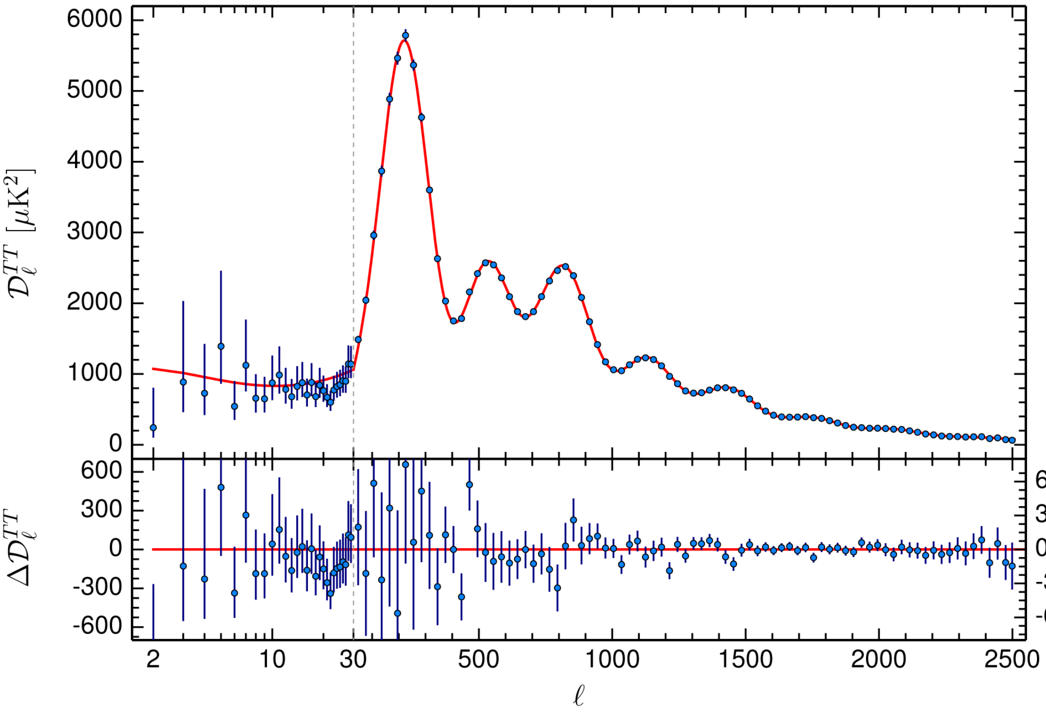

Figure 2.4.: The temperature angular power spectrum of the CMB detected by Planck at different multipole moments corresponding to various angular scales on the sky. From [4].

2.1.2. Cosmic microwave background

The cosmic microwave background (CMB) radiation provides precise measurements of energy densities in the universe. After the Big Bang, the universe was extremely hot and dense; the existing matter was a plasma. As the universe expanded, its density and temperature eventually dropped below the ionization energy of atoms. This allowed the matter to recombine into neutral atoms, hence this is called the epoch of recombination. This enabled photons to travel freely, without interacting with the matter. Such photons are observed today as the CMB radiation. These photons reach us from all directions and carry a snapshot of the universe at the time of last scattering. Figure 2.3 shows an all-sky map of the CMB as observed by the Planck Collaboration [4, 5]. The color in the map represents different temperatures as cold blue spots and warm red spots. The fluctuations in the temperature are tiny, of the order of 10^{-5}. This small non-uniformity in the temperature is the result of variations in the matter density. The universe has voids between galaxies and clusters, and photons can travel more freely in the void regions. Areas with lower density than their surroundings would be measured in the CMB as cold spots.

The temperature anisotropies can be separated by the angle and quantified using spherical harmonics as shown in Figure 2.4. The resulting angular power spectrum quantifies the variance of temperature fluctuations in the sky, as a function of the multipole moment l, which corresponds to inverse angular scale. The red curve shown in the power spectrum represents the best-fit of the standard model of cosmology, the Λ Cold Dark Matter (ΛCDM) model, and the fitted result determines the cosmological parameters. The position of the first peak corresponds to the curvature of the universe, is consistent with a flat universe. The ratio of amplitudes between the first and second peaks tells us the ordinary matter density. If we raise the dark matter density, then the amplitude of the first peak becomes smaller. In 2015, the Planck collaboration released the following parameter values:

$$\Omega_b h^2 = 0.02226 \pm 0.00023 \tag{2.2}$$

$$\Omega_c h^2 = 0.1186 \pm 0.0020\,, \tag{2.3}$$

where $\Omega_b h^2$ is the ordinary matter density, $\Omega_c h^2$ is the dark matter density, and h is the reduced Hubble constant $h = H_0/(100\text{ km s}^{-1}\text{Mpc}^{-1}) = 0.678$. The uncertainties are shown at 68% confidence. These results tell us that approximately 84% of the matter in the universe is composed of dark matter.

2.2. Dark matter candidates

2.2.1. Properties of dark matter

The first conclusion derived from the previous section is that dark matter has to be massive as we observe its gravitational effects in the galaxies and clusters. It also has to be *dark*, which means that it carries no electric charge and interacts very weakly both with itself and with ordinary matter, as we see from the Bullet Cluster. The CMB results imply that dark matter has to be stable, which means its lifetime should be long enough to survive from the Big Bang until today.

There are a few dark matter candidates with such properties. Dark matter could consist of a single type of particle, multiple particle types, or astronomical objects. The astronomical objects could be massive astrophysical compact halo objects (MACHOs) [6, 7] or primordial black holes [8]. Both are composed of ordinary matter that emits very little to no radiation, while particle dark matter candidates are made up of non-ordinary matter particles. In this thesis, we will only focus on particle candidates for dark matter, such as sterile neutrinos [9], axions, and weakly interacting massive particles (WIMPs). These are hypothetical particles that are thought to constitute some, or all of, the dark matter. Properties of dark matter are limited by the cosmological constraints discussed above. These constraints may rule out sterile neutrinos as a dark matter candidates due to their limited mass range below 10 keV/c^2 [10]. However, sterile neutrinos could contribute warm dark matter instead of *cold* dark matter, as in the widely accepted ΛCDM model. Cold means that particles move relatively slowly compared to the speed of light, i.e. they are non-relativistic. In this thesis, we will focus on cold dark matter candidates; axions and WIMPs.

2.2.2. Axions

The axion is an attractive dark matter candidate because it was proposed to solve the strong CP problem [11, 12], not the dark matter problem. The weak interaction in the standard model of particle physics violates charge-parity CP symmetry, but the strong interaction seems to obey CP symmetry. There is no a priori reason the strong interaction should be CP conserving, but it has not been experimentally observed and has to be very small. This is a naturalness problem in the standard model, and known as the strong CP problem. The original axion was ruled out a long time ago by experiment, however *invisible* axion models [13–16] are still viable. As its name implies, it is effectively collionless with ordinary matter. The mass of the axion is determined by a single factor, the scale f_a of symmetry breaking, and is given by

$$m_a \simeq 0.60 \text{ eV} \frac{10^7 \text{ GeV}}{f_a} \; . \tag{2.4}$$

There are astrophysical and cosmological constraints that give the limit $10^9\,\text{GeV} \leq f_a \leq 10^{12}\,\text{GeV}$, which corresponds to $10\,\mu\text{eV/c}^2 \leq m_a \leq 1\,\text{meV/c}^2$ [17]. Despite having an extremely small mass, axion dark matter would be non-relativistic, unlike neutrinos. Axions may have been created by non-thermal processes in the early universe; axions couple very weakly to other matter and hence may not have thermalized. Thus they can have with non-relativistic speeds.

2.2.3. Weakly interacting massive particles

WIMPs represent a class of dark matter candidates that interact with ordinary matter only via gravity and standard model weak interactions. In the standard model (SM) of particle physics, the only weakly interacting particles are neutrinos. None of the SM particles are good candidates for dark matter, thus modification of the SM is required to account for dark matter.

In the early universe, the WIMPs were in thermal equilibrium with SM particles. As the universe expanded, and the temperature became smaller than the WIMP mass, the WIMPs could only annihilate and no longer be produced. This is because that the number density of non-relativistic particles in equilibrium decreases exponentially with decreasing temperature, due to the Boltzmann factor. As the universe expanded more, the WIMPs could not annihilate anymore either, because they became very rare. At that point the number density of WIMPs in a comoving volume approached a constant *relic density*. This is known as the freeze-out mechanism shown in Figure 2.5 [18].

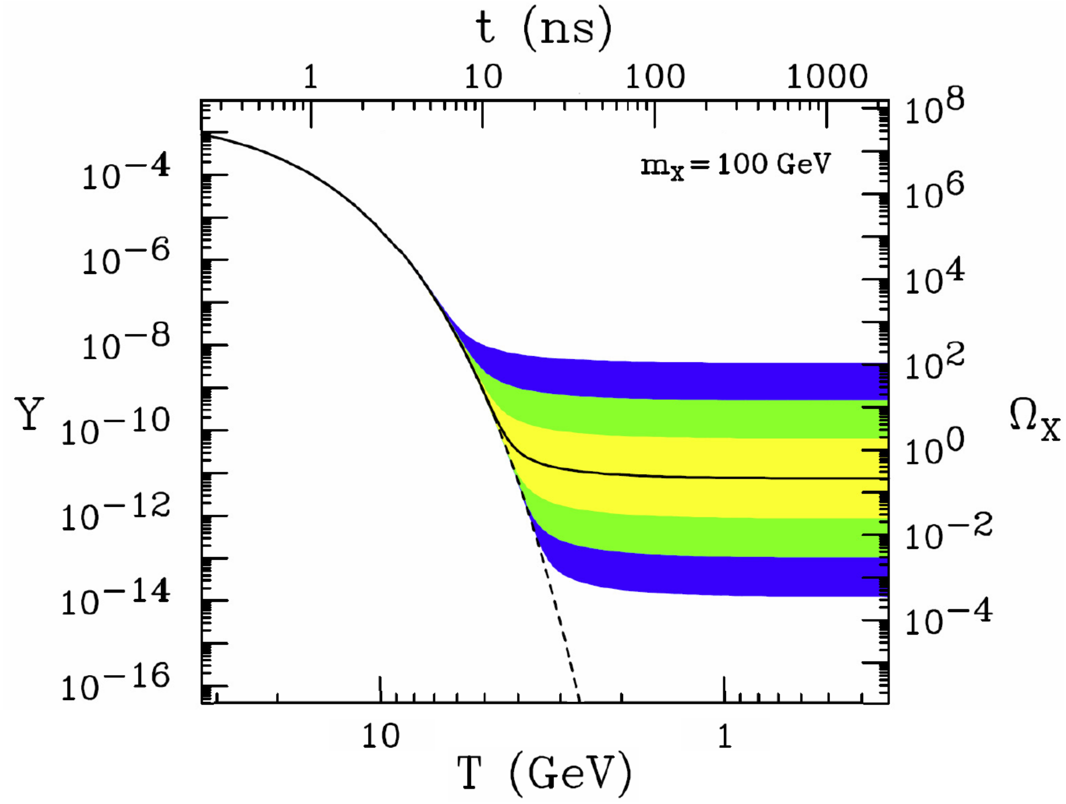

Figure 2.5.: Comoving number density Y and thermal relic density Ω_χ as a function of temperature T and time t. The solid black line is for an annihilation cross section that produces the observed relic density, while the shaded regions are for cross sections that differ by 1, 2, and 3 orders of magnitude. From [18].

The evolution of the number density over time can be described by the Boltzmann equation:

$$\frac{dn_\chi}{dt} = -3\,H\,n_\chi - \langle\sigma_{\text{ann}}v\rangle\left((n_\chi)^2 - (n_\chi^{eq})^2\right) \tag{2.5}$$

where n_χ is the WIMP number density, n_χ^{eq} is the equilibrium number density, H is the Hubble expansion rate, and $\langle\sigma_{\text{ann}}v\rangle$ is the thermally averaged annihilation cross section for the WIMP. The first term on the right hand side corresponds to the expansion of the universe, the second term to the WIMP annihilation process. The second term has to vanish in equilibrium. n_χ^{eq} decreases exponentially as the universe expands, thus freeze-out occurs when the universe expansion rate is comparable to the annihilation rate, $3H = \langle\sigma_{\text{ann}}v\rangle n_\chi$. The thermal relic energy density is approximately given by

$$\Omega_\chi h^2 \simeq const \cdot \frac{T_0^3}{M_{Pl}^3 \langle \sigma_{\rm ann} v \rangle} \simeq \frac{0.1 \text{ pb} \cdot \text{c}}{\langle \sigma_{\rm ann} v \rangle} \,, \tag{2.6}$$

where T_0 is the current CMB temperature, M_{Pl} is the Planck mass, and c is the speed of light. As shown in equation 2.6, smaller annihilation cross sections correspond to higher relic densities. From the measured value of $\Omega_\chi h^2$, we can estimate

$$\langle \sigma_{\rm ann} v \rangle \simeq 3 \times 10^{-26}\, \text{cm}^3/\text{s}\,. \tag{2.7}$$

Using dimensional analysis, the annihilation cross section for a WIMP can be written as

$$\sigma_{\rm ann} = k \frac{g_{weak}^4}{16\pi^2 m_\chi^2} \,, \tag{2.8}$$

where $g_{weak} \simeq 0.65$ is the weak gauge coupling, k is a model-dependent fudge factor, and m_χ is the WIMP mass. Assuming a WIMP mass around the electroweak scale, $m_\chi \sim$ 100 GeV, gives $\langle \sigma_{\rm ann} v \rangle \sim 10^{-26}$ cm^3/s. This agrees with the estimate in equation 2.7, which was based only on cosmological expansion, thermodynamics, and a general annihilation process. The fact that WIMPs provide the observed relic density is known as the "WIMP miracle". However, equation 2.8 is not quantitatively precise, it can be satisfied with WIMP masses from 1 GeV to 1 TeV.

WIMP candidates can be found in many extensions of the SM of particle physics. The most well motivated WIMP candidate is the lightest superparticle (LSP) in supersymmetry models. We will discuss this WIMP candidate in Chapter 3.

2.3. Detection of dark matter

The primary candidate for particle dark matter (DM) considered here is the WIMP. To determine the properties of the WIMP, such as its mass or cross sections, we have to detect it by experiment. WIMP searches can be divided into three categories: direct, indirect, and collider searches. Figure 2.6 illustrates the three detection processes: direct detection experiments are designed to observe events where WIMPs scatter off nuclei in detectors, and indirect detection experiments seek products of WIMP annihilation, such as gamma rays, neutrinos, positrons, or antiprotons.

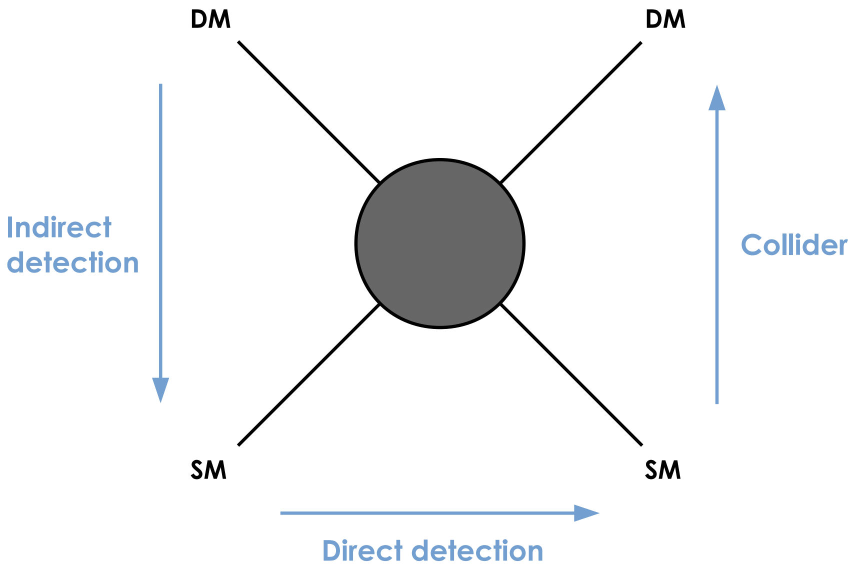

Figure 2.6.: Diagram for the unknown interaction of two dark matter and two standard model particles. The blue arrows indicate the direction of time for each dark matter detection method.

Collider experiments aim to produce WIMPs by colliding SM particles. We will briefly discuss these three detection methods.

2.3.1. Direct detection

Since DM is present in the galactic halo, it should pass through Earth continuously. The expected interaction rate is low due to the small scattering cross section. Inelastic scattering, which excites nuclear states, is expected to account for only a small part of the total cross section. Thus most direct detection experiments aim to detect nuclear recoils from elastic scattering of WIMPs on target nuclei. The low expected detection rate necessitates long exposure times, which makes direct detection experiments sensitive to backgrounds. The detectors are placed in underground laboratories to suppress backgrounds from cosmic rays. Generally, the experiments measure the nuclear recoil energy deposited in the detectors following the elastic scattering. The energy of recoiling nuclei converts into scintillation light, ionization energy, and thermal energy; the detectors record this converted energy, of the order of keV, using various techniques. Using the recoil energy and event rate information direct detection experiments estimate WIMP-*nucleon* scattering cross sections and mostly have set limits so far.

The differential elastic scattering rate per unit detector mass, time, and recoil energy is given by [19]

$$\frac{dR}{dE_R} = \frac{\sigma_0\,\rho_0}{2m_\chi\,\mu_N^2}\,F^2(E_R)\,\int_{v_{min}}^{v_{esc}} \frac{f(v)}{v}\,dv\ , \tag{2.9}$$

where E_R is the target nucleus recoil energy, σ_0 is the total WIMP-*nucleus* cross section at the zero momentum transfer limit, ρ_0 is the WIMP energy density, m_χ is the WIMP mass, $\mu_N = m_N m_\chi/(m_N + m_\chi)$ is the reduced mass of the WIMP and nucleus, v and $f(v)$ are the WIMP velocity and velocity distribution in the Earth frame, and $F(E_R)$ is the elastic nuclear form factor. The total cross section σ_0 depends on the coupling of WIMPs to nucleons. It can be separated into a spin-independent (SI) and a spin-dependent (SD) contribution.

For SI interactions, σ_0 can be written as

$$\sigma_0^{SI} = \frac{4\,\mu_N^2}{\pi}\,[Zf_p + (A-Z)f_n]^2\,, \tag{2.10}$$

where Z is the number of protons, A is the number of total nucleons, and f_p and f_n are the effective coupling constants of WIMPs to protons and neutrons, respectively. For most cases, we can assume isospin conservation, which is $f_p \simeq f_n$, then equation 2.10 can be rewritten as

$$\sigma_0^{SI} = \frac{4\,\mu_N^2}{\pi}\,A^2 f_p^2 = A^2\,\frac{\mu_N^2}{\mu_p^2}\,\sigma_p^{SI}\,, \tag{2.11}$$

where $\sigma_p^{SI} = \frac{4\,\mu_p^2}{\pi}\,f_p^2$ is the WIMP-*nucleon* cross section normalized to a single proton and μ_p is the reduced mass of the WIMP and proton. Direct search experiments conventionally use σ_p^{SI} to compare experiments using different targets. The SI event rate scales with the square of the number of nucleons, A. This means that heavier nuclei will produce a higher event rate than lighter nuclei and will allow searches for lower WIMP-nucleon cross sections. For SD interactions, σ_0 is given by

$$\sigma_0^{SD} = \frac{32}{\pi}\,G_F^2\,\mu_N^2\,\frac{(J+1)}{J}[a_p\langle S_p\rangle + a_n\langle S_n\rangle]^2\,, \tag{2.12}$$

where G_F^2 is the Fermi coupling constant, J is the total spin of the target nucleus, a_p and a_n are the effective SD WIMP couplings on protons and neutrons, and $\langle S_p \rangle$ and $\langle S_n \rangle$ are the expectation values of the proton and neutron spins within the nucleus. In contrast to the SI cross section, the SD cross section does not depend on A and it vanishes for zero total nuclear spin. Therefore, most experiments are more sensitive to the SI cross section than the SD cross section.

A large number of experiments search for signals from WIMP-nucleon scattering. Figure 2.7 shows the current status of direct detection experiments. The solid lines are exclusion limits and the closed contours are possible signal regions reported by DAMA/LIBRA [20], CoGeNT [21], CRESST II [22], and CDMS II (Si) [23]. The XENON 1T [24] and LUX [25] experiments currently provide the strongest constraints on spin-independent scattering. These experiments use liquid xenon targets and achieve a sensitivity of the order of 10^{-46} cm^2. These limits disfavor the signal claims in the SI elastic scattering framework. PICO-60L [26] is the leading experiment for spin-dependent scattering. The PICO experiment uses a bubble chamber of C_3F_8 and obtains a sensitivity of the order of 10^{-40} cm^2.

The lower limit of the integration in the differential scattering rate, equation 2.9, is given by the minimal velocity $v_{min} = \sqrt{m_N E_R/(2\mu_N^2)}$, which depends on the minimum detectable recoil energy, E_R. This means that experiments are limited by detector performance. Light WIMPs, with mass of the order of 10 GeV/c^2, induce small recoil energies, of the order of 1 keV, and most experiments are not sensitive in this region due to their energy threshold.

2.3.2. Indirect detection

DM particles may be bound in the center of the galactic halo, the Sun, or black holes because of the strong gravitational field. They could interact with each other in these locations, and if DM particles are WIMPs, they might annihilate into gamma rays, neutrinos, positrons, or antiprotons. Indirect detection experiments search for excesses of these annihilation products in the flux of cosmic rays. The primary cosmic rays include mainly matter particles like protons, hence it is difficult to observe the matter induced by the WIMP annihilation. Hence antimatter such as positrons or antiprotons from outer space is a good probe to search for DM annihilation. The detectors measure a diffuse spectrum because of the galactic magnetic field. Also, these particles are affected by the magnetic field of the Sun, therefore the solar

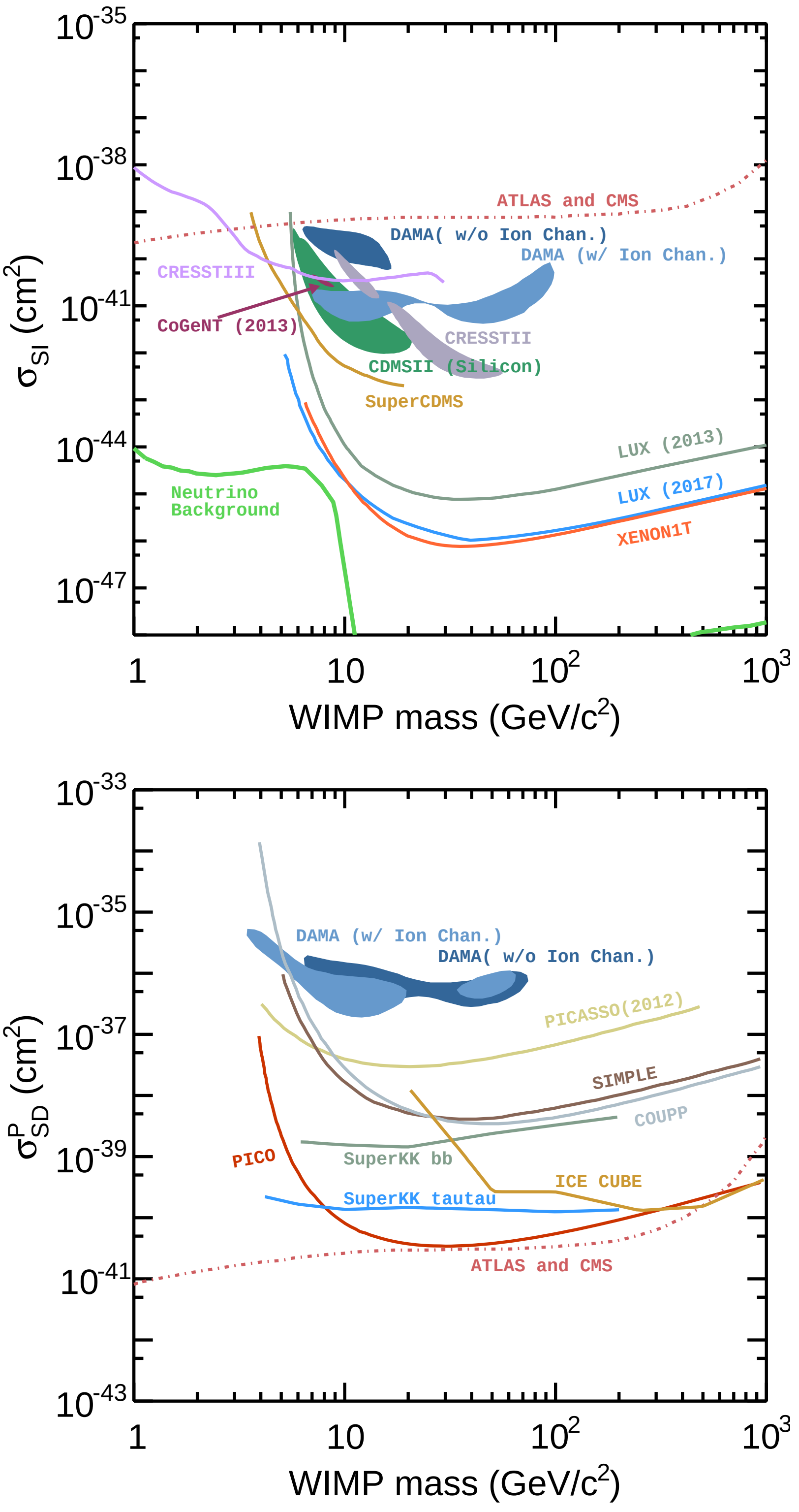

Figure 2.7.: WIMP-nucleon spin-independent (top) and spin-dependent (bottom) cross section limits. These limits are extracted by using a graph digitizer tool.

activity is an important effect. The searches for antimatter from the galactic halo is conducted by experiments on satellites. Photons freely propagate in the galaxy so that they can point back to their origin. They are also weakly attenuated over the large galactic distance scale, thus their energy spectra observed on the Earth would be close to the generated spectra from the WIMP annihilation. Neutrinos also freely propagate in the galaxy and also through dense matter. However, neutrinos are hard to detect since they interact only via the weak interactions. Hence, very large detectors are required. SuperKamiokande [27] and IceCube [28] provide the strong upper limits on the SD scattering cross section and their results are also shown in Figure 2.7. These limits are obtained considering WIMPs annihilation into $b\bar{b}$, $\tau^+\tau^-$, and W^+W^- pairs.

2.3.3. Collider searches

Since WIMPs can couple to SM particles, we could produce WIMPs in the interactions of SM particles. This may be achieved in the collisions of particles beams at particle colliders, where WIMPs may be produced directly or in subsequent decay chains. WIMPs are assumed to be neutral and stable, and they interact very weakly with the detector materials; hence they would leave the detectors without interacting. This would appear as missing energy in detected events. If we only produce WIMPs, the detectors do not observe any signatures of WIMPs. Hence, collider searches are based on the energy conservation and the detection of SM particles, which are produced in the particular interactions, to measure the missing energy. Because WIMPs are produced in pairs, the collider experiments can probe WIMP masses below half of the collision energy or decaying particle mass. Unlike direct detection experiments, collider searches can not provide direct evidence that a detected WIMP is the particle constituting the galactic DM, but they can provide a complementary probe for dark matter. These searches also can probe the light WIMP mass region where direct detection methods can not search due to their energy thresholds.

One way to search for WIMPs at colliders is to search for final states with missing energy and a photon or jet, and looking at excesses in the missing energy spectrum compared to the expected background contribution. The common approach to interpreting these results is to use effective operators to describe the interaction between SM particles and WIMPs. This approach does not require a complete model for the WIMP, but makes it possible to compare the results of collider searches with the

WIMP-nucleon cross sections from direct detection experiments. The production of WIMPs also requires a new mediator particle in extensions of the SM. The effective operators are valid when the energy of the process is small compared with the mass of the mediator.

The ATLAS [29, 30] and CMS [31, 32] experiments at the Large Hadron Collider (LHC) carried out searches that utilized the effective operator approach. They considered effective operators for interactions between fermionic or scalar WIMPs and quarks or gluons. Each operator is characterized by an effective suppression scale Λ and the WIMP mass m_χ. They didn't observe any significant WIMP signals and obtained results comparable to the constraints from direct detection experiments. Their results have been included in Figure 2.7.

Searches for WIMPs were also performed at electron-positron colliders. Electron colliders can use cascade decays or transitions of known particles, such as Υ mesons, to observe missing energy. The results are generally shown as branching fractions. Results from the Belle, BaBar, and BESSIII experiments have been interpreted as WIMP-nucleon cross sections in [33, 34]. That work developed a similar theoretical framework as the LHC experiments; but added quarkonium states and interactions of vector WIMPs with quarks.

Chapter 3

CP-odd Higgs boson and low mass dark matter

WIMP is a collective name describing neutral stable particles that have masses of the electroweak scale and interact weakly with ordinary matter. Extensions of the SM provide WIMP candidates, the most favored candidate is the *neutralino*. The neutralino is massive, stable, and can annihilate into the SM particles. When the neutralino interacts with SM particles, this occurs through the exchange of a new mediator, which is not present in the SM. Many candidates have been proposed for this new mediator, one of which can be a pseudoscalar boson known as CP-odd Higgs boson A^0. This chapter briefly describes the SM and supersymmetric extensions of the SM. We also introduce a possible approach to searching for low mass WIMPs and the A^0 Higgs boson at collider experiments.

3.1. Standard model

The SM is the currently accepted theory used to describe fundamental interactions and elementary particles that make up the universe. All the particle species of the SM have been detected experimentally; the last species was the Higgs boson, which was discovered by the CMS [35] and ATLAS [36] collaborations at the LHC in 2014.

In the SM, matter is made of elementary particles, called quarks and leptons, which are spin one-half fermions. Both quarks and leptons come in six types, known as "flavors", and are classified into three generations as shown in Figure 3.1. The quarks consist of the up (symbol: u) and down (d) quark, charm (c) and strange

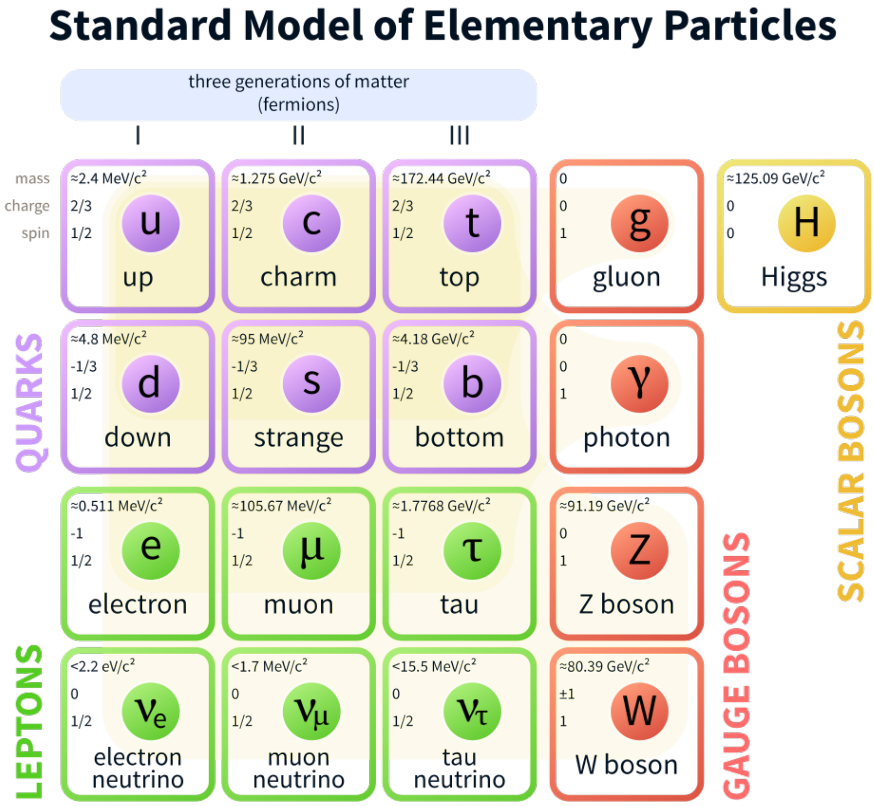

Figure 3.1.: The standard model of elementary particles. From:Wikipedia Credit:MissMJ

(s) quark, and bottom (b) and top (t) quark; the leptons consist of the electron (e) and electron neutrino (ν_e), muon (μ) and muon neutrino (ν_μ), and tau (τ) and tau neutrino (ν_τ). Two quarks and two leptons constitute each generation.

The interactions among these matter particles are governed by four fundamental forces: the strong force, the weak force, the electromagnetic force, and the gravitational force. The SM includes the first three forces but not the gravitational force. The three fundamental forces take place from the exchange of force carrier particles, also called mediators, which are spin one gauge bosons. The strong force is mediated by eight gluons g, that carry color charges, and the weak force is mediated by the $W^\pm$ and Z^0 bosons. The electromagnetic force is carried by the photon γ. The strong force only couples to quarks, which have color charges. The weak force can couple to all particles, and the electromagnetic force can couple to quarks and charged leptons. The Higgs is also a boson, but it has a spin of zero. The Higgs boson gives mass to massive elementary particles, but it does not mediate a force.

Every particle has a corresponding antiparticle, which has the same mass but opposite internal quantum numbers, such as the electric charge and color charge. Quarks form hadrons, which are found in two categories: baryons, consisting of three quarks, and mesons, consisting of a quark (q) and antiquark ($\bar{q}$). The ordinary matter referred in the previous chapter is baryonic matter mainly composed of first generation particles. Because baryons made of second or third generation particles have very short lifetimes, they can not sustain their state to remain in the universe.

Despite providing successful explanations for nearly all observations and experiments, there are still problems the SM can not solve. The SM does not contain any candidates for the dark matter, can not explain the matter-antimatter asymmetry in the universe, and is not able to account for a large discrepancy between aspects of the weak force and gravity. Besides these, there are various unexplained experimental results, such as the non-zero mass of neutrinos. These motivate extensions of the SM. Various new physics models have been suggested, the most prominent model is supersymmetry (SUSY).

3.2. Supersymmetry

Supersymmetry is a hypothetical symmetry of space and time that relates bosons and fermions. Supersymmetry requires every SM particle to have at least one associated supersymmetric particle, called superpartner, which differs in spin by half. Each SM fermion has a superpartner *sfermion*, which is a boson, and each SM boson has a superpartner *bosino*, which is a fermion. When the SM is extended to include supersymmetry, the resulting theory is known as the minimal sypersymmetric standard model (MSSM).

3.2.1. Minimal sypersymmetric standard model

As the name implies, the MSSM is the model which minimally extends the SM to incorporate supersymmetry. The MSSM requires an extra Higgs doublet, which leads to total five Higgs bosons, and superpartners for each of the SM particles. This model includes a conserved quantum number, called R-parity:

$$R = (-1)^{3(B-L)+2S} , \tag{3.1}$$

where B is the baryon number, L is the lepton number, and S is the spin of the particle. All of the SM particles have R-parity $R = 1$ and all supersymmetric particles have $R = -1$. Thus, as a consequence of R-party conservation, supersymmetric particles can only decay into an odd number of supersymmetric particles. This fact makes that the lightest supersymmetric particle (LSP) stable because there is no kinematically allowed decay process which preserves R-parity. R-parity conservation also implies that LSPs can only annihilate in pairs into SM particles.

The MSSM induces new particles called neutralinos, which are mixtures of the neutral superpartners of the Higgs bosons and the neutral superpartners of gauge bosons. The lightest supersymmetric particle can be the lightest neutralino which is the mixture of the supersymmetric partners of the photon, Z, and two neutral CP-even Higgs bosons. This neutralino naturally becomes a WIMP candidate.

The MSSM scenario introduces a term for the two Higgs doublets with the parameter μ, called the suppersymmetric Higgs mass parameter. This term is required to provide masses for the fermionic superpartners of the Higgs bosons. This μ parameter is naturally expected to be zero or of order of the Planck scale, but it has to be of the order of the electroweak scale due to phenomenological constraints. There is no theoretical explanation for why the μ parameter is much smaller than the Planck scale and non-zero. This is called the μ-problem which is a question about the naturalness problem [37].

3.2.2. Next-to-minimal sypersymmetric standard model

The next-to-minimal supersymmetric standard model (NMSSM) has been motivated to solve the μ-problem. The NMSSM requires an additional Higgs singlet, compared to the MSSM. Due to the added Higgs singlet, the NMSSM additionally provides two Higgs bosons and one neutralino, which can be the lightest neutralino. Therefore, this model contains a total of three CP-even, two CP-odd, and two charged Higgs bosons, and a total of five (neutral) neutralinos.

Another motivation for the NMSSM is related to the lightest CP-odd Higgs boson A^0. The MSSM predicts the CP-even Higgs boson mass m_h as less than $m_Z \simeq 91$ GeV with a tree-level calculation, however the LEP experiment excluded this. The LEP searched for the CP-even Higgs boson decaying to $b\bar{b}$ and set the lower bound $m_h \geq$ 114 GeV. The CP-odd Higgs boson in the NMSSM allows for new decay channel where the CP-even Higgs boson dominantly decays into A^0. Thus, if the mass of A^0 is below $2m_b$, then the CP-odd Higgs boson invalidates the LEP constraints on m_h [38, 39]. The ALEPH [40] and BaBar [41–44] experiments constrained this new scenario, however, some parameter space still remains [45].

Neutralinos in the NMSSM are stable for the same reason as in the MSSM. The neutralinos in the MSSM have preferred masses in the 100 GeV - 1 TeV range. However, the lightest neutralino, which includes the superpartner of the Higgs singlet, in the NMSSM can have a mass in the range of 100 MeV - 20 GeV [46]. This can open up decays of the CP-odd Higgs boson into pairs of neutralinos: $A^0 \to \chi\chi$. This neutralino can be a low mass WIMP candidate.

3.2.3. Low mass dark matter

Several direct detection experiments reported observations of excesses above background in the WIMP mass range of 6 - 30 GeV. These regions are excluded by other direct detection experiments. We can not explain these observations yet. They might be a hint of the existence of low mass WIMPs with masses of the order of a few GeV.

The lightest neutralino in the NMSSM can be a candidate for low mass WIMPs. This neutralino can be present in the range of masses claimed as signals in direct detection experiments, and could generate the dark matter abundance observed today. Besides of the neutralino, there is another plausible low mass dark matter candidate from the asymmetric dark matter (ADM) scenario [47, 48].

The ADM scenario is motivated by the observation that the baryon and dark matter energy densities close to $\Omega_c \simeq 5\,\Omega_b$. The standard thermal WIMP scenarios consider this as a coincidence because the baryons and dark matter are generated by different mechanism. In the ADM, the asymmetry between matter and anti-matter in the SM sector is transferred to the DM sector by a certain mechanism, rather than by thermal equilibrium. Thus asymmetries in the number densities of baryons and dark matter are comparable after the transfer, we have

$$n_\chi - n_{\bar{\chi}} \sim n_b - n_{\bar{b}} \, , \tag{3.2}$$

where n_χ and $n_{\bar{\chi}}$ are the DM and anti-DM number densities, and n_b and $n_{\bar{b}}$ are the baryon and anti-baryon number densities. Consequently the energy densities of baryons and dark matter are related by:

$$\frac{\Omega_b}{m_p} \simeq \frac{\Omega_c}{m_\chi}\,, \tag{3.3}$$

where m_p is the proton mass and m_χ is the dark matter mass. From the observed energy densities, this suggests the natural mass scale for asymmetric DM candidates to be $m_\chi \sim$ 5 GeV. In general, masses in the range of 5 - 15 GeV are predicted. This ADM scenario can be reconciled with the NMSSM [49].

3.3. Search for CP-odd Higgs boson and low mass dark matter

Since the A^0 can be light and couple to low mass WIMPs, we can search for A^0 and WIMPs at electron-positron colliders [50, 51]. Such searches can be performed with radiative decays of mesons, such as the Υ or ψ. This thesis only focuses on finding signals from the $\Upsilon(1S)$. Since the mass of the A^0 is unknown, we consider two processes: the on-shell process, $\Upsilon(1S) \to \gamma A^0, A^0 \to \chi\chi$; and the off-shell process,$\Upsilon(1S) \to \gamma\chi\chi$.

The radiative $\Upsilon(1S) \to \gamma A^0$ decay can have a larger branching fraction (BF), of the order of $10^{-5} - 10^{-4}$ [52], than the SM process $\Upsilon(1S) \to \gamma\nu\bar{\nu}$, which has a similar aspect to the signal. We calculate this expected neutrino contribution from the $\Upsilon(1S)$ by referring to [51], which describes the corresponding calculation for the Υ(3S), and obtain

$$\mathcal{B}(\Upsilon(1S) \to \gamma\nu\bar{\nu}) \approx 2.49 \times 10^{-9}\,. \tag{3.4}$$

The signal channels have previously been searched for by CLEO [53] and BaBar [54, 55], and the results are summarized in Table 3.1. The current best limits on the BFs are from BaBar measurements on the $\Upsilon(1S)$ in 2010 and Υ(3S) in 2009.

Collaboration	DATA	Channel	BF U.L. at 90% C.L.
CLEO	960k $\Upsilon(1S)$	$\mathcal{B}(\Upsilon(1S) \to \gamma A^0)$	(0.8-80) $\times 10^{-5}$ for $M_{A^0} < 8.4$ GeV/c^2
		$\mathcal{B}(\Upsilon(1S) \to \gamma\chi\chi)$	(0.3-60) $\times 10^{-4}$ for $M_\chi < 4.0$ GeV/c^2
BABAR	122M $\Upsilon(3S)$	$\mathcal{B}(\Upsilon(3S) \to \gamma A^0)$	(0.7-31) $\times 10^{-6}$ for $M_{A^0} < 7.8$ GeV/c^2
BABAR	98M $\Upsilon(2S)$	$\mathcal{B}(\Upsilon(1S) \to \gamma A^0)$	(1.9-37) $\times 10^{-6}$ for $M_{A^0} < 9.2$ GeV/c^2
		$\mathcal{B}(\Upsilon(1S) \to \gamma\chi\chi)$	(0.5-24) $\times 10^{-5}$ for $M_\chi < 4.5$ GeV/c^2

Table 3.1.: Summary of previous invisible decay searches with a single photon final state.

Chapter 4

The Belle experiment

The Belle experiment is located at the High Energy Accelerator Research Organization, known as KEK, in Tsukuba, Japan. It operated from 1999 to 2010. The Belle detector was originally designed to study CP violation and the Cabibbo-Kobayashi-Maskawa (CKM) mechanism by using B meson decays. The B mesons are produced in the decay of $\Upsilon(4S)$ mesons, which are created by the KEKB asymmetric energy electron-positron collider. The present analysis is based on data collected with the Belle detector at the KEKB accelerator. This chapter describes the KEKB accelerator, Belle detector, and the Belle trigger systems.

4.1. The KEKB accelerator

The KEKB accelerator is a electron-positron circular collider with asymmetric energies: a 3.5 GeV positron beam and an 8 GeV electron beam [56, 57]. The electron and positron beams consist of about 1000 bunches with a bunch spacing of 1.84 m and collide at the interaction point (IP) about every 8 ns. Electrons and positrons are first accelerated to their nominal energies in a linear accelerator (LINAC), then injected into the respective rings, the high energy ring (HER) for electrons and the low energy ring (LER) for positrons. The beam energies result in a center of mass (CM) energy corresponding to the mass of the $\Upsilon(4S)$ resonance:

$$\sqrt{s} = \sqrt{E_{LER} \cdot E_{HER}\ (1 + cos(\theta_{beam}))} \simeq 10.58 \text{ GeV} \,, \tag{4.1}$$

where E_{HER} is the electron beam energy, E_{LER} is the positron beam energy, and $\theta_{beam} = 22$ mrad is the beam crossing angle. The $\Upsilon(4S)$ resonance is a bound state

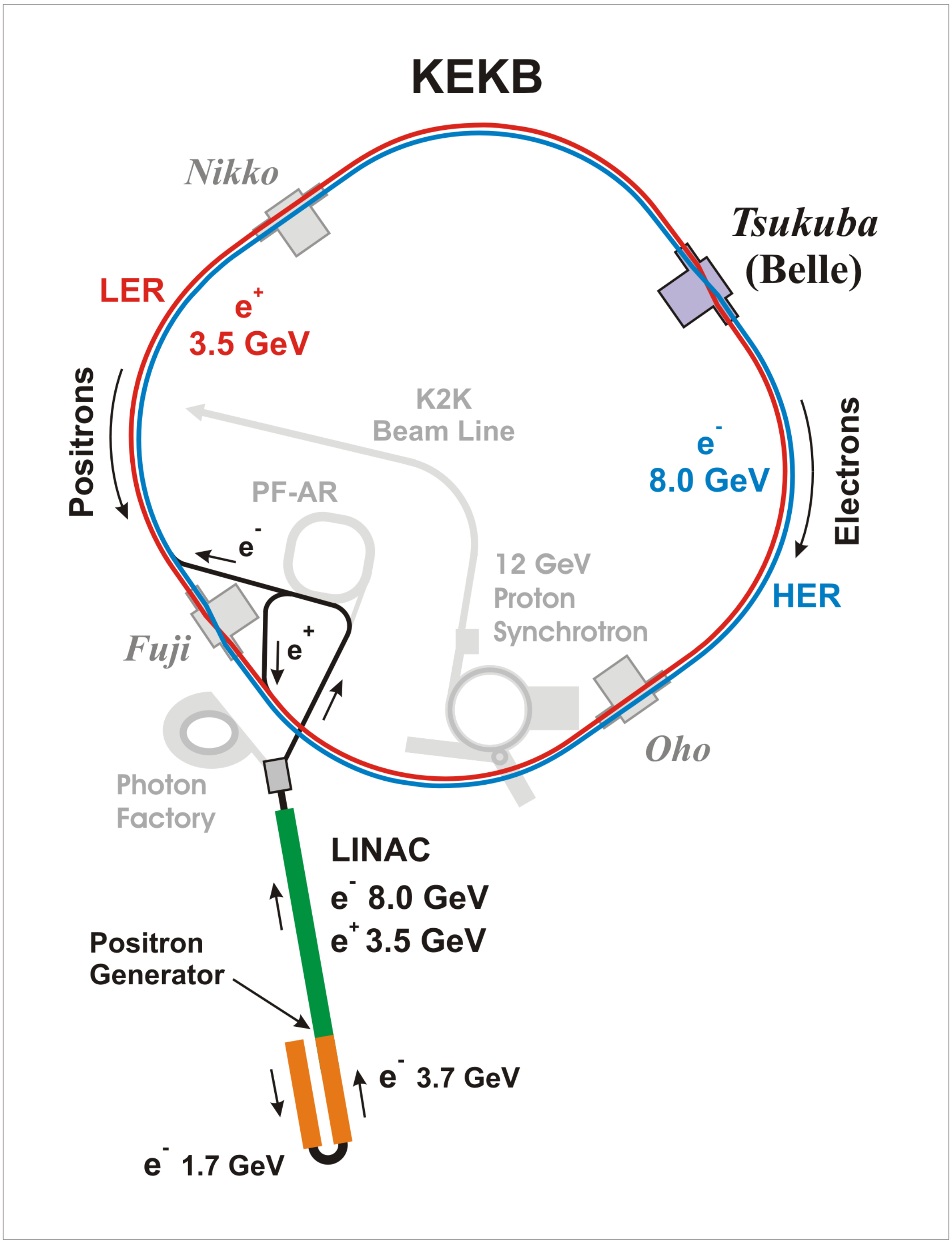

Figure 4.1.: The KEKB accelerator.

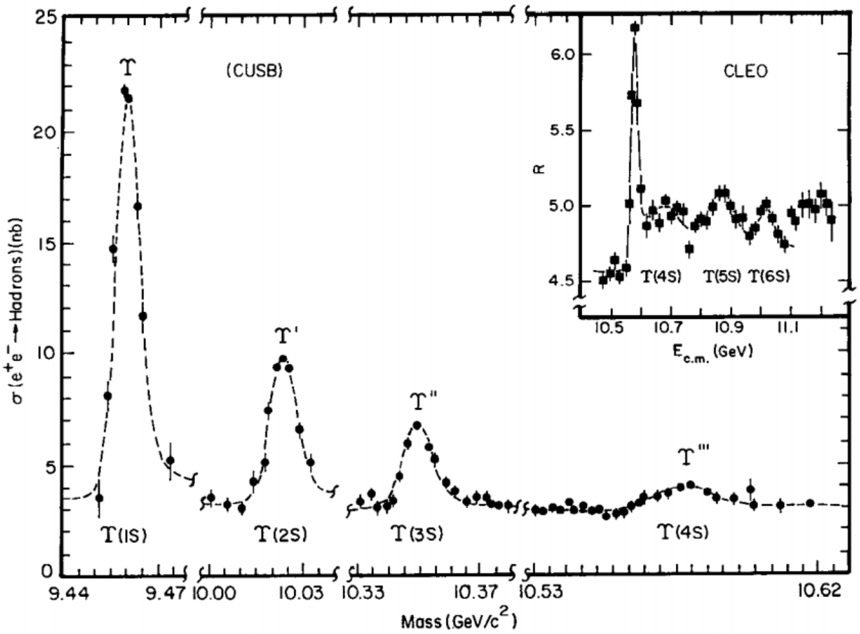

Figure 4.2.: Cross section for inclusive production of the Υ resonances. From [58].

of $b\bar{b}$ quarks that predominantly decays to a pair of B mesons. Belle also collected data at energies corresponding to the masses of the $\Upsilon(1S)$, $\Upsilon(2S)$, $\Upsilon(3S)$, and $\Upsilon(5S)$ resonances. While collecting data, other processes, such as Bhabha scatterings, two-photon processes, tau productions, and quark pair productions, also occur. The peak luminosity $\mathscr{L}$ of the accelerator is defined as

$$R = \mathscr{L}\, \sigma_{e^+e^-} \,, \tag{4.2}$$

where R is the rate of e^+e^- collisions and $\sigma_{e^+e^-}$ is the total cross section. KEKB achieved a peak luminosity of 2.11×10^{34} cm^{-2}s^{-1} in 2009. The Belle detector recorded a total integrated luminosity of about 10^{42} cm^{-2} = 1 ab^{-1}.

4.2. The Belle detector

The Belle detector [59] is a general purpose spectrometer to detect charged and neutral particles. The detector is configured with a 1.5 T superconducting solenoid coil and consists of several sub-detectors as shown in Figure 4.4. The sub-detectors of the Belle detector are the silicon vertex detector (SVD), the central drift chamber (CDC), the aerogel threshold Cherenkov counter (ACC), the time-of-flight scintilla-

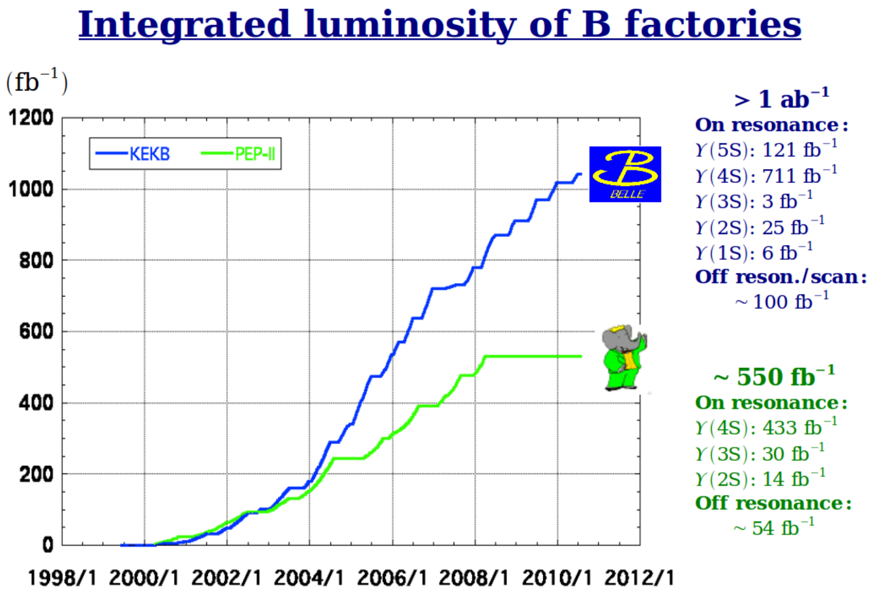

Figure 4.3.: Integrated luminosity of B factories.

tion counter (TOF), the electromagnetic calorimeter (ECL), and the K_L^0 and muon detector (KLM).

The Belle coordinate system in defined so that the z-axis is parallel to the HER beam direction, the horizontal x-axis is pointing toward the outside of the accelerator ring, and the y-axis is vertical. The origin of the coordinate system is defined as the position of the nominal IP, and the polar angle θ is the angle from the positive z-axis, the azimuthal angle ϕ is the angle in the xy-plane between the projected position vector and the positive x-axis, and r is the distance from the origin. The Belle detector covers the all azimuthal angles ϕ and polar angles θ from 17° to 150°, which corresponds to 92% of the full solid angle.

4.2.1. Silicon vertex detector (SVD)

The silicon vertex detector (SVD) is the innermost sub-detector and provides decay vertex information of detected particles with high precision. Measurement of z-vertex positions with a precision of $\simeq$ 100 μm is crucial to observe time-dependent CP asymmetries in decays of B mesons, which is the primary goal of the Belle experiment. Since most B decay products of interest have the momenta around

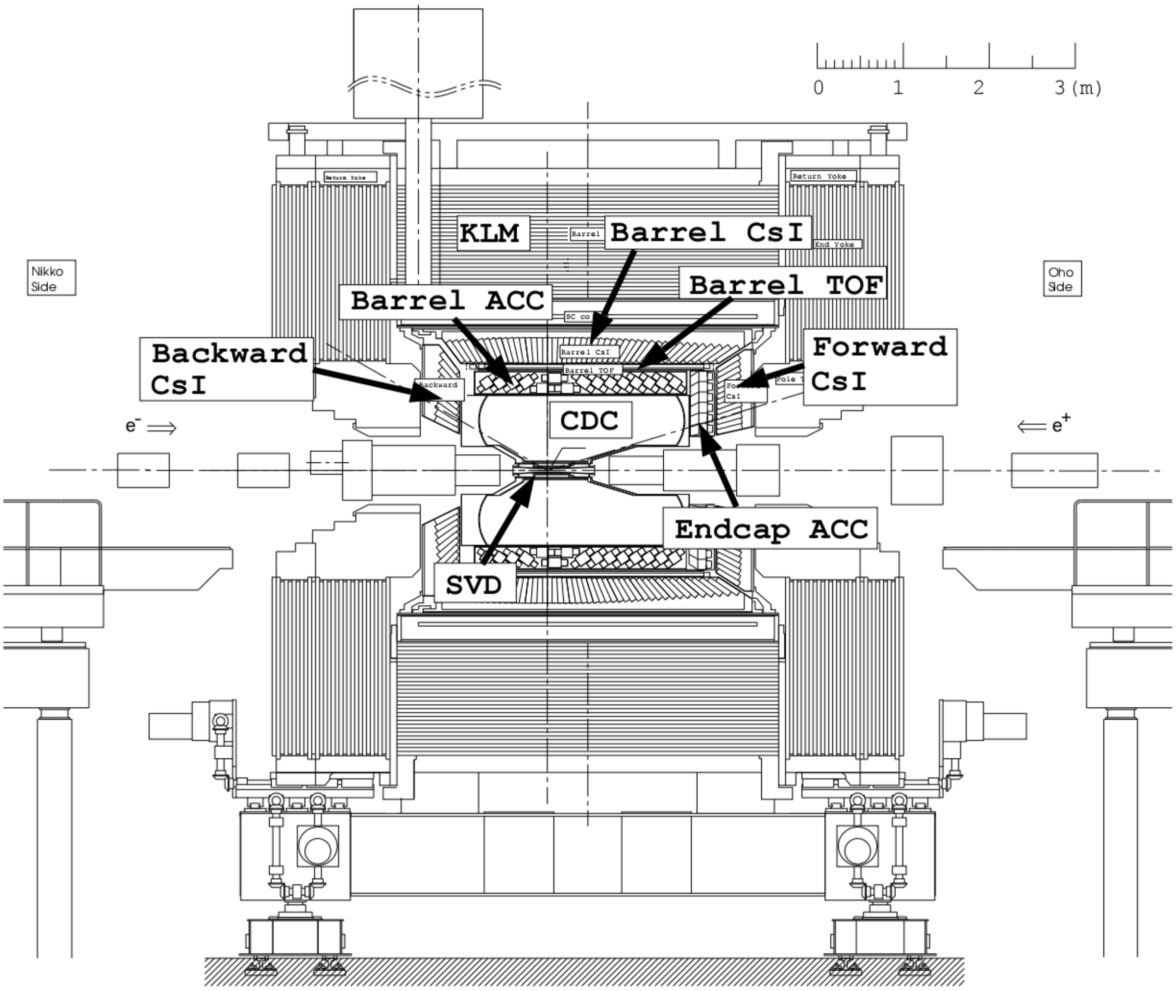

Figure 4.4.: The Belle detector. From [59].

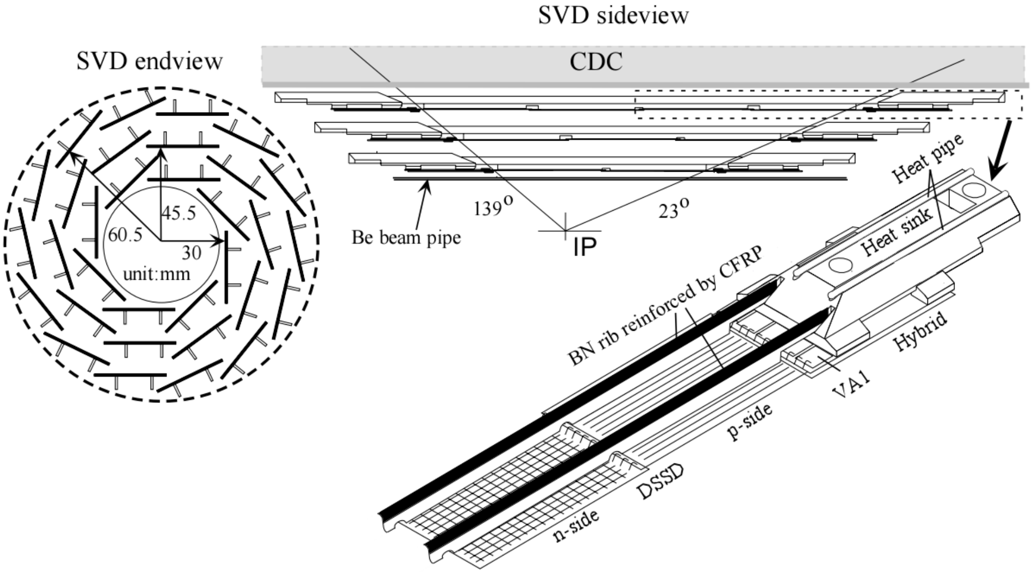

Figure 4.5.: Silicon vertex detector (SVD). From [59].

1 GeV/c or less, the vertex resolution is limited by multiple Coulomb scattering in a material before the innermost SVD layer. Therefore, to achieve high vertex resolution, the SVD has to be placed as close as possible to the beam pipe; and the SVD, its support structure, and the beam pipe have to be thin, low in Z, and rigid.

The SVD consists of double-sided silicon detectors (DSSDs), which originally developed for the DELPHI detector. Two configurations have been used during the experiment, SVD1 and SVD2. The SVD1 consisted of three layers of DSSDs, it was upgraded to the SVD2, which consists of four layers of DSSDs, in 2003. Figure 4.5 shows side and end views of SVD1. Differences between the SVD1 and SVD2 are summarized in Table 4.1. SVD1 and SVD2 cover 86% and 92% of the solid angle, respectively. The DSSD has sense strips on both sides, which are arranged perpendicular to each other. The strips on one side measure the z positions, while those on the other side measure the ϕ positions. The strip pitch for the inner three layers is 75 μm in the z direction and 50 μm in the ϕ direction, while the one for the fourth layer is 73 μm in the z direction and 65 μm in the ϕ direction.

The performance of the SVD1 and SVD2 are measured by the resolution of the distances of closest approach to the IP, called impact parameters. The momentum dependence of the impact parameter resolutions are shown in Figure 4.6 and are described by the formulas: $\sigma_{xy} = 19.2 \oplus 54.0\ /\ (p\beta sin^{3/2}\theta)$ and $\sigma_z = 42.2 \oplus 44.3\ /\ (p\beta sin^{5/2}\theta)$ for SVD1; and $\sigma_{xy} = 17.4 \oplus 34.3\ /\ (p\beta sin^{3/2}\theta)$ and $\sigma_z = 26.3 \oplus$

Parameter	SVD1	SVD2
Number of DSSD layers	3	4
Number of total DSSD ladders	$8 + 10 + 14 = 32$	$6 + 12 + 18 + 18 = 54$
Radius of beam pipe	2 cm	1.5 cm
Radius of layers	30, 45.5, 60.5 mm	20, 34.2, 70, 80 mm
Coverage	$20^\circ < \theta < 139^\circ$	$17^\circ < \theta < 150^\circ$

Table 4.1.: Comparison of SVD1 and SVD2.

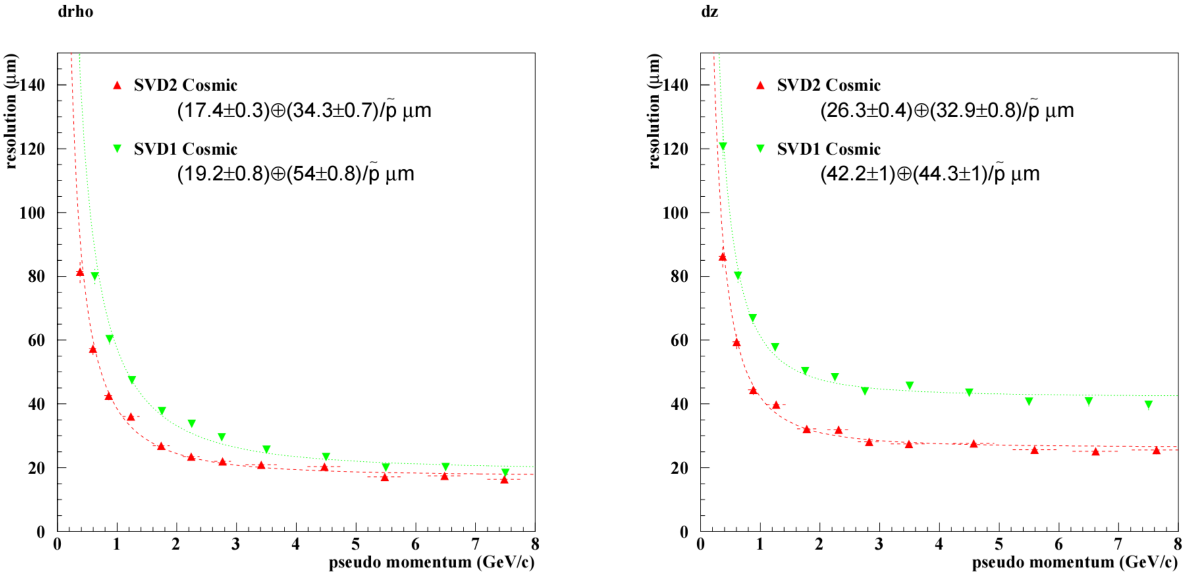

Figure 4.6.: Impact parameter resolution of SVD1 (reversed triangle) and SVD2 (triangle) in the r-ϕ plane (left) and the z direction (right). Pseudo momentum is defined in the text. From [59].

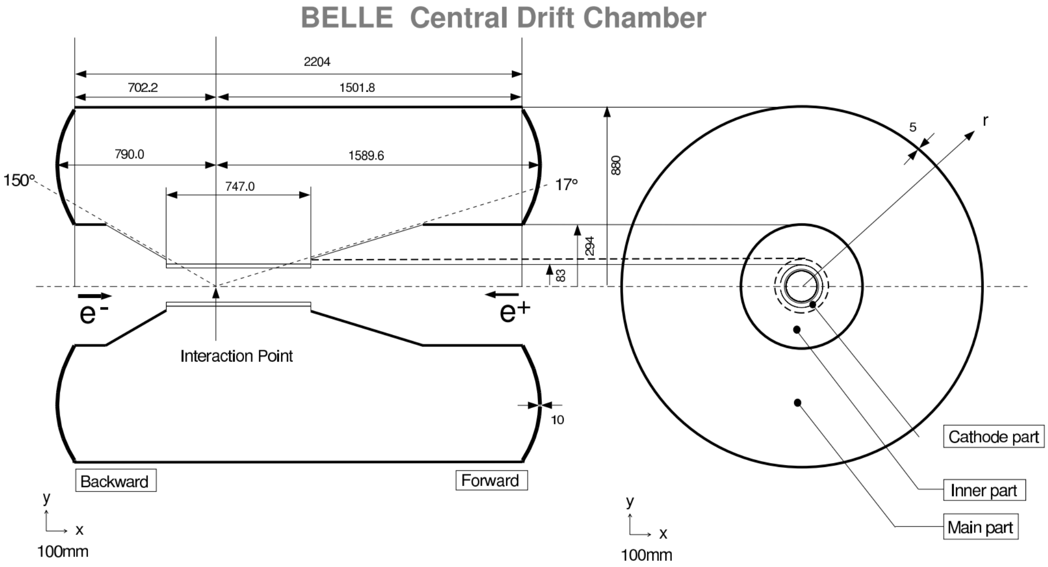

Figure 4.7.: Overview of the central drift chamber (CDC). From [59].

42.2 / $(p\beta sin^{5/2}\theta)$ for SVD2, where $\oplus$ denotes addition in quadrature. The pseudo-momentum is defined as $p\beta sin^{3/2}\theta$ for the r-ϕ plane and $p\beta sin^{5/2}\theta$ for the z direction, where p is the momentum of a particle, β denotes v/c, and θ is the polar angle between a momentum vector of a particle and the z-axis.

4.2.2. Central drift chamber (CDC)

The central drift chamber (CDC) measures three dimensional trajectories of charged particles and determines their momenta from the track curvature. The trajectory is fitted with five parameters, called helix parameters, which contain information on the curvature magnitude and impact parameters. The CDC also provides the energy deposit per unit length, dE/dx, of charged tracks to help with provide the particle identification.

The CDC is a cylindrical wire drift chamber which is filled with a 50% helium and 50% ethane gas mixture, which was selected to minimize multiple Coulomb scattering contributions to the momentum resolution, at a slightly above one atmosphere pressure. As shown on Figure 4.7, the CDC provides coverage in the polar angular region $17^\circ < \theta < 150^\circ$ and in the radii 83 mm $< r <$ 880 mm for SVD1 and 104 mm $< r <$ 880 mm for SVD2. The CDC geometry is asymmetric in the z direction, which is optimized for the boost from the asymmetric beam energies. The CDC contains 50 cylindrical layers, consisting of 32 axial-wire and 18 stereo-wire layers, and three cathode strip layers. The axial-wire layers are configured to be parallel to z-axis, while the stereo-wire layers are rotated ± 50 mrad to provide z coordinate information.

One CDC drift cell consists of one sense and eight electric field wires. The sense wires are gold-plated tungsten wires of 30 μm in diameter and the field wires are unplated aluminum of 126 μm in diameter. There are 8400 drift cells in the CDC. About 2.3 kV is applied on the sense wires, and the field wires are kept at the ground potential. Ionized electrons due to charged particle passing though the CDC drift towards the sense wires, and create an electron avalanche near the sense wires. Before the avalanche, ionized electrons have nearly constant drift velocity, about 4 cm/μs, therefore the pulse time can determine the distance of charged particle to the sense wire by comparing with the event trigger time. The measured pulse height provides energy deposit information, and dE/dx is measured by taking the mean of the ionization charge on the sense wires along the particle trajectory. Figure 4.8 shows a scatter plot of dE/dx versus momentum for various particle species, measured in collision data. The dE/dx resolution is obtained to be 7.8% in the pion momentum range of 0.4 - 0.6 GeV/c, and 6% for Bhabha and μ-pair events.

The transverse momentum resolution in combination with the SVD is measured to be:

$$\frac{\sigma_{P_t}}{P_t} = 0.19\, P_t \oplus \frac{0.30}{\beta}\,, \tag{4.3}$$

where P_t is the transverse momentum in GeV/c. The overall spatial resolution of tracking is measured to be 130 μm.

4.2.3. Aerogel Čherenkov counter (ACC)

The aerogel Čherenkov counter (ACC) provides information to separate charged pions and kaons, which are not well identified by the CDC dE/dx and the time-of-flight system for high momenta, in the range 1.2 GeV/c - 3.5 GeV/c.

The ACC consists of 960 counter modules in the barrel region and 228 modules in the forward end-cap region, as shown in Figure 4.9, covering the polar angular region of $34^\circ < \theta < 127^\circ$ and $17^\circ < \theta < 34^\circ$, respectively. Each module consists of

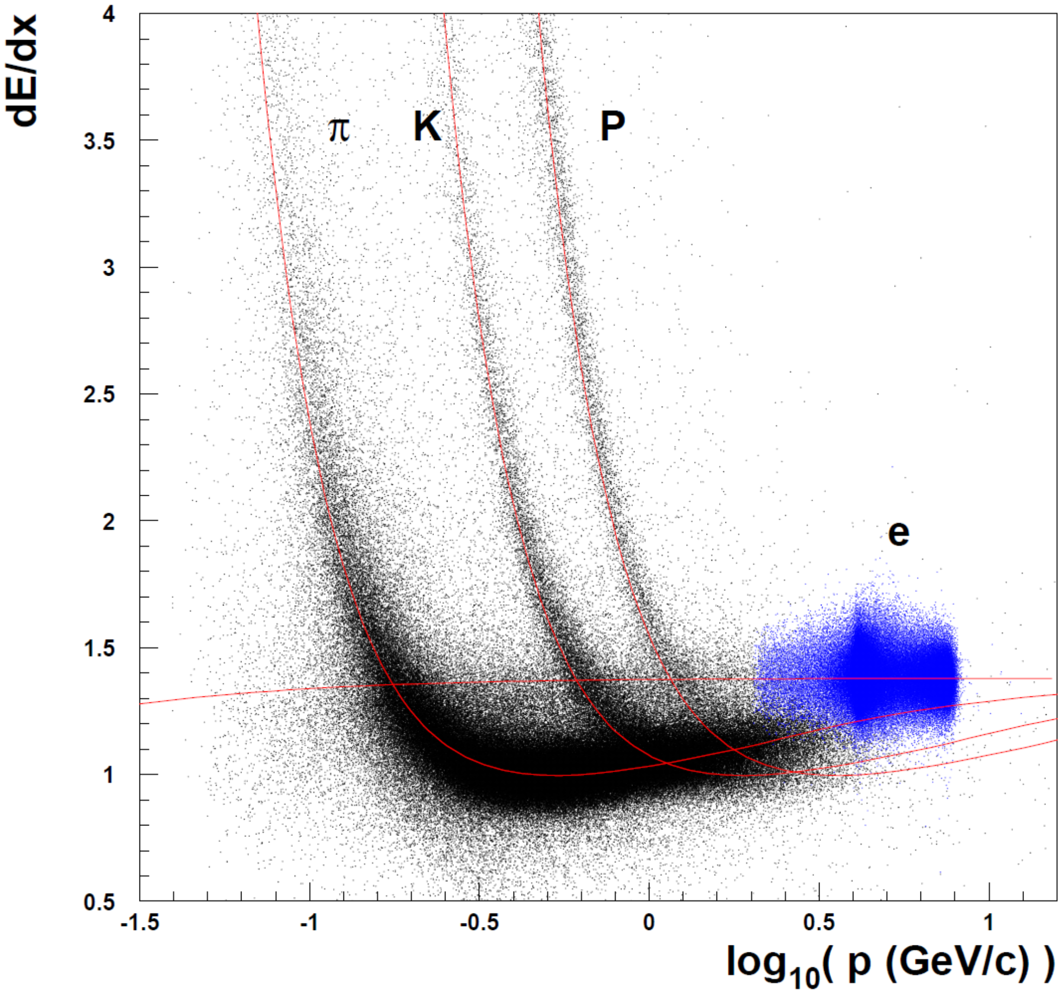

Figure 4.8.: Measured mean of dE/dx versus momentum for different particles. From [59].

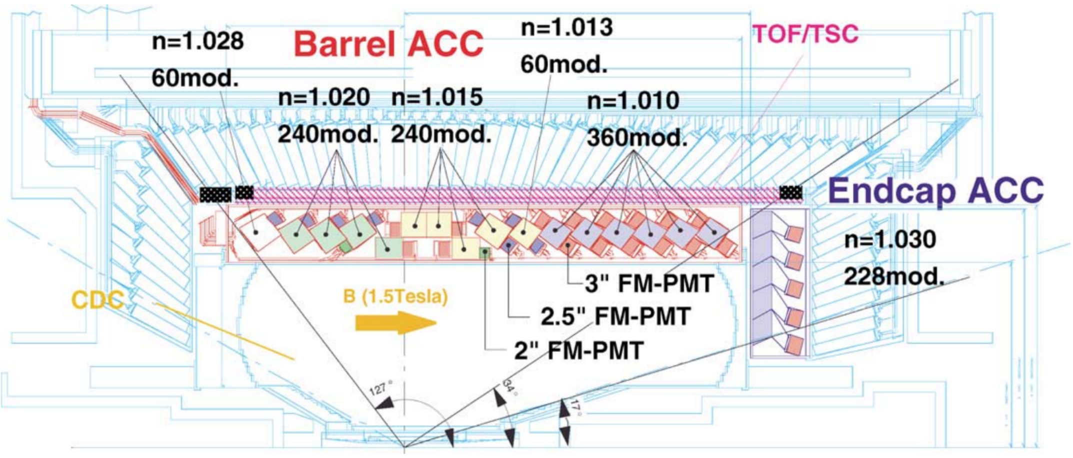

Figure 4.9.: Aerogel Čherenkov counter (ACC). From [59].

an aluminum box filled with five stacked silica aerogel tiles and one or two fine mesh-type photomultiplier tubes (FM-PMTs). In the barrel part, five different refractive indices of aerogels, between 1.01 and 1.02, are used depending on the polar angle. The end-cap region uses a single refractive index of 1.03.

A charged particle passing through a medium with refractive index n emits a cone of Čherenkov radiation, if the velocity of the particle, β, is larger than the speed of light in the medium, i.e. $n > 1/\beta$. At fixed momentum, the factor $1/\beta$ is proportional to the particle's mass, thus, in the momentum region of interest, pions produce Čherenkov radiation while kaons do not. Čherenkov photons are collected by the FM-PMTs, and typically 10 to 20 photons are detected in the barrel region and 25 to 30 in the end-cap region.

4.2.4. Time-of-flight counter (TOF)

The time-of-flight counter (TOF) provides pion/kaon separation in the momentum region below 1.2 GeV/c. The TOF counter also delivers fast timing signals for the trigger system to generate gate signals for analog-to-digital converters (ADC) and stop signals for time-to-digital converters (TDC).

The TOF system consists of 64 modules, each containing two trapezoidal-shaped TOF counters and one thin trigger scintillation counter (TSC), separated by a 1.5 cm radial gap. Each counter is made of plastic scintillator and is read out using FM-PMTs, which are mounted on both ends of the TOF counters and one end of

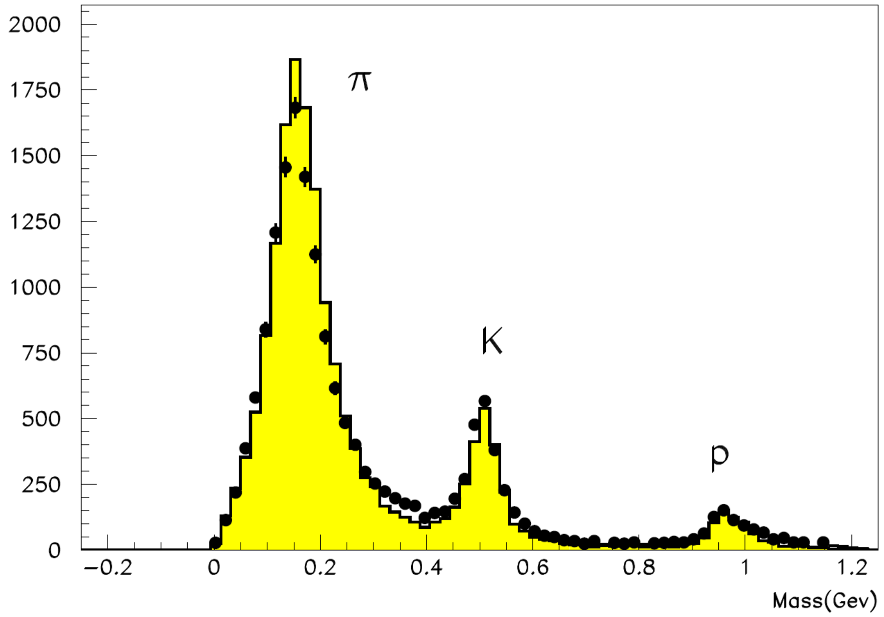

Figure 4.10.: Calculated masses of π, p, and K from TOF measurement for particle momenta below 1.2 GeV/c. From [59].

the TSC counter. The TSC is used to keep the fast trigger rate below 70 kHz, to avoid pileup in the trigger queue in any beam background conditions. The gaps between the TOF and TSC counters lead to reduced backgrounds in the TSC when the signals from the two counters are required for in coincidence. The modules are located at a radius of 1.2 m from the IP and cover the polar angular range of $34^\circ < \theta < 120^\circ$.

The time-of-flight of a particle is given by:

$$T = \frac{L}{c\,\beta} = \frac{L}{c}\sqrt{1 + \frac{m^2}{p^2}}\ , \tag{4.4}$$

where L is the flight length of particle from the IP to the TOF module, m is the particle mass, and p is the particle momentum measured by the CDC. Thus the measured T can determine the particle mass and hence the species. The TOF system has about 100 ps time resolution and achieves a 2σ separation for particle momenta up to 1.25 GeV/c as shown in Figure 4.10.

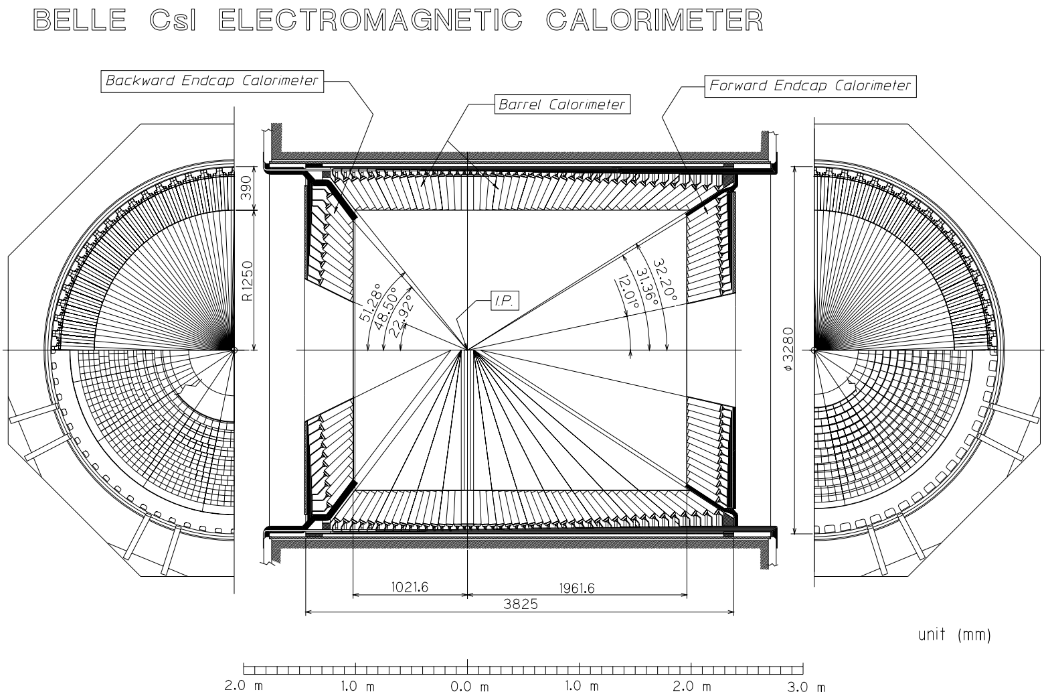

Figure 4.11.: Geometry of the electromagnetic calorimeter (ECL). From [59].

4.2.5. Electromagnetic calorimeter (ECL)

The Electromagnetic calorimeter (ECL) measures the energy and position of photons and electrons, and provides information to identify electrons.

High energy electrons lose energy by bremsstrahlung radiation, and the bremsstrahlung photons can produce electron-position pairs. The electrons and positrons produced can again generate bremsstrahlung photons, and these processes repeat until the energy of photons, electrons, or positrons is low. This is called an electromagnetic shower. The ECL measures the energy of electromagnetic showers.

The ECL consists of 8736 CsI(Tl) crystals. Each crystal is read out using two silicon PIN photodiodes with preamplifiers, attached at the end of the crystal. The ECL is composed of three sections: forward end-cap, barrel, and backward end-cap as shown in Figure 4.11. These three sections cover the polar angle regions $12.4^\circ < \theta < 31.4^\circ$, $32.2^\circ < \theta < 129.8^\circ$, and $130.7^\circ < \theta < 155.1^\circ$, respectively. Each crystal is 30 cm long with slightly different shape depending on its location and is oriented toward the IP. The 30 cm length corresponds to 16.2 radiation lengths, X_0, for electrons and 0.8 interaction lengths for K_L^0 mesons.

Electron identification primarily relies on a comparison of track momentum from the CDC and the energy deposit in the ECL. A shower in the ECL that is isolated from any tracks is identified as a neutral shower. The position resolution in mm is

$$\sigma_{pos} = 0.27 \oplus \frac{3.4}{\sqrt{E}} \oplus \frac{1.8}{\sqrt[4]{E}} , \tag{4.5}$$

and the energy resolution is

$$\frac{\sigma_E}{E} = \left(1.34 \oplus \frac{0.066}{E} \oplus \frac{0.81}{\sqrt[4]{E}}\right)\% , \tag{4.6}$$

where E is in GeV. The efficiency of electron identification is greater than 90% and the hadron fake rate (the probability of misidentifying a hadron as an electron) is $\sim$ 0.3% for a track with $p > 1$ GeV/c.

4.2.6. K_L and muon detector (KLM)

The K_L and muon detector (KLM) has been designed to identify K_L's and muons, and is the outermost of the Belle sub-detectors. The KLM consists of 15 detector layers and 14 iron layers in the barrel region and 14 detector layers in each of the forward and backward end-cap region. The detector layers detect charged particles using glass-electrode resistive plate counters (RPCs), and the iron plates are 4.7 cm thick, corresponding to 3.9 interaction lengths for K_L's. Each RPC superlayer contains two RPC layers, as shown in Figure 4.12, and each RPC layer consists of two parallel plate electrodes with a gas-filled gap, which has high resistance.

Charged particles passing the gap initiate a streamer in the gas. This results in a local discharge on the glass plates, which induces a signal on external pickup strips used to record the location and time of ionization. Particles detected that within 15 degree of an extrapolated track from the CDC also identified as muons, while those further from tracks are identified as K_L^0s. Muons are also discriminated from hadronic interactions based on their penetration depth and shower range. The efficiency of muon identification for momenta between 1 GeV/c and 3 GeV/c is 89%, with kaon and pion fake rates less than 2%.

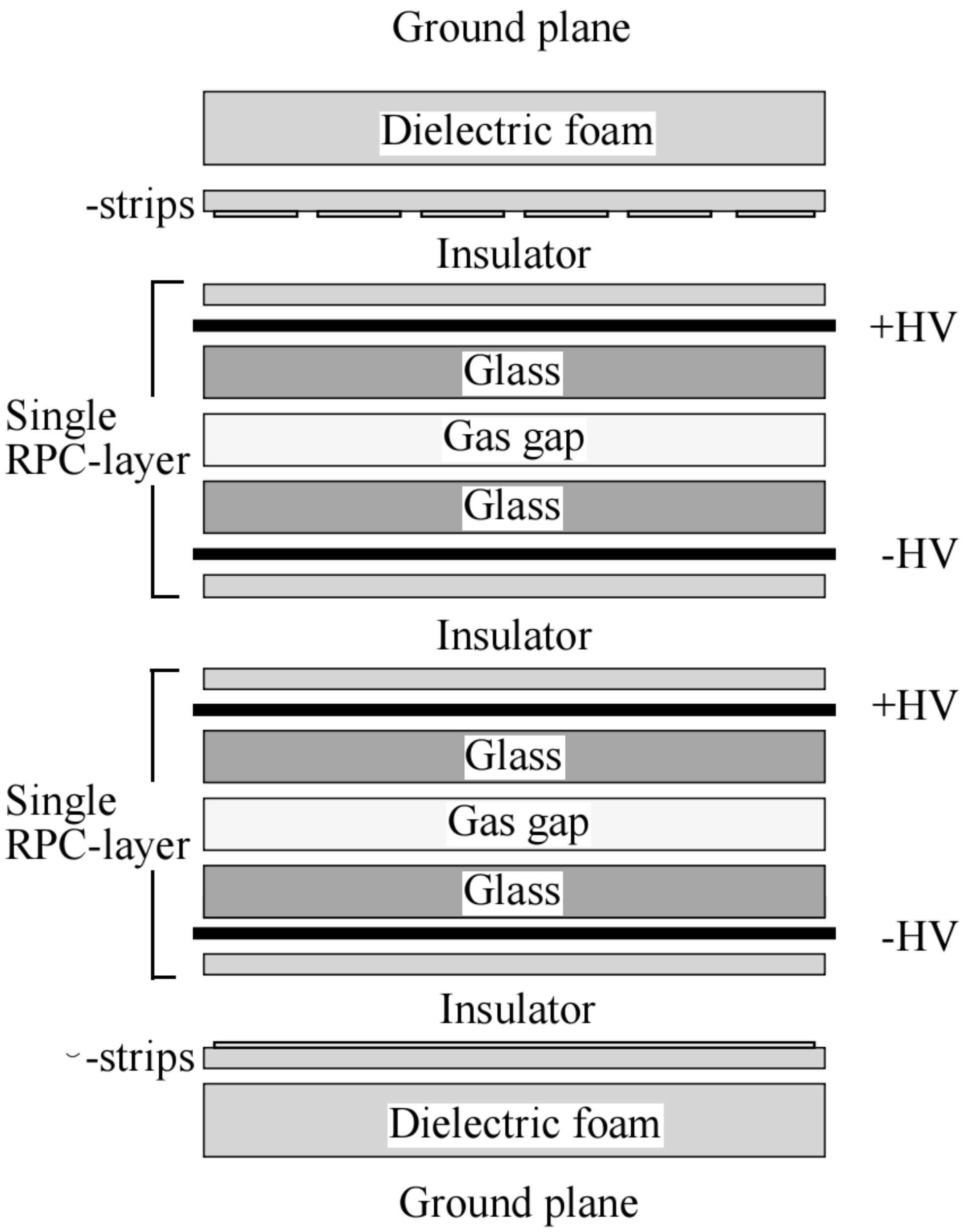

Figure 4.12.: Cross section of a RPC superlayer in the KLM detector. From [59].

Physics process	Cross sectio (nb)	Rate (Hz)
$\Upsilon(4S) \to B\bar{B}$	1.15	11.5
Hadron production from continuum	2.8	28
$e^+e^- \to \mu^+\mu^-$	0.8	8
$e^+e^- \to \tau^+\tau^-$	0.8	8
Bhabha ($\theta_{lab} > 17°$)	44	$4.4^{(a)}$
$e^+e^- \to \gamma\bar{\gamma}$ ($\theta_{lab} > 17°$)	2.4	$0.24^{(a)}$
2γ process ($\theta_{lab} > 17°, p_t > 0.1$ GeV/c)	$\sim$ 15	$\sim 35^{(b)}$
Total	$\sim$ 67	$\sim$ 96

Table 4.2.: Total cross section and typical Belle trigger rates at $\mathscr{L} = 10^{34}$ cm^{-2} s^{-1}. $^{(a)}$ indicates processes pre-scaled by 1/100. $^{(b)}$ indicates the restricted condition $p_t > 0.3$ GeV/c.

4.3. Trigger system

A trigger system is required to select the events of interest and to suppress background contributions to a data acquisition (DAQ) system. The DAQ system only transfers events which pass trigger conditions to the data storage system. Table 4.2 shows cross sections for various physics processes, and their typical trigger rates at a luminosity of 10^{34} cm^{-2} s^{-1}. The total event rate is expected to be around 100 Hz. Since KEKB operates at high beam currents, beam backgrounds are high. Beam background rates are sensitive to beam conditions, thus the trigger system should be robust against unexpected high beam background rates within the limit of the DAQ system, while the efficiency for physics events of interest is kept high.

The Belle trigger system [60] consists of three stages: a Level-1 hardware trigger, a Level-3 software trigger, and a Level-4 offline trigger. The Level-1 trigger consists of sub-detector triggers and a central trigger system, called Global Decision Logic (GDL). The Level-3 trigger is implemented in an online computing farm as a part of DAQ system. The Level-4 trigger rejects beam backgrounds using a fast tracking algorithm. An overview of the trigger system is shown in Figure 4.13.

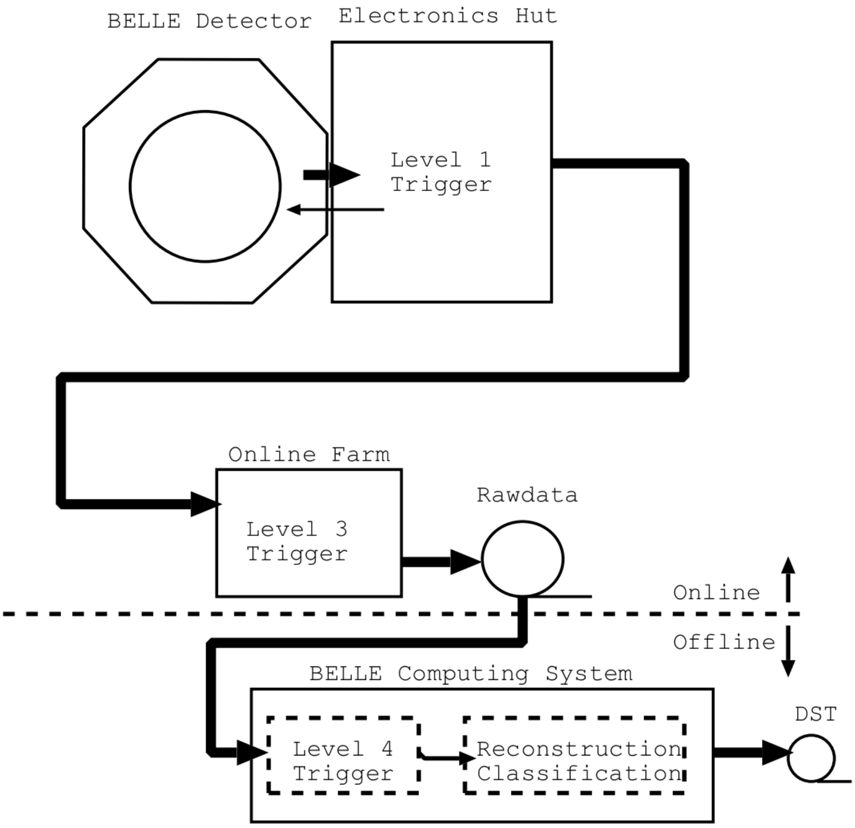

Figure 4.13.: Overview of the trigger system

4.3.1. Level 1 (L1) trigger

The Level-1 (L1) trigger collects trigger signals from sub-detectors and feeds them to the GDL as shown in Figure 4.14. The sub-detector triggers reaching at the GDL within 1.85 μs are used to make global trigger decisions, and the GDL provides the final L1 trigger signal at the fixed time of 2.2 μs after the event occurrence. The TOF and ECL triggers are used to determine the timing of the event occurrence. The SVD triggers are not implemented in the data samples used in this thesis.

The CDC and TOF provide trigger signals for charged particles. The CDC triggers are determined based on signals from axial superlayers, which provide the number of short and full tracks, determination of the maximum opening angle between tracks, and recognition of back-to-back tracks. The TOF gives an event timing signal and information on the hit multiplicity and topology to the GDL. The timing signal provides a gate signal for the ECL readout and T_0 to the CDC readout. The information on hit multiplicity and pattern is used to reduce the background

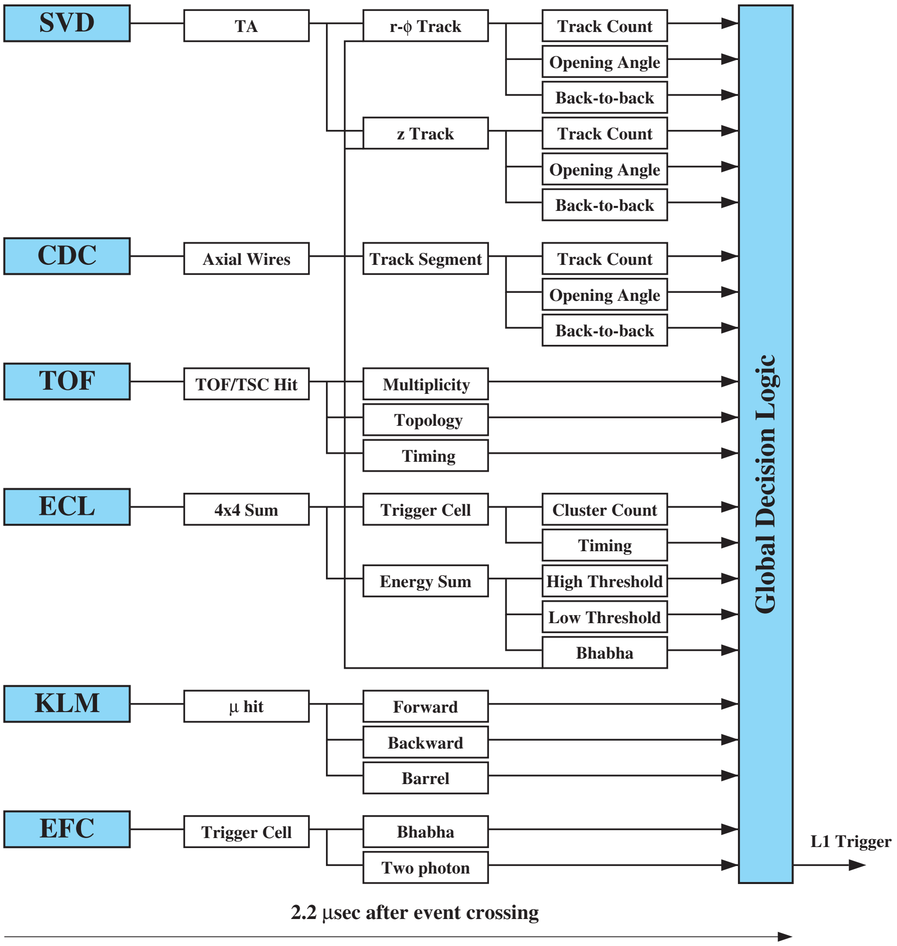

Figure 4.14.: Schematic of the Level-1 trigger system. The SVD triggers were disabled in April 2006.

trigger rate before timing signals are sent out to the GDL and to select an event in the GDL. The ECL provides trigger signals for both neutral and charged particles based on total energy deposit and cluster counting. The ECL trigger signals are used to determine the timing in the case that the TOF cannot generate the timing signal. The total energy triggers are sensitive to events with high electromagnetic energy deposition, while the cluster counting trigger is sensitive to multi-hadronic events that have low energy clusters and minimum ionizing particles. The ECL is divided into 17 sections in the θ direction: 12 sections in the barrel region, 3 in the forward and 2 in the backward end-cap regions. Bhabha events are triggered using back-to-back conditions, which are 11 combinations of the sections. The Bhabha triggers are not only used to veto the total energy triggers but also used to store Bhabha events. In the latter case, these triggers are prescaled to keep the rate less than 10 Hz. The total energy deposit triggers implement the thresholds of about

1 GeV and 3 GeV. The KLM trigger signals are used to save events which contain muon tracks.

The typical L1 trigger rate created by the GDL is about 200 Hz, the trigger rate is dominated by beam backgrounds. Trigger conditions are adjusted depending on beam conditions, keeping the average trigger rate around 200 Hz. Bhabha and two-photon events are prescaled by a factor of 1/100 due to their large cross sections. The trigger efficiency is monitored from the data using redundant triggers. The total efficiency is higher than 99.5% for hadronic B meson decays.

Although the L1 trigger efficiency is high for B meson decays, low multiplicity events, which we are interested in this thesis, suffer from the noticeable decrease in efficiency, due to the Bhabha veto and the energy thresholds in the total energy triggers.

4.3.2. Level 3 (L3) trigger

The Level-3 (L3) trigger is a software trigger which stores raw data containing all sub-detector information. The L3 trigger first checks the L1 trigger information and passes some categories of events, such as Bhabha events and random trigger events. If an event does not belong to these categories, the L3 trigger performs a fast reconstruction and rejects events having no tracks with impact parameter $|dz| <$ 5.0 cm and events with total energy deposit in the ECL less than 3 GeV. A large fraction of beam background events are discarded by this procedure, which results in a 50% reduction of stored events while retaining an efficiency of more than 99% for hadronic events.

4.3.3. Level 4 (L4) trigger

The Level-4 (L4) trigger is applied offline to filter events from the raw data. The difference between the L3 and L4 triggers is that raw data rejected by the L4 still remains on tape and can be read again whereas events rejected by the L3 are not recorded anywhere. The L4 trigger system has the role of rejecting backgrounds just before full event reconstruction. The L4 trigger has four stages, which operate in the following order: 1. selecting Bhabha and calibration events by checking the L1 and L3 trigger bits; 2. requiring the total energy deposited in the ECL from

Fzisan, which is a fast track/cluster finder, greater than 4 GeV; 3. requiring at least one good charged track reconstructed by Fzisan with $dr < 1.0$ cm, $|dz| < 4.0$ cm, and $p_t > 300$ MeV; 4. salvaging some events for monitoring. Approximately 78% of triggered events are rejected, while the efficiency for hadronic events is close to unity. The events selected by the L4 trigger are fully reconstructed and stored in data summary tapes (DSTs).

Chapter 5

Data analysis

The goal of this analysis is to search for a CP-odd light Higgs boson, A^0, and a low mass dark matter particle, χ, and set a limit on the branching fraction (BF) product $\mathcal{B}(\Upsilon(1S) \to \gamma A^0) \times \mathcal{B}(A^0 \to \chi\chi)$ and the branching fraction $\mathcal{B}(\Upsilon(1S) \to \gamma\chi\chi)$. This analysis using $\Upsilon(1S)$ decays from the dipion transition $\Upsilon(2S) \to \pi^+\pi^-\Upsilon(1S)$. We search for a single energetic photon with missing energy. The pions from the dipion transition have low transverse momentum, less than 550 GeV/c, due to a small mass difference between $\Upsilon(2S)$ and $\Upsilon(1S)$. Dark matter χ would escape the detector without interacting, thus we tag these two pions and a single photon to characterize a signal.

The on-shell process, $\Upsilon(1S) \to \gamma A^0, A^0 \to \chi\chi$, is characterized by a mono-energetic photon in the $\Upsilon(1S)$ frame with energy given by:

$$E^*_\gamma = \frac{M^2_{\Upsilon(1S)} - M^2_{A^0}}{2M_{\Upsilon(1S)}} \quad , \tag{5.1}$$

where $M_{\Upsilon(1S)} = 9.460$ GeV/c^2 is the $\Upsilon(1S)$ mass and M_{A^0} is the A^0 mass. On the other hand, the off-shell process, $\Upsilon(1S) \to \gamma\chi\chi$, has a broad photon energy spectrum due to the multi-body decay of the $\Upsilon(1S)$.

The two pions are used to obtain the invariant recoil mass of the dipion system and to ensure low backgrounds. The recoil mass is a quantity expected to peak at the $\Upsilon(1S)$ mass and is defined as:

$$M^2_{recoil} = s + M^2_{\pi\pi} - 2\sqrt{s}E^*_{\pi\pi} \quad , \tag{5.2}$$

where $\sqrt{s} = 10.02$ GeV is the $\Upsilon(2S)$ resonance energy, $M_{\pi\pi}$ is the invariant mass of the dipion system, and $E^*_{\pi\pi}$ is the energy of the dipion system in the CM frame of the $\Upsilon(2S)$. Using these two kinematic variables, E^*_γ and M_{recoil}, we perform a search for an A^0 and χ signal. We examine the photon energy spectrum and extract the yield of signal events as a function of M_{A^0} and M_χ in the interval $0 < M_{A^0} < 9.0$ GeV/c^2 and $0 < M_\chi < 4.5$ GeV/c^2. In this chapter, we present data samples, trigger requirement, event selections, background studies, probability density function (PDF) constructions, limit calculations, and systematic uncertainties.

5.1. Data samples

5.1.1. $\Upsilon(2S)$ experimental data

This analysis uses an un-skimmed data sample with an integrated luminosity of 24.9 fb^{-1}, corresponding to 157.3 ± 3.6 million $\Upsilon(2S)$ events in Belle experiment 67 and 71. The signal region in this analysis was not looked at, i.e. kept "blinded", until the event selection, background study, and yield extraction method were completed.

5.1.2. Monte Carlo simulation of signal events

It is important to prepare proper Monte Carlo (MC) samples to test and develop the analysis procedure. They are used to estimate the signal efficiency and background contributions and to construct probability density functions. The MC simulation is performed in two steps: generating decay processes and simulating detector responses.

In the Belle experiment, several physics event generators based on the MC techniques are embedded in the software library, called the "Belle library". In this analysis, the EvtGen MC event generator [61] is used to generate the signal processes, referred to as signal MC samples. The dipion transision

$$\Upsilon(2S) \to \Upsilon(1S)\pi^+\pi^- \qquad (5.3)$$

is simulated using the VVPIPI model. The PHSP model is used for the S-wave coupling of the processes:

$$\Upsilon(1S) \to \gamma A^0, A^0 \to \chi\chi \text{ and } \Upsilon(1S) \to \gamma\chi\chi \ . \tag{5.4}$$

The A^0 is assumed to have zero spin and zero decay width, while the χ is assumed to have half-integer spin. The VVPIPI model was originally developed for the $\psi' \to J/\psi\pi^+\pi^-$ decay to describe the decays of vector particles (V) to the other vector particles (V') and two pions. The PHSP model is generic phase space decay model which takes the average of the particle spins in the initial state and the final state. The on-shell and off-shell signal processes are generated with masses in the range of $0 < M_{A^0} \leq 9.2$ GeV/c^2 and $0 < M_\chi \leq 4.5$ GeV/c^2. Each mass is generated with 0.5 GeV/c^2 intervals of A^0 and χ mass. A total of 20 M_{A^0} and 10 M_χ samples are simulated and each sample contains 10^6 events.

The Belle detector responses to the final state particles is simulated using the GEANT3 software package [62]. The interaction of particles with detector materials, such as energy deposits, cascade production of daughter particles, and decays in flight are calculated every step of the evolution of the particle. Simulated results are recorded in the same format as the real experimental data using the same data process chain. Beam backgrounds, which are collected from the real experimental data with random triggers, are overlaid on the simulated MC events. The L1 trigger simulation, TSIM, and L4 software trigger are employed to simulate the effect of the triggers. Figure 5.1 shows examples of the generated photon energy spectrum, before including detector effects, for the on-shell and off-shell process for each lowest and highest mass MC sample.

5.1.3. Monte Carlo simulation of $\Upsilon(2S)$ decays

Standard model $\Upsilon(2S)$ decays can be backgrounds in this analysis. The $\Upsilon(2S)$ inclusive MC samples provided by the Belle collaboration do not contain information for TSIM nor recently measured decay channels. Thus we re-simulate $\Upsilon(2S)$ inclusive decays with EvtGen, using branching fractions listed in the PDG 2014. Details of the simulated decays are shown in Appendix A. We produce two data sets of 200×10^6 $\Upsilon(2S)$ events; each set corresponds to about 25% larger integrated luminosity than Exp. 67 and 71 combined.

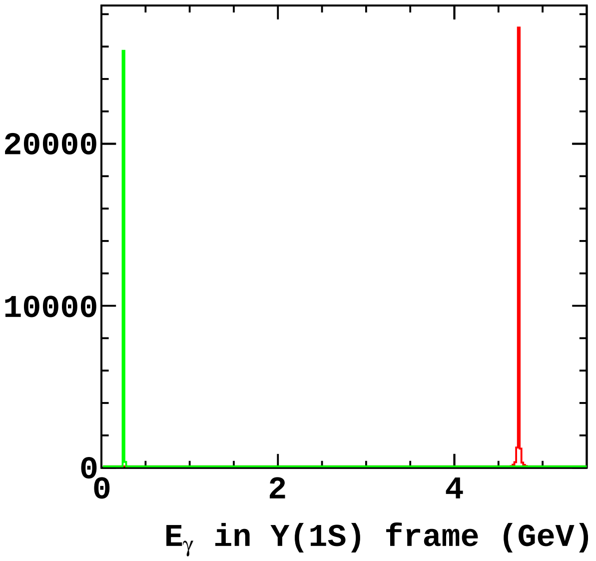

(a)

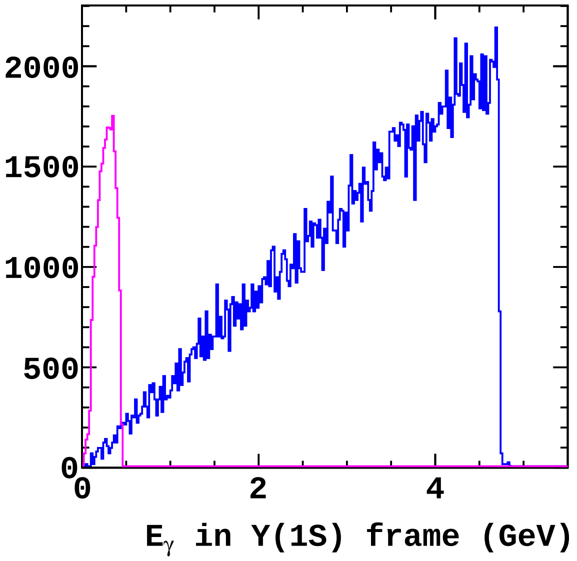

(b)

Figure 5.1.: Generated photon energy spectra in the Υ(1S) frame. (a): on-shell process M_{A^0} = 0.1 GeV/c^2 (red) and 9.2 GeV/c^2 (green). (b): off-shell process M_χ = 0.1 GeV/c^2 (blue) and 4.5 GeV/c^2 (magenta).

bit	name	definition
16	hie	e_high[a] & !csi_bb & !csi_comsic & !veto35
21	e_had	e_lum[b] & !csi_bb & !veto35
27	loe_fs_o	e_low[c] & ncdr_short>1 & ncdr_full>0 & cdc_open & !csi_bb & !veto35

[a, b, c] ECL total energy deposit > 1.0, 3.0, 0.5 GeV, respectively

Table 5.1.: The dominant L1 triggers in this analysis

5.1.4. $\Upsilon(4S)$ off-resonance data

We uses 40.41 fb^{-1} of $\Upsilon(4S)$ off-resonance experimental data to study continuum backgrounds. To determine the expected contributions of continuum background in $\Upsilon(2S)$ on-resonance data, we use the formula:

$$N_{cont} = f_{scale} N_{off} = \frac{\mathscr{L}_{on}}{\mathscr{L}_{off}} \frac{s_{off}}{s_{on}} N_{off} \ , \tag{5.5}$$

where N_{off} is the number of events from off-resonance data at $\sqrt{s_{off}} = 10.52$ GeV, $\sqrt{s_{on}} = 10.02$ GeV is the $\Upsilon(2S)$ on-resonance energy, the scale factor is $f_{scale} = \frac{\mathscr{L}_{on}}{\mathscr{L}_{off}} \frac{s_{off}}{s_{on}} = 0.6792$, and $\mathscr{L}_{on}$ and $\mathscr{L}_{off}$ are the integrated luminosities of the given data samples.

5.2. Trigger selection

Both signal processes produce three detectable particles: two charged pions, which have low transverse momentum; and a photon, which deposits energy on the ECL. The small number of charged tracks and their low momentum make them difficult to trigger on, thus the main L1 triggers used are related to the ECL. The main triggers produced by the GDL are *e_had*, *hie*, and *loe_fs_o*. The relative importance of these triggers varies with the A^0 and χ mass. Definitions of these triggers are shown in Table 5.1.

In most cases when the *loe_fs_o* trigger is produced by the GDL, the TOF detector also provides a trigger signal. This signal from the TOF determines the timing of the trigger, and the trigger signals from the Belle sub-detectors are retained at the GDL during the 1.85 μs latency from the timing signal. If the trigger signal of the TOF is not available, that of the ECL determines the timing. When the timing signal from the TOF is used, it is possible that only loe_fs_o is produced and e_had and hie are not produced at the GDL due to the timing. For instance, the ECL total deposited energy due to beam backgrounds can exceed the energy thresholds of the e_had or hie trigger, but the ECL trigger signals can be out-of-time with the TOF timing signal at the GDL. So then the loe_fs_o trigger is only produced by the GDL. Estimating the systematic uncertainty of the trigger efficiency is difficult in this case because TSIM does not simulate the timing. Thus we decided to use only these two triggers, e_had and hie, in this analysis. Although we decide to use only two triggers, it is worth to compare with using all triggers, to see what the potential improvement might be. Hence, we compare with the case of using all triggers when estimating efficiencies.

5.2.1. Trigger efficiency

We seek to validate the trigger efficiency for a photon energy of 0 - 7.0 GeV, which corresponds to an ECL total deposited energy of 0 - 7.5 GeV. To study L1 triggers for these energies, we generate 10^6 $\Upsilon(2S) \rightarrow \Upsilon(1S)\pi^+\pi^-$ with $\Upsilon(1S) \rightarrow \mu^+\mu^-$. The muons do not deposit energy on the ECL, therefore we can study the triggers from the low to the high photon energy region using beam backgrounds. It is important to also consider the effect of beam background on the trigger because, for the signal, mainly a single photon contributes to the ECL. We, therefore, include the ECL beam backgrounds in TSIM for all MC samples. The ECL total deposited energy for the trigger is defined as E_{ECL}^{trg}, which covers the polar angle range in the lab frame $-0.6235 < \cos\theta < 0.9481$. After tuning the thresholds of E_{ECL}^{trg}, we set them to be greater than 1.1 and 2.8 GeV for hie and e_had, respectively.

To validate the simulated trigger efficiency against experimental data, we define the relative efficiency of the triggers as follows:

$$\begin{aligned}\text{Relative efficiency of "}hie\text{"} &= N(hie \,\&\, e\_had)/N(e\_had)\\ \text{Relative efficiency of "}e\_had\text{"} &= N(hie \,\&\, e\_had)/N(hie)\end{aligned}$$

where N is the number of events satisfying the trigger conditions in parentheses. Figure 5.2 shows the relative efficiency versus E_{ECL}^{trg}. MC events without the beam backgrounds including in TSIM are not able to show the relative efficiency in the

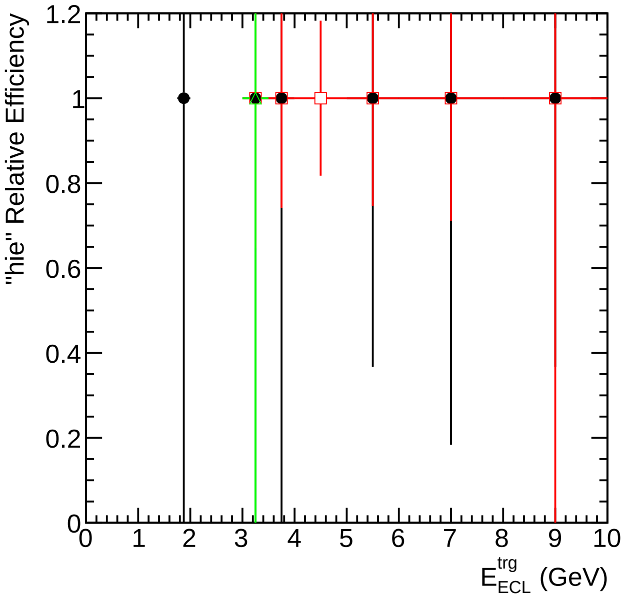

(a)

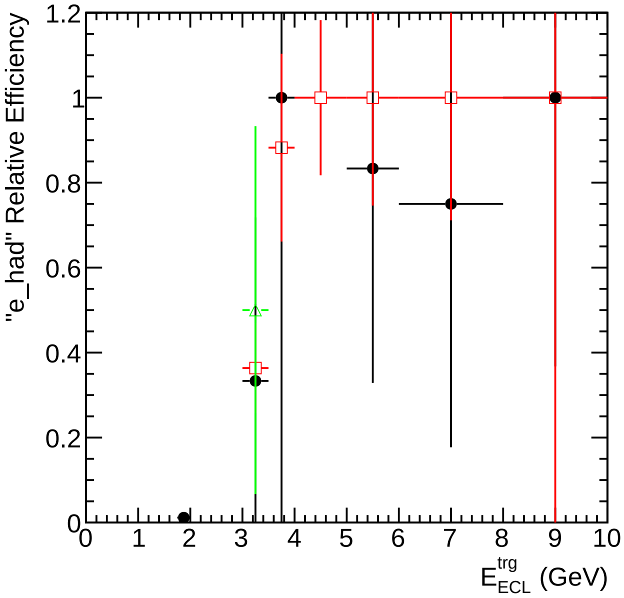

(b)

Figure 5.2.: Relative efficiency of *hie* (a) and *e_had* (b) as a function of E_{ECL}^{trg}. Black dots are experimental data and red open-squares and green open-triangles are MC events with and without beam background contribution in the triggers, respectively.

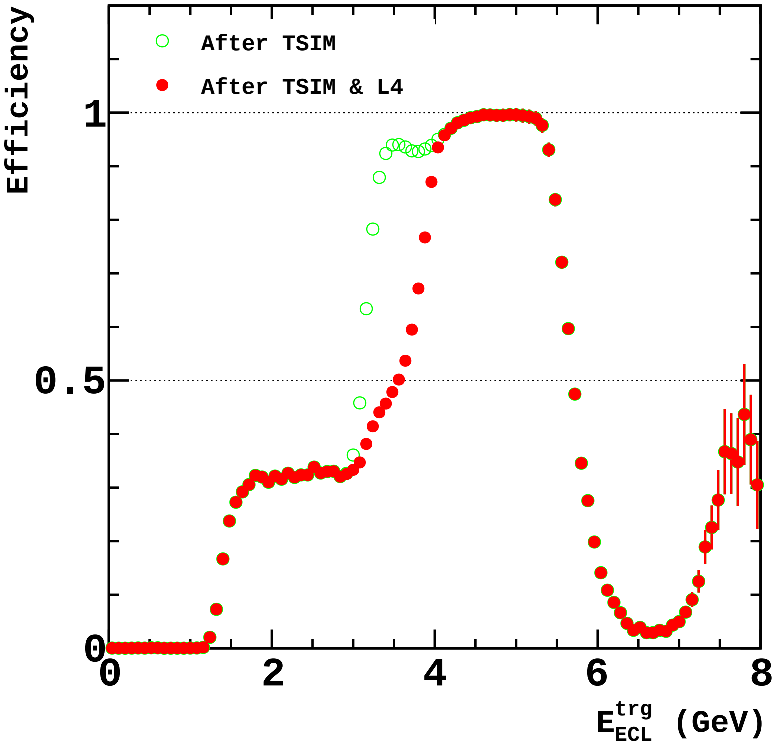

Figure 5.3.: Trigger efficiency versus energy deposit on the ECL for $M_\chi = 0.1$ GeV/c^2. Green circles show the L1 trigger efficiency and red dots show the total trigger efficiency with L1 and L4 triggers.

high E^{trg}_{ECL} region because they have an extremely low probability of firing the e_had trigger bit. These samples are limited by low statistics, however, the e_had relative efficiency reveals a potential discrepancy between data and MC. We further investigate this and find that the relative efficiency is correlated with amount of beam background included in TSIM. We attempt to correct this contribution; however, the efficiency is reduced in the entire E^{trg}_{ECL} range when background contribution is reduced. We conclude that there is some dependency on the deposited energy in the ECL, which we can not reproduce with TSIM. Thus we include the difference in means between the experimental data and the MC sample as a systematic uncertainty, rather than a correction.

These two triggers are applied to the signal and the background MC samples to account for the finite trigger efficiency of the detector. The efficiency strongly depends on the simulated particle masses. For the on-shell mode, the L1 trigger

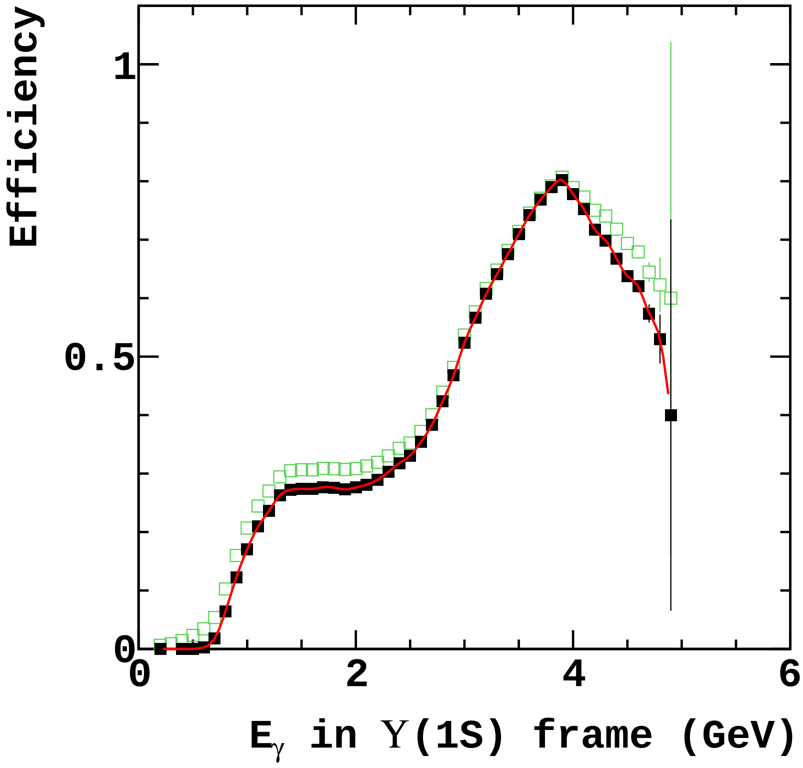

Figure 5.4.: Trigger efficiency as a function of E^*_γ. Black filled-squares and green open-squares are the $\epsilon_{\rm trig}(E^*_\gamma)$ of using the two trigger and all triggers, respectively.

efficiency is 46.9 (0.60) % for M_{A^0} = 0.1 GeV (9.2 GeV). For the off-shell mode, it is 53.8 (0.58) % for M_χ = 0.1 GeV (4.5 GeV). Furthermore, the L4 software trigger is also applied to the MC samples because it has already been applied to experimental data and becomes important for low-multiplicity events. The L4 trigger is described in Chapter 4. The L4 software trigger has an efficiency of 86.6 (19.5) % for M_{A^0} = 0.1 GeV (9.2 GeV) and 63.9 (19.6) % for M_χ = 0.1 GeV (4.5 GeV). The variation of trigger efficiency in signal samples is mainly due to the variation of the photon energy depending on M_{A^0} and M_χ. Figure 5.3 shows the trigger efficiency versus the total deposited energy on the ECL with the MC sample for M_χ = 0.1 GeV. The decrease of the efficiency above 5 GeV is due to the Bhabha event veto in the L1 trigger condition.

The trigger efficiency as a function of photon energy in the Υ(1S) frame, $\epsilon_{\rm trig}(E^*_\gamma)$, has to be estimated because it affects the photon energy spectrum in the signal and background samples. The $\epsilon_{\rm trig}(E^*_\gamma)$ is obtained from the signal MC samples as shown in the black filled-squares in Figure 5.4, and it is extracted with the histogram probability density function. The large uncertainty in the high energy region is due to low statistics of the maximum reachable photon energy in the signal MC samples. The green open-squares are the efficiency as a function of E_{γ}^{*} with the case of using all triggers. Using two L1 triggers results in nearly 100% efficiency loss in the low energy region compared with using all L triggers. In other regions the loss is less than 15%. The low energy region had $< 3\%$ efficiency even when using all triggers, thus the sensitivity was never good.

5.3. Event selection

5.3.1. Initial selection

We are looking for the two pions from the $\Upsilon(2S) \to \Upsilon(1S)\pi^{+}\pi^{-}$ decays, and no additional charged particles should be present in the event. Hence, none of the official skims in the Belle Library can be used. We, therefore, require an initial loose selection to skim for $\Upsilon(2S) \to \Upsilon(1S)\pi^{+}\pi^{-}$, $\Upsilon(1S) \to \gamma X$ events, where X can be A^0 or $\chi\chi$, as follows:

- Number of good charged tracks ($\mathrm{N}_{charged}$):
  At this stage, charged tracks are assumed to be pions and are classified as good charged tracks if they satisfy impact parameters $dr < 2.0$ cm and $|dz| < 4.0$ cm. Events which have exactly two good charged tracks with opposite charge are kept.

- Recoil mass (M_{recoil}):
  Recoil mass has to be between 9.40 GeV and 9.52 GeV. The PDG values for $M_{\Upsilon(1S)}$ and $\Gamma_{\Upsilon(1S)}$ are 9460.30 ± 0.25 MeV/c^2 and 54.02 ± 1.25 keV, respectively.

- Photon energy in the $\Upsilon(1S)$ frame (E_{γ}^{*}):
  We select the highest-energy photon in the CM frame and it has to be > 0.15 GeV in the $\Upsilon(1S)$ frame.

5.3.2. Particle identification and photon selection

Particle identification for a pion is performed with the charged track information from the sub-detectors: the ACC, the TOF, and the CDC. The information from these detectors is combined into the likelihood ratio defined as

$$\begin{aligned} \mathcal{L}_i &= \mathcal{L}_i^{ACC} \times \mathcal{L}_i^{TOF} \times \mathcal{L}_i^{CDC} && (5.6) \\ Prob(i:j) &= \frac{\mathcal{L}_i}{\mathcal{L}_i + \mathcal{L}_j} \ , && (5.7) \end{aligned}$$

where i is a kaon or pion. We also use the electron identification, eID, to suppress the electron fake contribution in this analysis. The eID uses sub-detector information from the ACC, TOF, CDC, and ECL detector, which is combined into a likelihood ratio with electron and hadron hypothesis. Two good charged tracks are classified as pions by applying the following particle identification requirements:

$$\begin{aligned} \mathrm{Prob}(\pi:K) &> 0.6 && (5.8) \\ e\mathrm{ID} &< 0.1 \ . && (5.9) \end{aligned}$$

93% of candidate events contain a pair of true pions. One of pions is contaminated by muon ($<$ 4%), electron ($<$ 2%), or protons ($<$ 0.1%).

The photon candidate, which is the highest-energy photon in the CM frame, is required to satisfy the following selections:

- ECL barrel region ($cos(\theta_\gamma)$):
  The photon candidate has to be detected in the ECL barrel region, -0.63 $<$ cosθ_γ $<$ 0.84, to suppress beam background contribution.

- Number of crystals (N_{hits}):
  The number of crystals in the ECL cluster for the photon candidate is greater than 2.

- E9/E25:
  The ratio of energy in a 3 × 3 and 5 × 5 array of crystals in the ECL surrounding the shower center is required to be > 0.9.

5.4. Background suppression

We require additional selection to further suppress background, aiming to maximize Figure of Merit (FOM), which is defined as:

$$\text{FOM} = \frac{S}{\sqrt{B}} \,,$$

where S and B are the number of signal and background events, respectively, after applying all other selections except the cut being evaluated. B is estimated from the sum of scaled $\Upsilon(2S)$ inclusive MC and scaled $\Upsilon(4S)$ off-resonance data samples in the signal region. One million signal events with $M_{A^0} = 0.1$ GeV and 9.2 GeV, which are the lowest and highest Higgs masses, are used to choose final selections. The optimization of the selection is performed both using the two triggers and all triggers; the results remain the same. The results and their distributions are shown in Appendix B and optimized selections are also applied to off-shell signal samples. Before starting optimization, we require a narrow range of recoil mass, $9.450 < M_{recoil} < 9.475$ GeV/c^2, to reduce backgrounds from outside of signal region.

5.4.1. Di-pion selection

To select pions from the $\Upsilon(2S) \to \pi^+\pi^-$, the two pion candidates are required to have a vertex χ^2 and opening angle between the two pions in the $\Upsilon(1S)$ frame, $cos(\theta^*_{\pi\pi})$ (see Figure 5.5a), satisfying the following rquirements:

$$\chi^2_{vtx} < 11$$
$$\cos(\theta^*_{\pi\pi}) < 0.0$$

The $cos(\theta^*_{\pi\pi})$ has a dependency on the mass of the signal samples due to the trigger efficiency, therefore we choose an average value between the two optimal selection criteria for the lowest and highest M_{A^0} samples.

5.4.2. Photon vetos

Photons are contributed by various non-signal sources, and additional selection criteria are necessary to suppress these backgrounds:

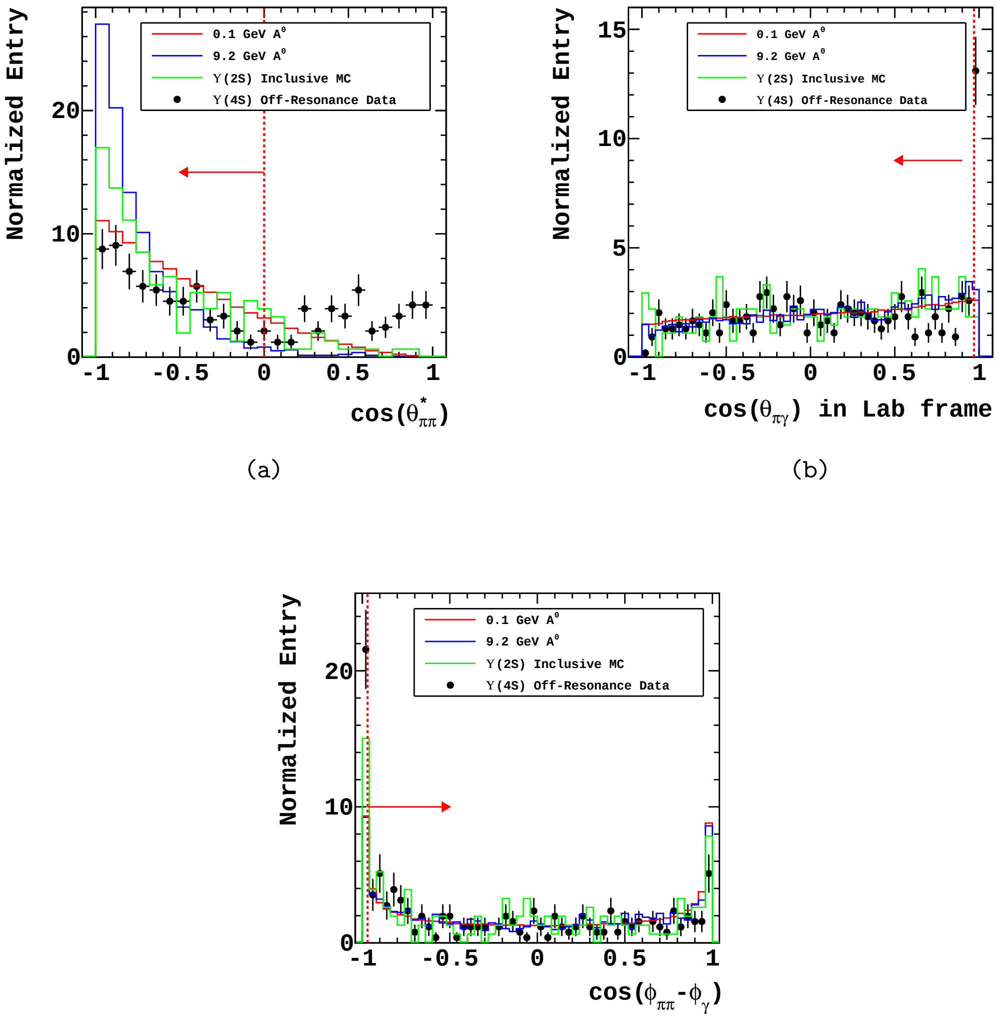

(a)

(b)

(c)

Figure 5.5.: Angular distributions for signal MC and background events. (a): opening angle between the two pion candidates in the $\Upsilon(1S)$ frame, (b): Bremsstrahlung photon distribution, (c): azimuthal angle difference between the dipion system and a photon. The dotted vertical red line indicates the cut values, and the arrow shows which events are kept by the cut.

- Bremsstrahlung rejection ($\cos(\theta_{\pi^{\pm}\gamma})$):
  The opening angle between the candidate photon and each charged track in the lab frame must satisfy $\cos(\theta_{\pi^{\pm}\gamma}) < 0.97$ (Figure 5.5b).
- QED background suppression ($\cos(\phi_{\pi\pi} - \phi_{\gamma})$):
  The QED process, $e^{+}e^{-} \to \gamma\pi^{+}\pi^{-}\cdots$, where the photon is radiated from the initial state (ISR) has a large azimuthal angle difference between the dipion system and the photon as shown in Figure 5.5c and is suppressed with $\cos(\phi_{\pi\pi} - \phi_{\gamma}) >$ -0.97.
- Multiple photon process suppression:
  Energy of the second most-energetic gamma (E_{γ}^{2}) in the CM frame has to be very small since a single photon is produced in the signal samples. We require E_{γ}^{2} in the $\Upsilon(1S)$ frame $<$ 0.18 GeV, which suppresses multiple photon processes and continuum events (Figure 5.6).
- Remaining energy in ECL (E_{ECL}^{remains}):
  E_{ECL}^{remains} is the sum of energy deposited in the ECL cluster ($E_{cluster}$) after excluding the clusters associated with the pions and the photon candidate. In order to suppress the beam background contribution, different energy thresholds are applied for different parts of the ECL: $E_{cluster} >$ 0.05 GeV for the barrel, $E_{cluster} >$ 0.10 GeV for the forward endcap, and $E_{cluster} >$ 0.15 GeV for the backward endcap. E_{ECL}^{remains} has to be near zero for signal, we require $<$ 0.18 GeV (Figure 5.7).

5.4.3. K_L veto

Neutral particles can also fake the photon of the signal. In order to study long-lived particles and neutral $\Upsilon(1S)$ final states with kaons, neutrons, or neutral pions, exclusive MC events with such decay modes are generated using EvtGen. Furthermore, $f_2(1270)$ and $f_2'(1525)$ from the $\Upsilon(1S)$ can also result in backgrounds when decaying to neutral kaons or pions. These modes are also generated, using recently measured decay modes. Most long-lived neutral particles interact directly in the ECL or KLM detectors without interacting in the CDC. We select such neutral hadronic particle candidates in two ways: more than 1 KLM hit with an associated ECL shower or more than 2 KLM hits without any ECL shower. We select one neutral particle

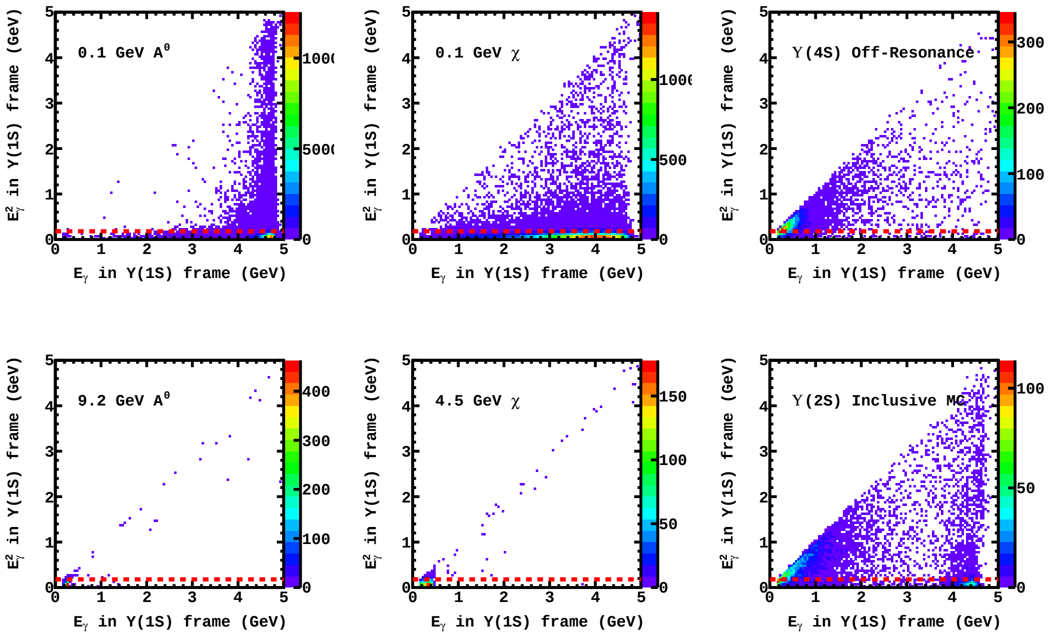

Figure 5.6.: E_γ^{2*} versus E_γ^* distribution. The red dashed line indicates our selection.

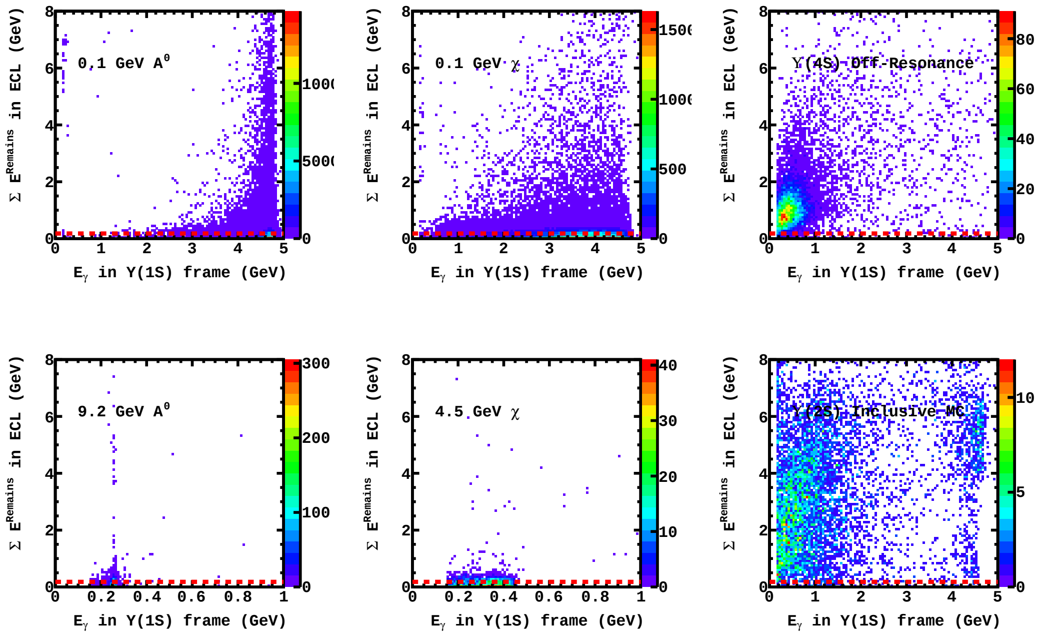

Figure 5.7.: Remaining energy deposited in ECL versus E_γ^* distribution. The red dashed line indicates our selection.

candidate per event by choosing the minimum $|\Delta\phi_{\gamma N}|$ defined as:

$$|\Delta\phi_{\gamma N}| \equiv |180 - |\phi_{\gamma} - \phi_{N}|| \,, \tag{5.10}$$

where ϕ_N is the azimuthal angle of the neutral particle. This is definition avoids sign problems in the azimuthal angle (Figure 5.8a) and enables us to choose the neutral particle furthest from the photon candidate.

Figures 5.8b and 5.8c show comparisons between hadronic decays and signal MC events. The two event types are well distinguishable with the variable $|\Delta\phi_{\gamma N}|$. Photons can leak into the KLM and be selected as the neutral particle as shown in the signal distributions. The FOM and the signal N-1 efficiency are shown in Figure 5.9 and the optimized selection is represented as a red vertical dashed line, $|\Delta\phi_{\gamma N}| > 20^{o}$. To optimize the selection, we used $\Upsilon(2S)$ inclusive MC samples instead of exclusive background MC. The $\mathrm{K_L}$ veto rejects 54% of $\Upsilon(1S) \to \gamma K_L^0 K_L^0$ $(n\bar{n})$, 98% of $\Upsilon(1S) \to \gamma f_2'(1525)$ events, and 95% of $\Upsilon(1S) \to \gamma f_2(1270)$. The difference between $f_2'(1525)$ and $f_2(1270)$ is due to larger BF of $\pi^0\pi^0$ mode in $f_2(1270)$. Most of π^0s from $f_2(1270)$ are rejected by the $E_{ECL}^{\mathrm{remains}}$ selection.

5.4.4. Remaining backgrounds

The distributions of remaining backgrounds from a 400×10^6 $\Upsilon(2S)$ inclusive MC sample and $\Upsilon(4S)$ off-resonance experimental data, after applying all selections discussed above, are shown in Figure 5.10 and Figure 5.11, respectively.

Backgrounds from the $\Upsilon(2S)$

The truth information in the $\Upsilon(2S)$ MC sample is used to categorize the remaining backgrounds and shows three main event types as follows:

- $\Upsilon(2S) \to \tau^+\tau^-$:
  $\tau^{\pm}$ can decay to $\pi^{\pm}\nu_{\tau}$ + anything. Anything can be single or multiple π^0 or nothing. $\pi^{\pm}$ from $\tau^{\pm}$ can have low momentum because of ν_{τ} and can pass the selection.
- Leptonic decays, $\Upsilon(2S) \to \pi^+\pi^-\Upsilon(1S), \Upsilon(1S) \to l^+l^-$:
  $l^{\pm}$ is any charged lepton, electron, muon, or tau. Such events can pass the

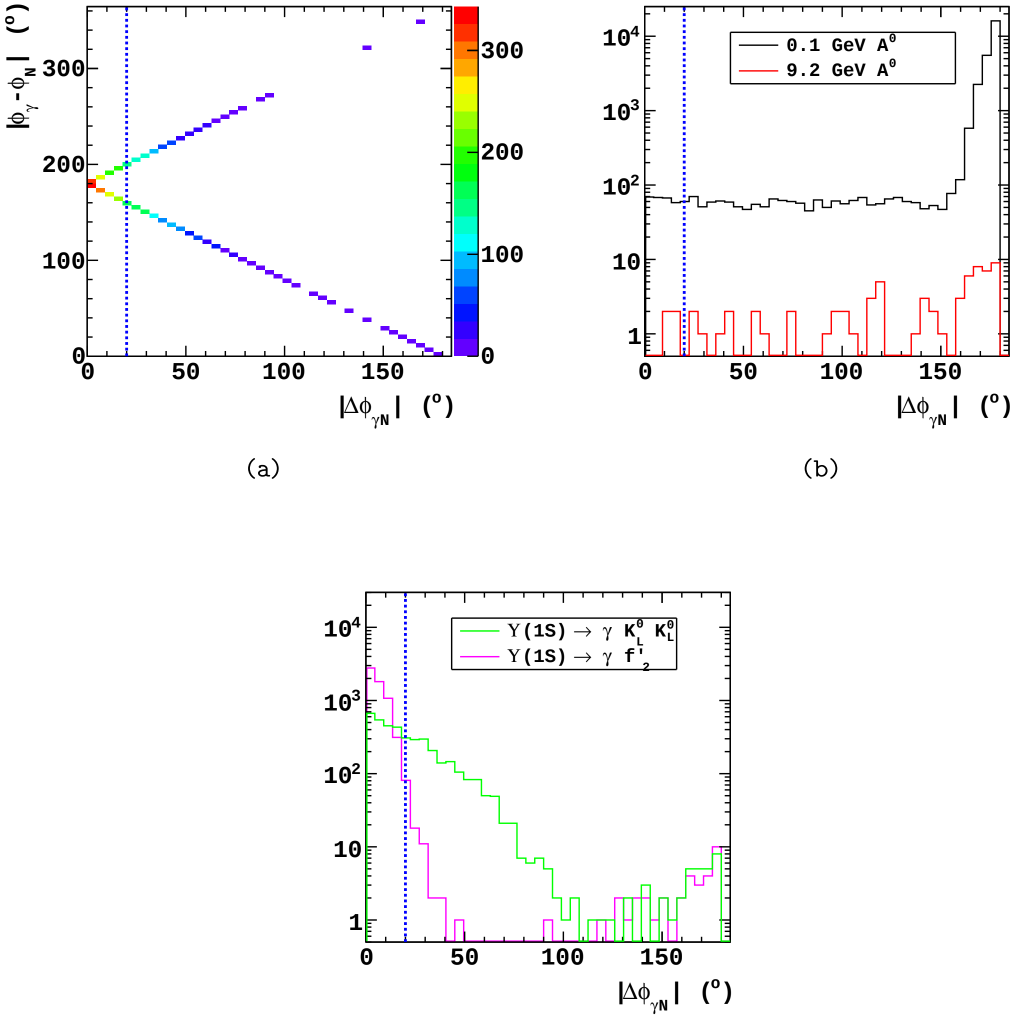

(a)

(b)

(c)

Figure 5.8.: $|\Delta\phi_{\gamma N}|$ distribution for the neutral particle candidate. (a): absolute azimuthal angle difference versus $|\Delta\phi_{\gamma N}|$ with $\Upsilon(1S) \rightarrow \gamma K_L^0 K_L^0$ MC, (b): 1D histogram for signal MC, (c): for exclusive background MC.

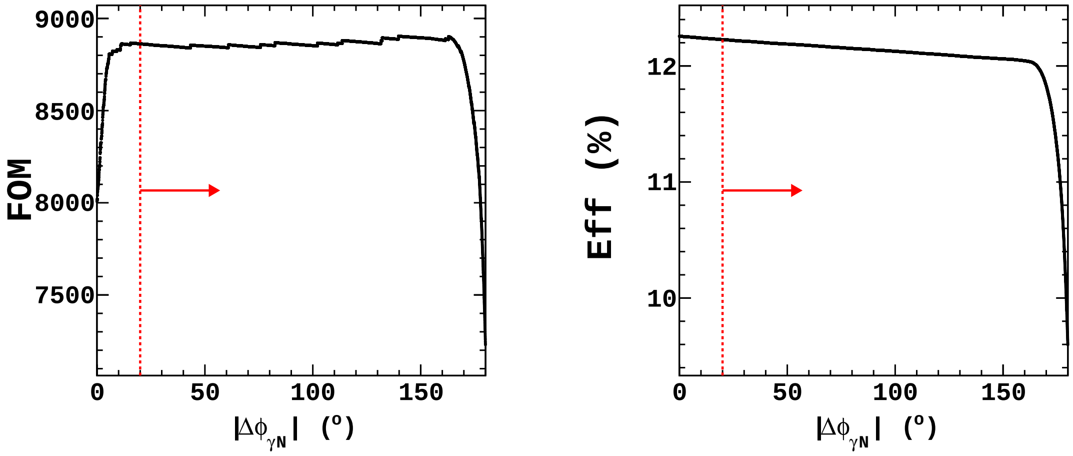

Figure 5.9.: Optimization of K_L veto with $M_{A^0} = 0.1$ GeV. Instead of using exclusive background MC samples, $\Upsilon(2S)$ inclusive MC and $\Upsilon(4S)$ off-resonance data are used. Left: Figure of Merit, right: signal efficiency as a function of $|\Delta\phi_{\gamma N}|$.

selection when leptons escape through the beam pipe. The contribution of tau is smaller than other leptons, due to the decay process of taus with short life time. The photon candidates mostly originate from the Final State Radiation (FSR) or beam backgrounds.

- Hadronic decays, $\Upsilon(2S) \to \pi^+\pi^-\Upsilon(1S), \Upsilon(1S) \to \gamma$ hadrons :
  Hadrons can be neutral particles, such as K_L, π^0, and n^0, or charged. Charged particles mainly escape through the beam pipe as in the case of leptonic decays. The photon from $\Upsilon(1S) \to \gamma$ hadrons can contribute as a peaking background at high photon energies.

Backgrounds from off-resonance

We estimate background from processes other than $e^+e^- \to \Upsilon(2S)$ using $\Upsilon(4S)$ off-resonance experimental data. We loosen the initial recoil mass selection to retain more events. Figure 5.12 shows the distributions of the $\pi^+\pi^-$ invariant mass ($M_{\pi\pi}$), the $\pi^+\pi^-\gamma$ invariant mass ($M_{\pi\pi\gamma}$), and $M_{\pi\pi\gamma}$ versus E_γ in $\Upsilon(1S)$ frame. A peak at $M_{\pi\pi} \approx 0.5$ GeV matches with the mass of K_S and another peak at $M_{\pi\pi\gamma} \approx 0.95$ GeV corresponds to the mass of $\eta'(958)$. As a result, the off-resonance events not only contribute as continuous backgrounds but also produce a peaking background

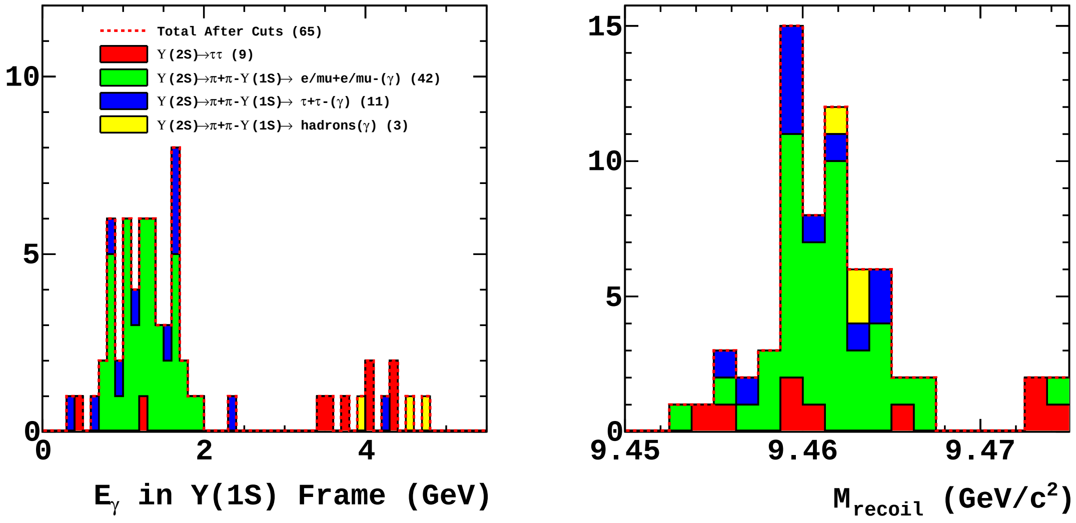

Figure 5.10.: Categorized remaining backgrounds, estimated from 400 million Υ(2S) inclusive MC events. Left: photon energy spectrum in the Υ(1S) frame. Right: Υ(1S) recoil mass distribution.

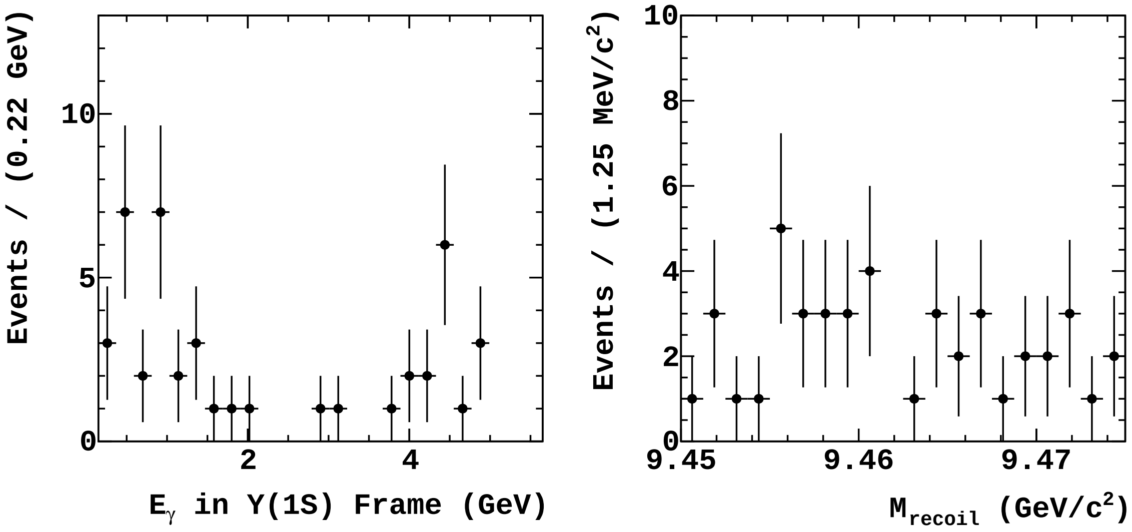

Figure 5.11.: Distributions for the photon energy spectrum in Υ(1S) frame (left) and the Υ(1S) recoil mass (right) from Υ(4S) off-resonance data.

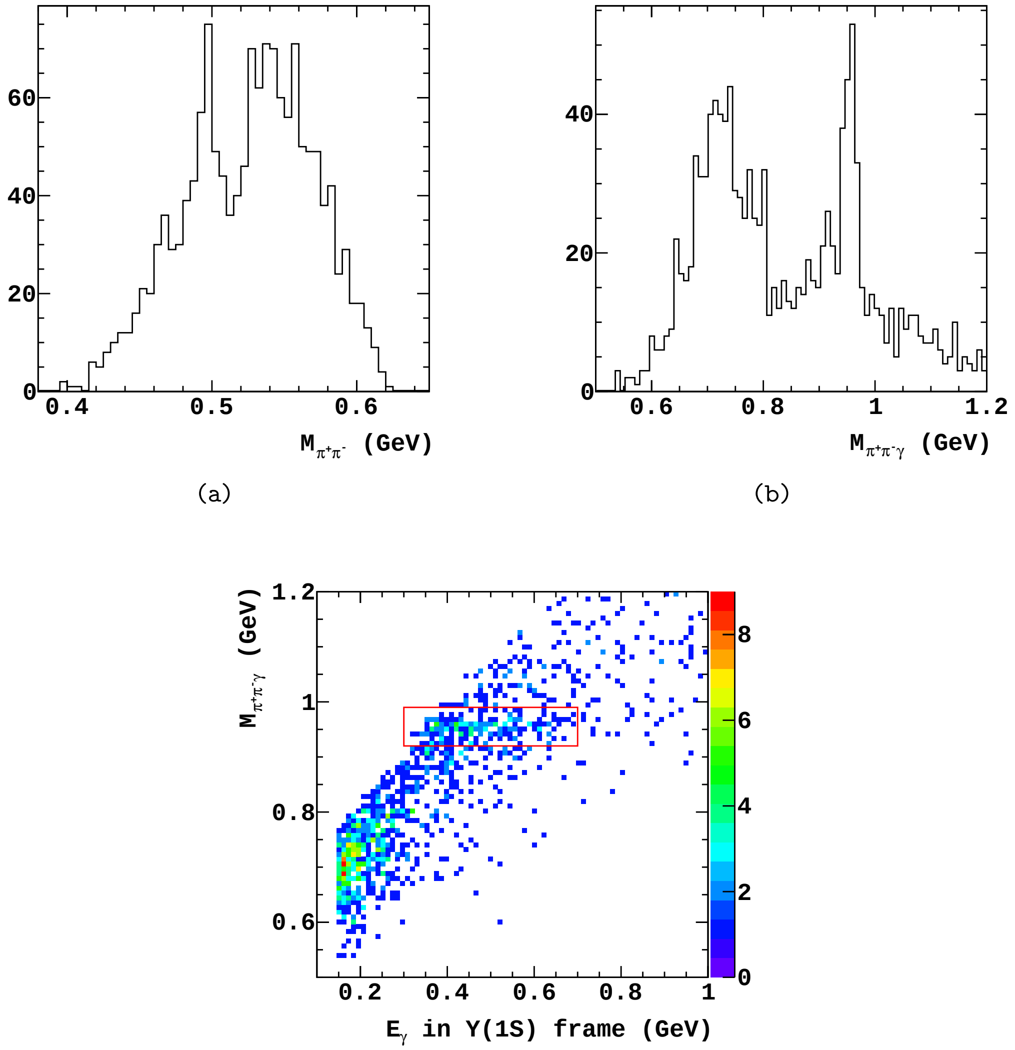

(a) (b)

(c)

Figure 5.12.: Invariant mass distributions with loose recoil mass selection. (a): $M_{\pi\pi}$ distribution, (b): $M_{\pi\pi\gamma}$ distribution, (c): $M_{\pi\pi\gamma}$ vs. E^*_γ

	$\Upsilon(2S) \to \tau\tau$	$\Upsilon(2S) \to \Upsilon(1S)\pi^+\pi^-$				Continuum
		$\Upsilon(1S)$ Leptonic BG			$\Upsilon(1S)$ Hadronic BG	
		$\tau^+\tau^-$	e^+e^-	$\mu^+\mu^-$		
Efficiency ($\times 10^{-5}$)	0.11 ± 0.04	0.58 ± 0.18	1.28 ± 0.27	1.05 ± 0.24	0.004 ± 0.003	-
Expected yield	3.5 ± 1.2	4.2 ± 1.3	8.5 ± 1.8	7.3 ± 1.7	1.2 ± 0.7	29.9

Table 5.2.: Estimated number of background in the signal region

in the low photon energy region from the decays of η'. However, they don't produce a peak in the recoil mass spectrum.

- Non-peaking background in the E^*_γ distribution:
  QED processes or two-photon processes with hadronic particles in the final state contribute as a smooth background with γ_{ISR} or the photons from π^0. Two pions are produced directly or via secondary processes such as $K_S \to \pi^+\pi^-$. The γ_{ISR} may contribute as a high energy photon and the $\pi^0 \to \gamma\gamma$ process contributes as soft photons.

- Peaking background in the E^*_γ distribution:
  The η' is produced by a two-photon process, $e^+e^- \to e^+e^-\gamma^*\gamma^* \to e^+e^-\eta'$, and decays with a resonant mode, $\eta' \to \rho^0\gamma \to \pi^+\pi^-\gamma$, or a non-resonant mode, $\eta' \to \pi^+\pi^-\gamma$. The beam particles, e^+e^-, escape along the beam pipe. The tail of the $\rho^0(770)$ can satisfy the recoil mass (dipion mass) selection due to the broad decay width ($\Gamma = 149.1 \pm 0.8$ MeV), eventually both modes can contribute as a background in the signal region. Even though the $\cos(\phi_{\pi\pi} - \phi_\gamma)$ selection suppresses about 40% of η' events, still it produces a peak at $E^*_\gamma \approx 0.4$ GeV as shown in Figure 5.11 (left) and the red box in Figure 5.12 (c).

Estimate of background contribution in $\Upsilon(2S)$ experimental data

We estimate the expected number of backgrounds in $\Upsilon(2S)$ experimental data. In order to obtain explicit number of backgrounds from the $\Upsilon(2S)$, we obtain the efficiency of each background channel from the 400×10^6 $\Upsilon(2S)$ inclusive MC events and estimate expected background yields. The contribution of continuum background in the signal data is estimated from $\Upsilon(4S)$ off-resonance experimental data, scaled to the $\Upsilon(2S)$ on-resonance luminosity using equation 5.5. The result is shown in Table 5.2. A total of 21.2 ± 2.9 background event from $\Upsilon(2S) \to \Upsilon(1S)\pi^+\pi^-$ decays is expected.

5.5. Signal efficiency

The signal efficiency, ϵ, must be obtained to calculate the signal BF or to set a limit. We obtained ϵ from MC as shown in Table 5.3, where all selection criteria and N-1 efficiency values are summarized. The N-1 efficiency is defined as

$$\text{N-1 Efficiency} = \frac{N(\text{after all selections})}{N(\text{after all other selections except the cut being evaluated})} .$$

Total efficiency is computed as a function of M_{A^0} or M_χ, and it is shown in black filled-squares in Figure 5.13. The low efficiency at high M_{A^0} is due to the low trigger efficiency of low energy photons. The low and middle region of M_{A^0} is affected by the Bhabha event veto and Cosmic ray veto in the L1 trigger. The signal efficiency varies between 0.001% and 14% for the on-shell signal and 0.0007% and 9.4% for the off-shell signal sample. The green open-squares in Figure 5.13 are the signal efficiency of using all triggers. The efficiency of using the two triggers is lower by about 10% in the low mass region and by nearly 100% in the high mass region than using all triggers. We exclude the highest mass region due to the extremely low signal efficiency, from here on we only keep the signal mass region $M_{A^0} < 8.97$ GeV/c^2 and $M_\chi < 4.44$ GeV/c^2. We use a Spline function to extract the efficiency curve, shown as red solid lines in Figure 5.13.

Selections	Signal MC 0.1 GeV A^0	Signal MC 9.2 GeV A^0	Υ(2S) Inclusive MC	Off-Resonance DATA
Initial Selection	46.80 %	42.84 %	0.0427 %	0.0284 %
+ Two Trigger Conditions	24.01 %	0.30 %	0.0198 %	0.0168 %
+ L4 Trigger	22.70 %	0.30 %	0.0197 %	-
Number of Events	226976	2958	78672	265554
Vertex Chi2 ($\chi^2_{vtx} < 11$)	97.64	100.00	97.01	89.90
Prob(π:K) (>0.6)	99.68	100.00	98.48	100.00
EID (< 0.1)	94.34	100.00	86.67	54.32
Cos($\theta^*_{\pi\pi}$) (< 0.0)	85.24	83.33	77.38	44.44
M_{recoil} (9.450 < M < 9.475 GeV)	97.21	90.91	52.85	15.94
ECL Barrel	98.84	28.57	31.10	68.75
Number of Crystal (> 2)	100.00	76.92	64.36	91.67
E9/E25 (> 0.9)	99.49	100.00	97.01	84.62
Bremsstrahlung (cos(θ) < 0.97)	96.19	90.91	91.55	74.58
E^2_γ in $\Upsilon(1S)$ frame (< 0.18 GeV)	98.62	90.91	92.86	93.62
Cos($\phi_{\pi\pi}$-ϕ_γ)(> -0.97)	92.07	100.00	84.42	89.80
KL Veto	99.79	100.00	43.33	100.00
Remaining E_{ECL} (< 0.18 GeV)	80.47	20.41	11.34	7.80
Total Efficiency	11.04 %	0.0010 %	0.00002 %	2.78×10^{-6} %
Retainning Number of Events	110445	10	65	44

Table 5.3.: Summary of selection with N-1 efficiency

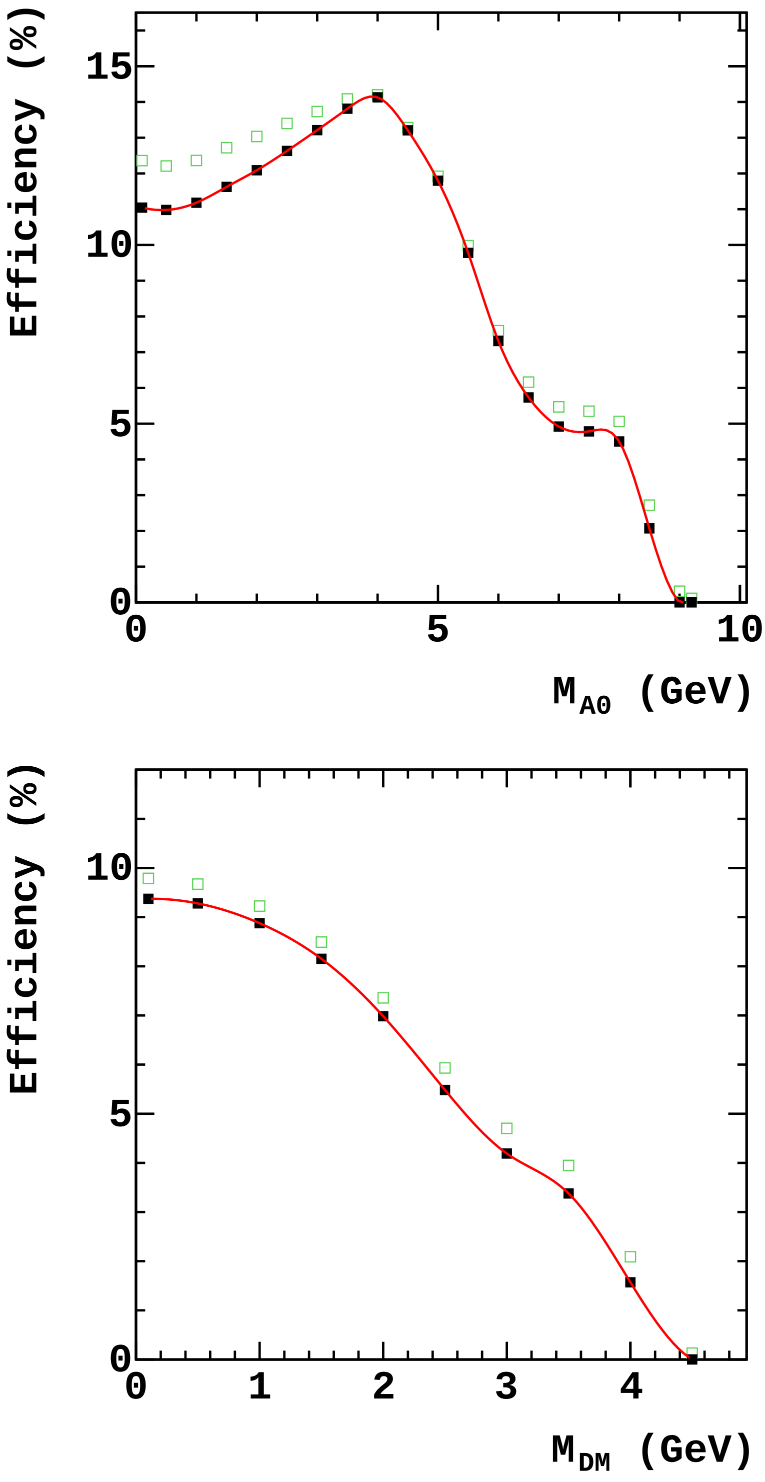

Figure 5.13.: Reconstruction efficiency for the on-shell and the off-shell process versus M_{A^0} and M_χ, respectively, after all selections. Black filled-squares and green open-squares are the efficiency when using two triggers and using all triggers, respectively. Red solid lines are the Spline functions used for interpolation.

5.6. Probability density functions

In order to extract the signal, we construct the probability density functions (PDFs) for the signal and background events. We expect extremely low statistical samples thus good understanding in the background and signal events is required. Instead of constructing each PDF for every kind of irreducible backgrounds, we simply divide them into three categories: leptonic decays, hadronic decays, and the continuum. The tau-pair production from the $\Upsilon(2S)$ has a peak neither in the recoil mass distribution nor in the photon energy spectrum; therefore, we regard the $\Upsilon(2S) \to \tau^+\tau^-$ events as continuum backgrounds and use scaled data samples of the $\Upsilon(4S)$ off-resonance and the $\Upsilon(2S) \to \tau^+\tau^-$ events to construct the continuum PDF.

5.6.1. Recoil mass PDF

The recoil mass PDF for the $\Upsilon(2S)$ on-resonance and continuum samples are constructed with all triggers to increase statistics. The triggers could affect the recoil mass PDF, but we neglect the effect because it is small as shown on the efficiency difference between the trigger conditions. The momentum and angular distributions of the pions in the $\Upsilon(2S) \to \pi^+\pi^-\Upsilon(1S)$ transition has a small discrepancy between the MC and experimental data thus we use the $\Upsilon(2S) \to \pi^+\pi^-\Upsilon(1S)$,$\Upsilon(1S) \to \mu^+\mu^-$ experimental data to construct a PDF of the $\Upsilon(1S)$ recoil mass. The $\Upsilon(1S)$ recoil mass distribution for the signal and background events from the $\Upsilon(2S) \to \pi^+\pi^-\Upsilon(1S)$ is described as a double-side Crystal Ball (CB) function:

$$f(M_{recoil}) \propto \begin{cases} \left(\frac{n_1}{|\alpha_1|}\right)^{n_1} \exp\left(-\frac{|\alpha_1|^2}{2}\right) \left(\frac{n_1}{|\alpha_1|} - |\alpha_1| - \frac{E^*_\gamma - \mu}{\sigma}\right)^{-n_1} & \text{, for } \frac{E^*_\gamma-\mu}{\sigma} < -\alpha_1 \\ \exp\left(-\frac{(E^*_\gamma-\mu)^2}{2\sigma^2}\right) & \text{, for } -\alpha_1 \leqslant \frac{E^*_\gamma-\mu}{\sigma} < \alpha_2 \\ \left(\frac{n_2}{|\alpha_2|}\right)^{n_2} \exp\left(-\frac{|\alpha_2|^2}{2}\right) \left(\frac{n_2}{|\alpha_2|} + |\alpha_2| - \frac{E^*_\gamma - \mu}{\sigma}\right)^{-n_2} & \text{, for } \alpha_2 \leqslant \frac{E^*_\gamma-\mu}{\sigma} \end{cases} \tag{5.11}$$

where μ and σ are the mean and sigma of the recoil mass distribution, α_1 and α_2 are the cutoff term for left and right side, and n_1 and n_2 are the shape parameters. We fix the two cutoff parameters, α_1 and α_2, to 1.5 and 1.2, respectively. Other

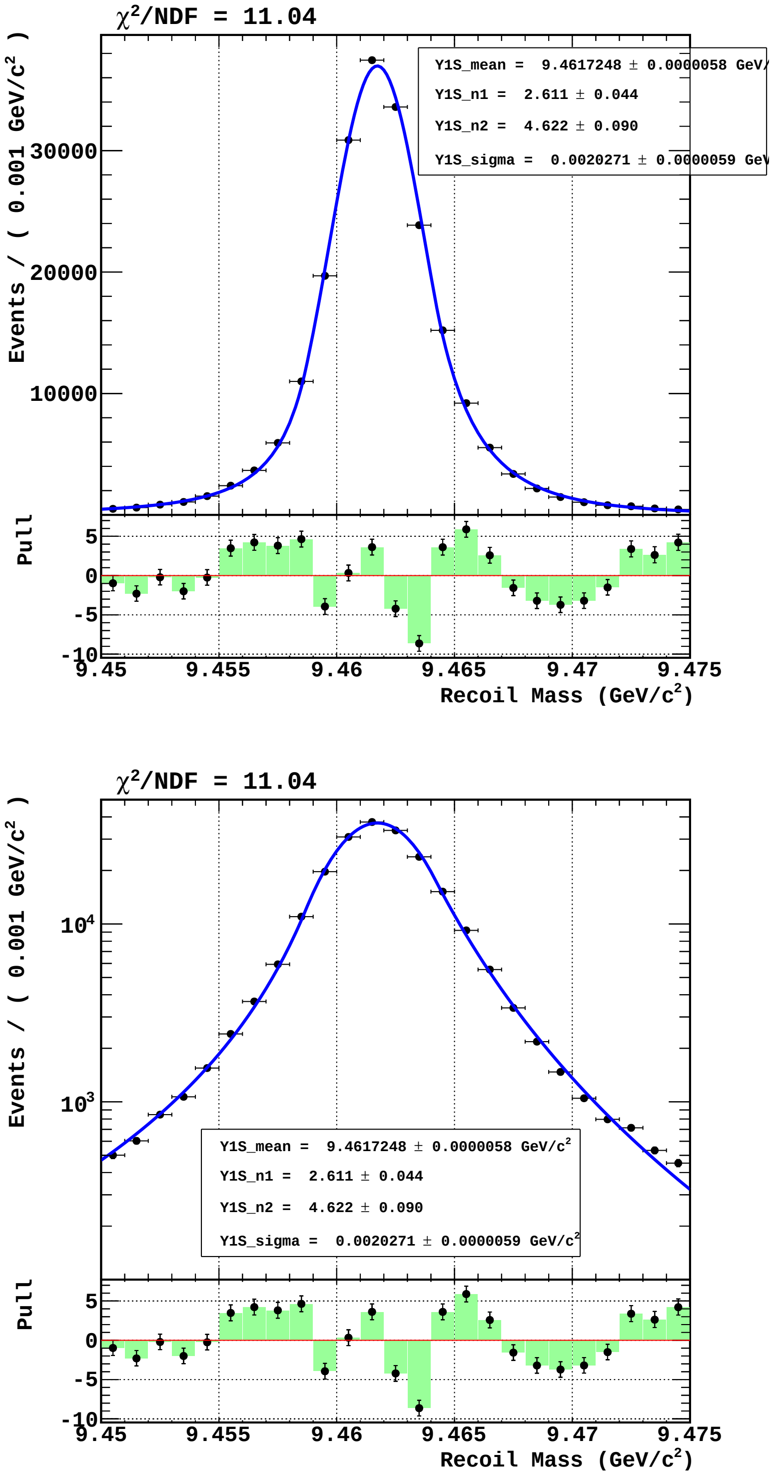

Figure 5.14.: Recoil mass distribution with PDF for the signal and background from $\Upsilon(1S)$ decays. Top: linear scale, bottom: log scale.

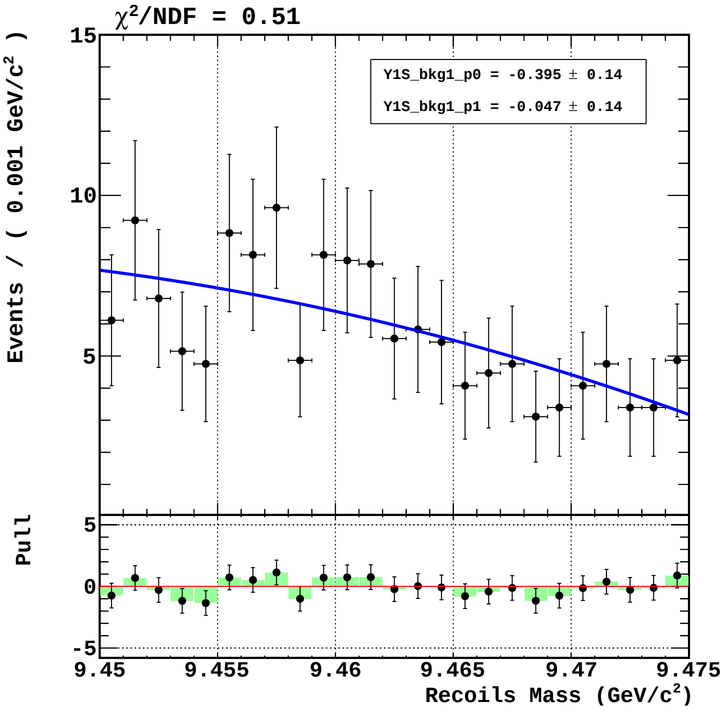

Figure 5.15.: Continuum background PDF in the recoil mass distribution.

parameters are floated and the results are shown in Figure 5.14. The PDF for the continuum background events in the recoil mass distribution is a second degree Chebychev polynomial function, as shown in Figure 5.15.

5.6.2. Photon energy PDF

The effect of the trigger efficiency in the photon energy spectrum is considered independently as a function of photon energy rather than constructing full PDF directly. The $\epsilon_{\text{trig}}(E_\gamma^*)$ is obtained in Section 5.2.1, and we implement the product of a PDF with the $\epsilon_{\text{trig}}(E_\gamma^*)$ to construct a photon energy PDF.

On-shell signal PDF

A Crystal Ball (CB) function is used for the photon energy PDF of on-shell production, $\Upsilon(1S) \to \gamma A^0$, as

$$f(E^*_\gamma)_{\text{on-shell}} \propto \epsilon_{\text{trig}}(E^*_\gamma) \times \begin{cases} \exp(-\frac{(E^*_\gamma-\mu)^2}{2\sigma^2}) & \text{, for } \frac{E^*_\gamma-\mu}{\sigma} > -\alpha \\ \left(\frac{n}{|\alpha|}\right)^n \exp\left(-\frac{|\alpha|^2}{2}\right) \cdot (\frac{n}{|\alpha|} - |\alpha| - \frac{E^*_\gamma-\mu}{\sigma})^{-n} & \text{, for } \frac{E^*_\gamma-\mu}{\sigma} \leqslant -\alpha \end{cases} \tag{5.12}$$

where μ and σ are the mean and sigma of the Gaussian part, α is the cutoff term, and n is the shape parameter of the CB function. Figure 5.16 and Figure 5.17 show examples of PDFs for $M_{A^0} = 0.1$ GeV and 8.5 GeV, respectively. Appendix C.1 shows fits for other mass values. The 9.0 GeV M_{A^0} sample do not retain enough statistics to construct the PDF; we exclude this sample from extracting the PDF parameters. We obtain the CB parameters as a function of M_{A^0} and the results are shown in Figure 5.18. The obtained parameter functions are extrapolated to $M_{A^0} <$ 9.0 GeV for the likelihood scan.

Off-shell signal PDF

The photon energy spectrum of the off-shell production, $\Upsilon(1S) \to \gamma\chi\chi$, has a broad distribution due to the multi-body decay process, which is described as

$$f(E^*_\gamma)_{\text{off-shell}} \propto \epsilon_{\text{trig}}(E^*_\gamma) \times \frac{(E^*_\gamma)^p}{1+\exp\left(s\cdot(E^*_\gamma-\beta)\right)} \times \frac{1}{1+\exp\left(s'\cdot(E^*_\gamma-\beta')\right)} \quad . \tag{5.13}$$

The parameters s and $s' = k \cdot s$ describe the slope of the function, β and β' decide the threshold of the photon energy, and the parameter p describes the shape of the slope of the function and is fixed as $p = 1$. Figure 5.19 shows examples of PDFs for $M_\chi = 0.1$ GeV and 4.0 GeV, respectively. Appendix C.2 shows the fit results with the different MC samples and the dependence of the parameters on M_χ is shown in Figure 5.20. The parameter functions for the off-shell process are extrapolated to $M_\chi < 4.5$ GeV.

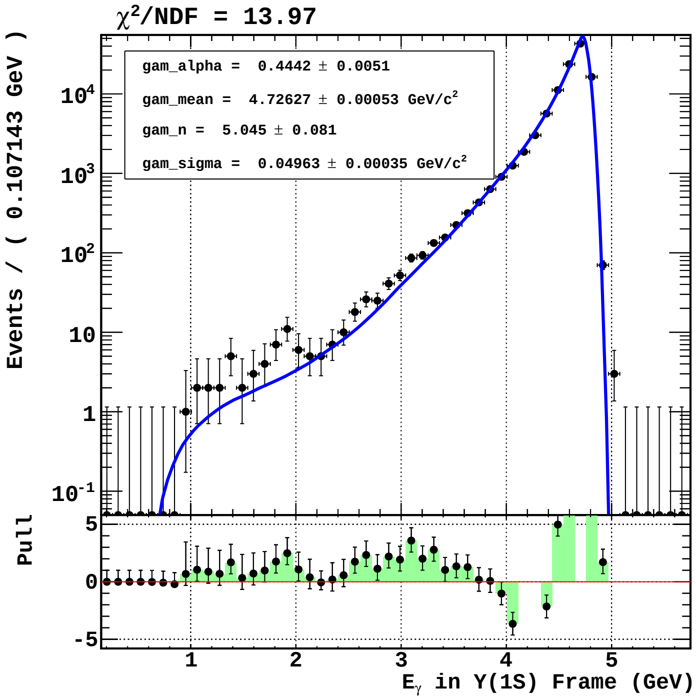

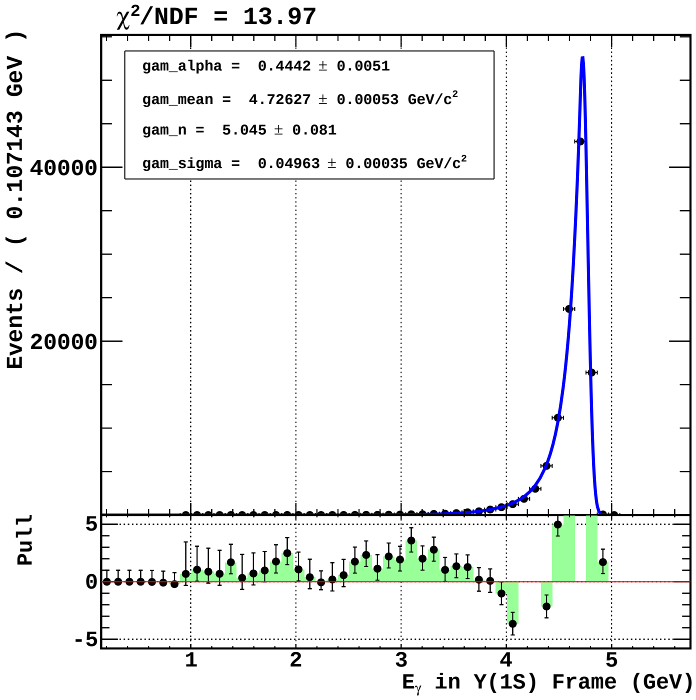

Figure 5.16.: Photon energy spectrum with a CB PDF for $M_{A^0} = 0.1$ GeV. Top: log scale, bottom: linear scale.

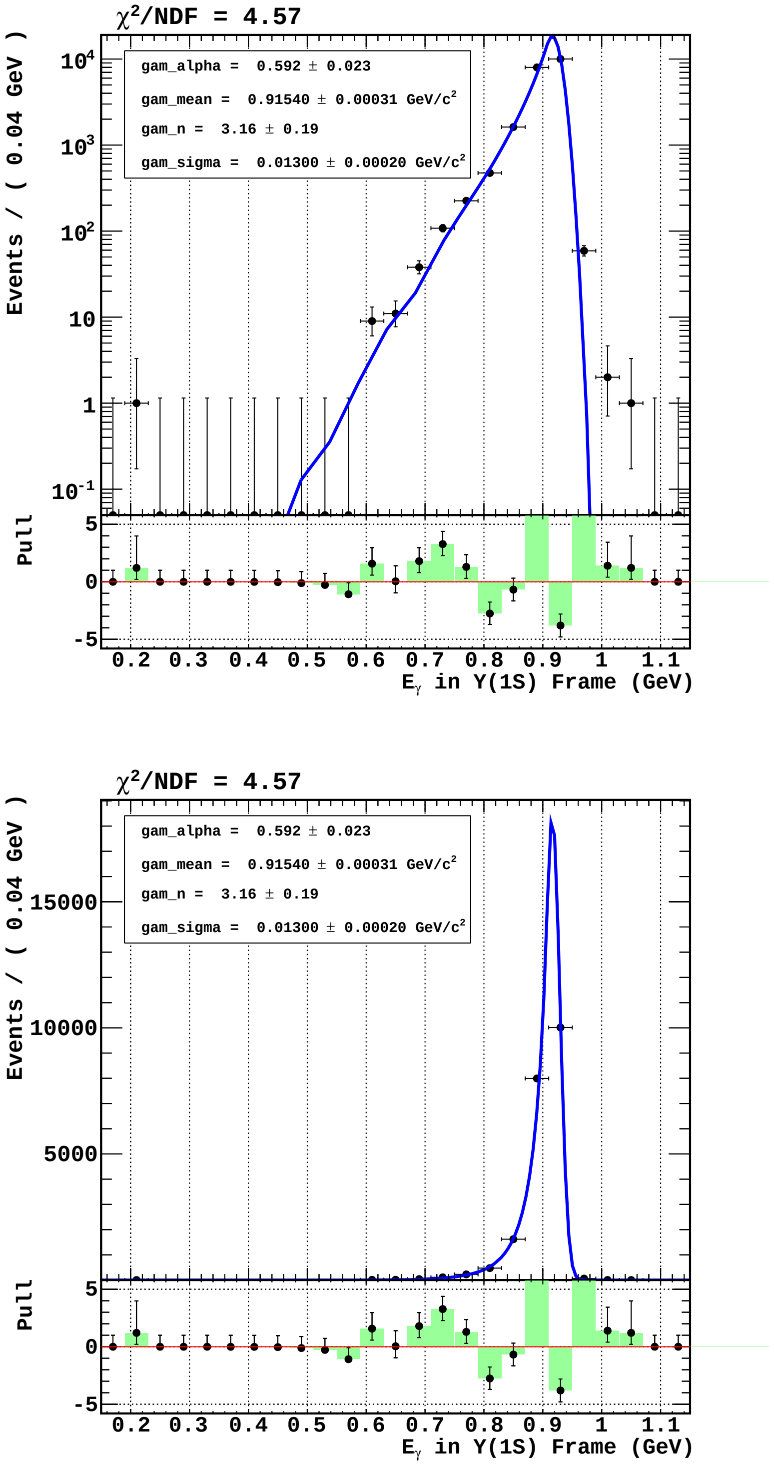

Figure 5.17.: Photon energy spectrum with a CB PDF for $M_{A^0} = 8.5$ GeV. Top: log scale, bottom: linear scale.

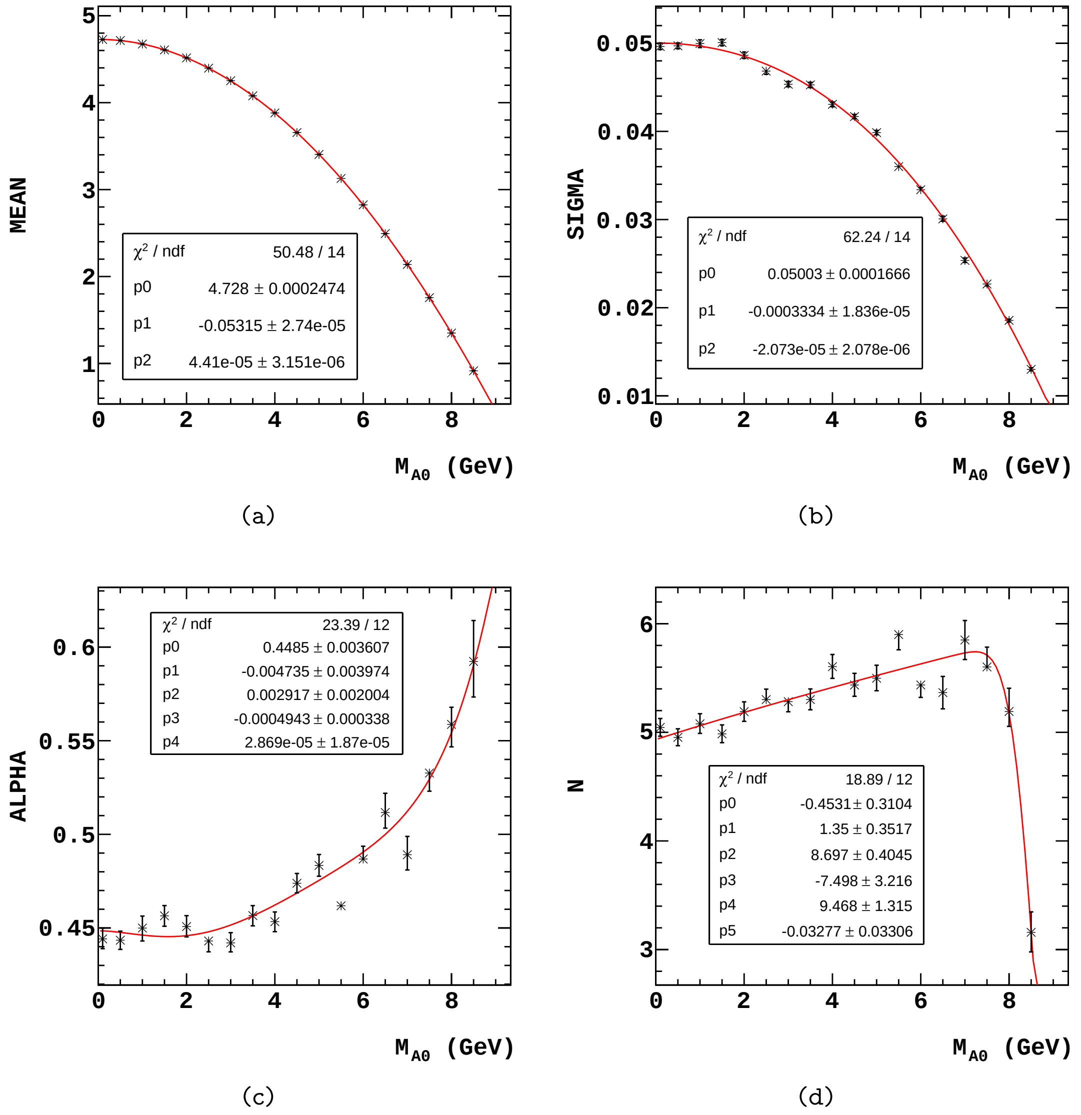

Figure 5.18.: Dependence of Crystal Ball (CB) parameters on M_{A^0}. (a) The mean of the Gaussian term in the CB function, (b) the sigma of the Gaussian term , (c) the cutoff term of the CB tail, and (d) the power-law of the CB tail.

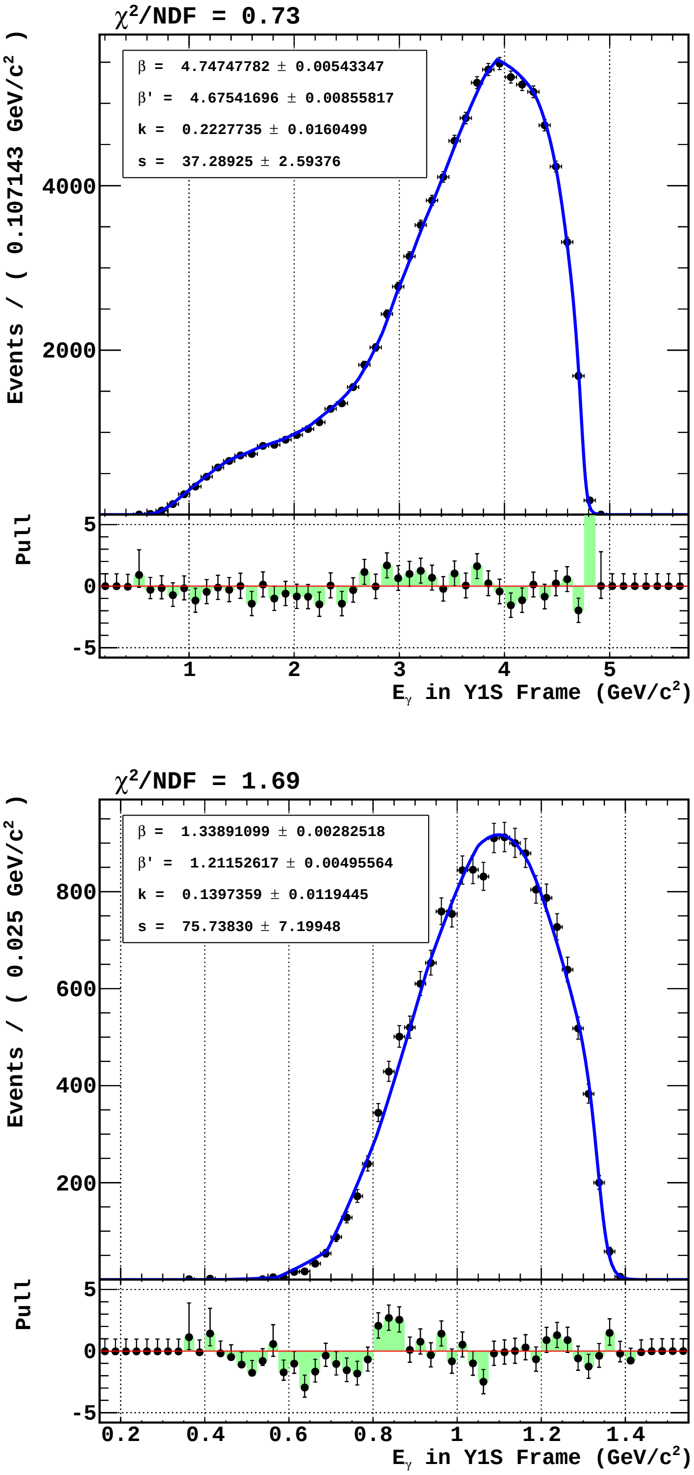

Figure 5.19.: The off-shell signal PDF with the $M_\chi = 0.1$ GeV (top) and 4.0 GeV (bottom).

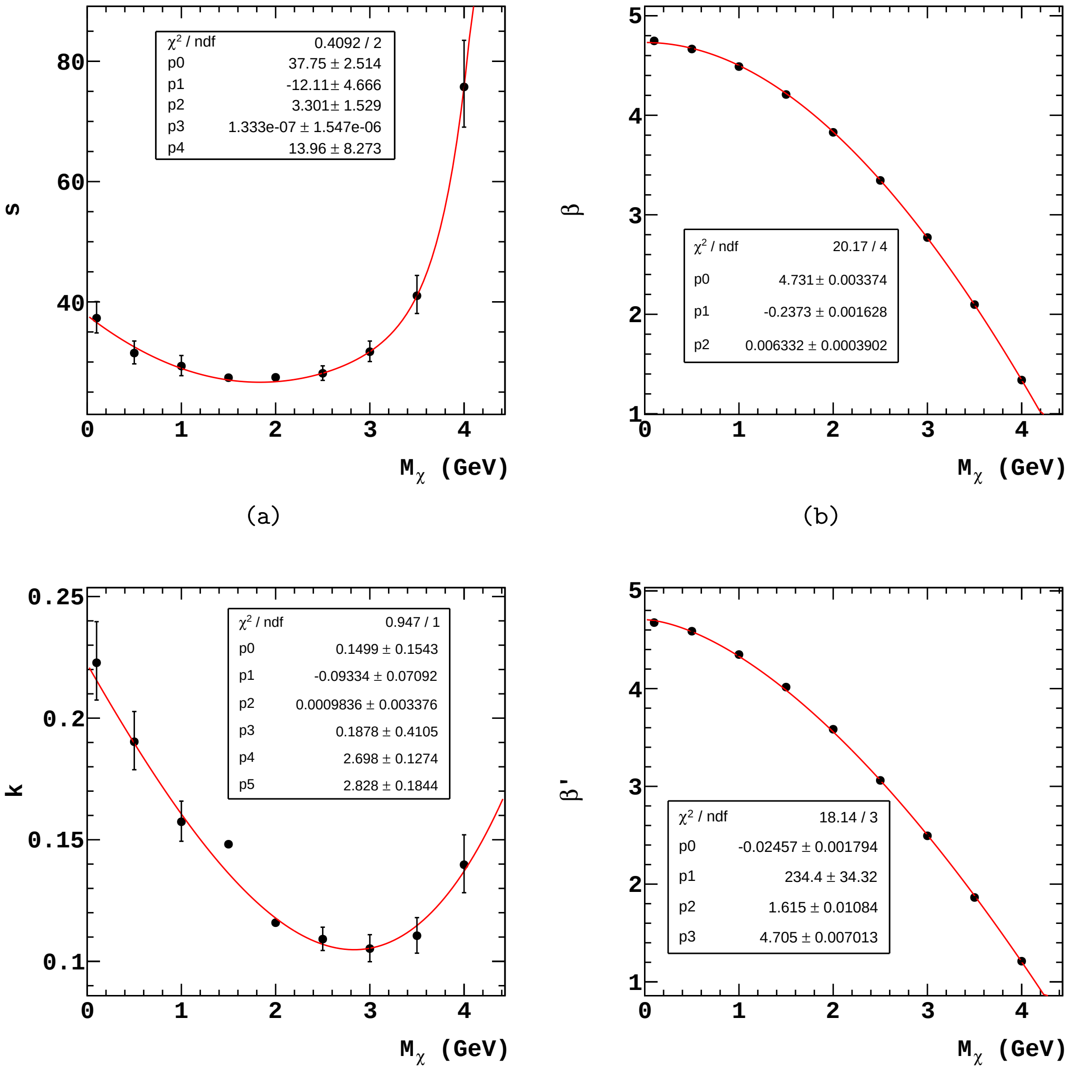

Figure 5.20.: Dependence of the off-shell signal PDF parameters on M_χ. (a) s, the slope parameter, (b) β, the cutoff term, (c) k ($s' = k \cdot s$), the relative slope parameter, and (d) β', the second cutoff term.

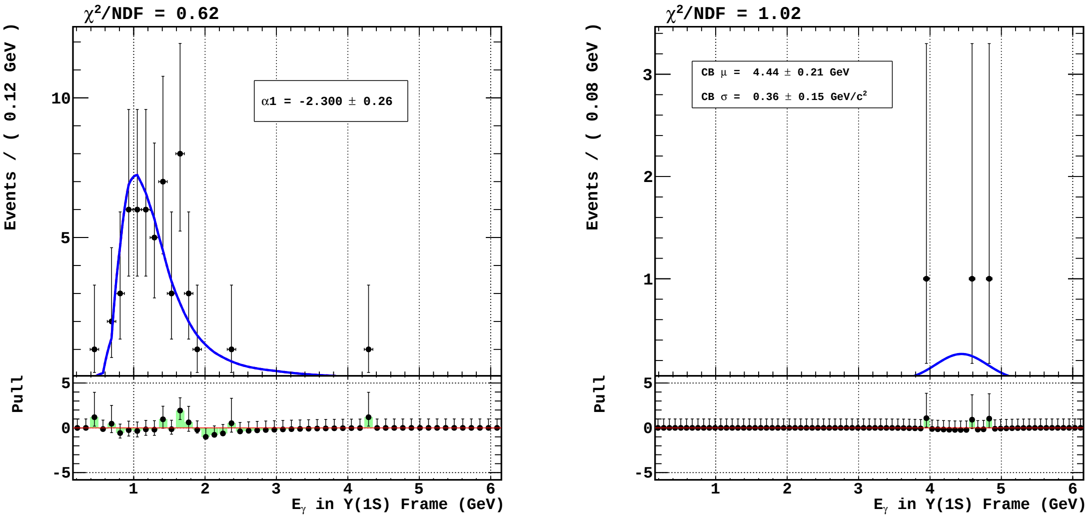

Figure 5.21.: Photon energy spectrum of background samples. Left: $\Upsilon(1S)$ leptonic decays, right: $\Upsilon(1S)$ hadronic decays.

PDF for leptonic decays

The photon energy spectrum of leptonic decays from the $\Upsilon(1S)$ is predominated by soft FSR photons and the beam backgrounds. This distribution in Figure 5.21 (left) is fitted with an exponential function as :

$$\mathcal{P}_{ll} \propto \epsilon_{\text{trig}}(E^*_\gamma) \times \exp\left(\alpha_1 \cdot E^*_\gamma\right) \tag{5.14}$$

PDF for hadronic decays

The contribution of hadronic decays from the $\Upsilon(1S)$ is much smaller than leptonic decays. However, they produce a peak at high energy region where the small contribution from the leptonic decays. We include this peak with a Gaussian function as

$$\mathcal{P}_{hh} \propto \mathcal{F}_{Gauss}(E^*_\gamma; \mu, \sigma) \tag{5.15}$$

Note that the ϵ_{trig} is not multiplied here. The fit result is shown in Figure 5.21 (right).

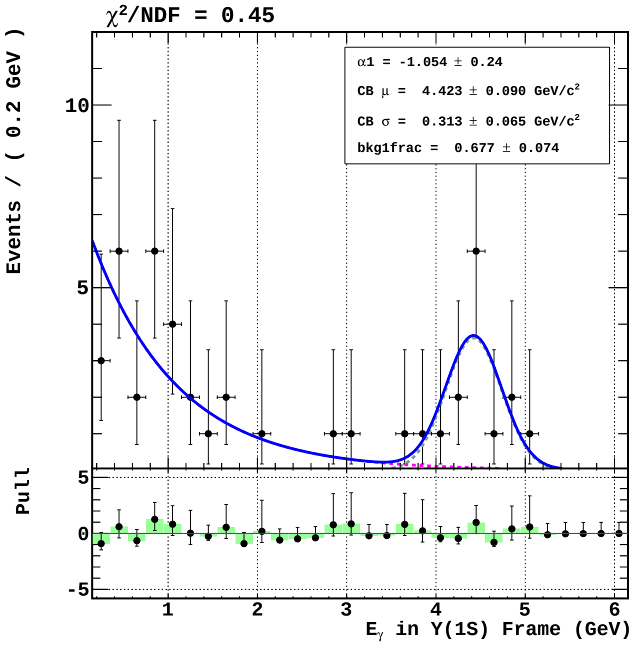

Figure 5.22.: Photon energy spectrum of continuum background.

PDF for continuum

The PDF for continuum events can accommodate other remaining backgrounds such that $\Upsilon(2S) \to \tau^+\tau^-$ and η' decays. The $\Upsilon(2S) \to \tau^+\tau^-$ events with a tau decaying to a π^0 and charged pions contribute to the overall photon energy spectrum and the η' contributes as a peaking background in the low energy region ($\approx$ 0.4 GeV). However, their contributions are not significant and distinguishable compared to the continuum events in that region. Thus, we treat the $\Upsilon(2S) \to \tau^+\tau^-$ and η' events to be a part of the continuum. The continuum is described with an exponential PDF plus a Gaussian PDF, it is defined as

$$\mathcal{P}_{off} \propto f_1 \cdot \exp\left(\alpha_1 \cdot E^*_\gamma\right) + (1-f_1) \cdot \mathcal{F}_{Gauss}(E^*_\gamma;\mu,\sigma) \quad . \tag{5.16}$$

The Gaussian function is used for ISR photons in the high energy region. The $\Upsilon(4S)$ off-resonance data is used to construct the continuum PDF. The $\epsilon_{\text{trig}}(E^*_\gamma)$ is not included in the PDF. The fit result is shown in Figure 5.22.

5.7. Determination of branching fractions

5.7.1. Yield Extraction

As shown in Table 5.2, the expected number of events is extremely small. Thus, we perform an unbinned extended log-likelihood fit at the given mass of the signal that maximizes the likelihood function

$$\mathcal{L} = \frac{\exp(-\sum_i n_i)}{N!} \prod_{j=1}^{N} \left(\sum_i n_i \mathcal{P}_i^j (M_{recoil}, E_\gamma^*) \right) \quad , \tag{5.17}$$

where n_i is the yield for each event type category for the signal and the backgrounds, N is the total observed number of events, j is the event index, and $\mathcal{P}_i^j$ is the PDF for each event type. We fix all shape parameters of PDFs and use the two-dimensional, (M_{recoil}, E_γ^*), space to constrain the yields from the different sources. Instead of floating three background yields, we combine the PDFs of the $\Upsilon(1S)$ backgrounds as follows:

$$\mathcal{P}_{\Upsilon(1S)} \propto f_{ll} \cdot \mathcal{P}_{ll} + (1 - f_{ll}) \cdot \mathcal{P}_{hh} \quad , \tag{5.18}$$

where f_{ll} is a fraction of events for the $\Upsilon(1S)$ leptonic decay ($\mathcal{P}_{ll}$). The f_{ll} is fixed with the expected value obtained from the $\Upsilon(2S)$ inclusive MC sample, $f_{ll} = 0.933 \pm 0.034$. Therefore, we float a total two background yields and one signal yield, N_{cont}, $N_{\Upsilon(1S)}$, and N_{sig}, to maximize the likelihood function.

5.7.2. Limit Calculation

We search for a signal over the range of $0 < M_{A^0} < 8.97$ GeV/c^2 and $0 < M_\chi < 4.44$ GeV/c^2. We perform the likelihood scan with the following procedure: first, we float the yields of the signal events (N_{sig}), the $\Upsilon(1S)$ background events ($N_{\Upsilon(1S)}$), and the continuum events (N_{cont}). We fix the f_{ll} with the value obtained from the MC and allow the negative yield for the signal and the backgrounds. We perform the extended log-likelihood fit for each M_{A^0} or M_χ by scanning for peaks in the E_γ^* distribution. For the on-shell signal events, we vary the photon energy with the step sizes from 25 MeV to 4.0 MeV which is equivalent with the half of photon energy resolution. Total 353 scan points are used. For the off-shell signal events, we use total 45 M_χ scan points with the fixed step size, 100 MeV. If the likelihood fit finds $N_{sig} > 0$, we compute the significance with $S = \sqrt{2\ln(\mathcal{L}_{max}/\mathcal{L}_0)}$, where -ln$\mathcal{L}_{max}$ is the negative log-likelihood value at the minimum and -ln$\mathcal{L}_0$ is the minimum value for the background only hypothesis. If no evidence is found, we compute the upper limits (90% C.L.) on the branching fractions for on-shell and off-shell signal with

$$\mathcal{B}(\Upsilon(1S) \to \gamma A^0, A^0 \to \chi\chi) = \frac{N^{upper}}{N_{\Upsilon(2S)} \times \mathcal{B}(\Upsilon(2S) \to \Upsilon(1S)\pi^+\pi^-) \times \epsilon} , \qquad (5.19)$$

where the N^{upper} is obtained by integrating the 90% of likelihood function as follows:

$$\int_0^{N^{upper}} \mathcal{L}(N_{sig})\, dN_{sig} = 0.9 \int_0^{\infty} \mathcal{L}(N_{sig})\, dN_{sig} \ . \qquad (5.20)$$

5.7.3. Results of the fits to MC

We mix the $\Upsilon(2S)$ inclusive MC events and $\Upsilon(4S)$ off-resonance experimental data with reduced sample sizes, called pseudo-experimental data, to mimic the real $\Upsilon(2S)$ on-resonance data. Figure 5.23 shows the results of the fit to the pseudo-experimental data without the signal PDF and Figure 5.24 shows an example of the result of likelihood and its integral as a function of the N_{sig}. Expected upper limits on branching fractions are obtained in Figure 5.25.

5.7.4. Fit to experimental data

Correction of PDF for continuum

We further check continuum backgrounds with the sideband regions in the $\Upsilon(2S)$ on-resonance data. The sidebands are defined as $9.415 < M_{recoil} < 9.44$ GeV/c^2 and $9.485 < M_{recoil} < 9.51$ GeV/c^2 shown in Figure 5.26 top. The high energy region in the photon energy spectrum shows a difference between the sidebands and the off-resonance data samples as shown in Figure 5.26 bottom. The difference in the shape of the broad bump in the high energy region could affect to estimate signal yields and could make a fake signal. Therefore, to apply the final fits to the $\Upsilon(2S)$ experimental data, we use new parameter values for the continuum background PDF obtained from the sideband regions.

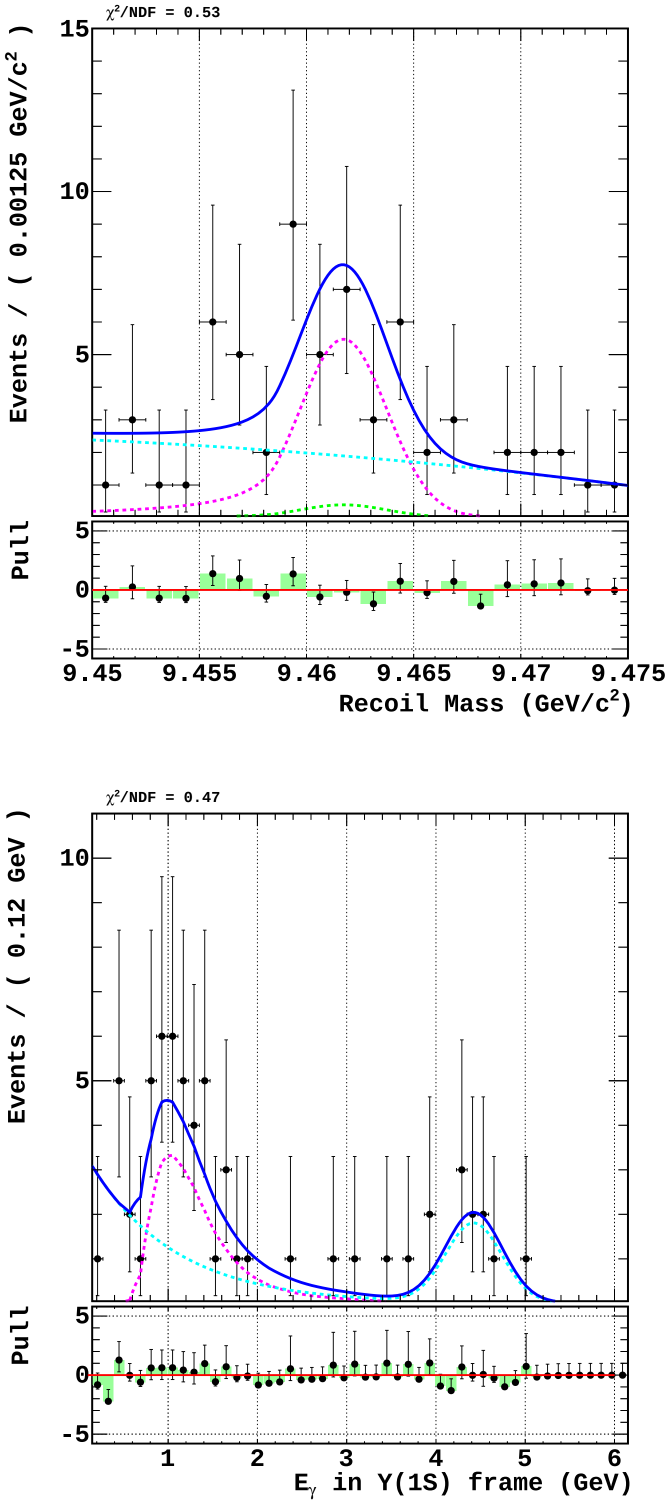

Figure 5.23.: The results of unbinned likelihood fit to the mixed events with the Υ(2S) inclusive MC events and Υ(4S) off-resonance experimental data. Top: the recoil mass distribution and bottom: the photon energy spectrum. Cyan dashed line is the continuum contribution, magenta dashed line is the leptonic decays, and green dashed line is the hadronic decays. Total PDF is shown as blue solid line.

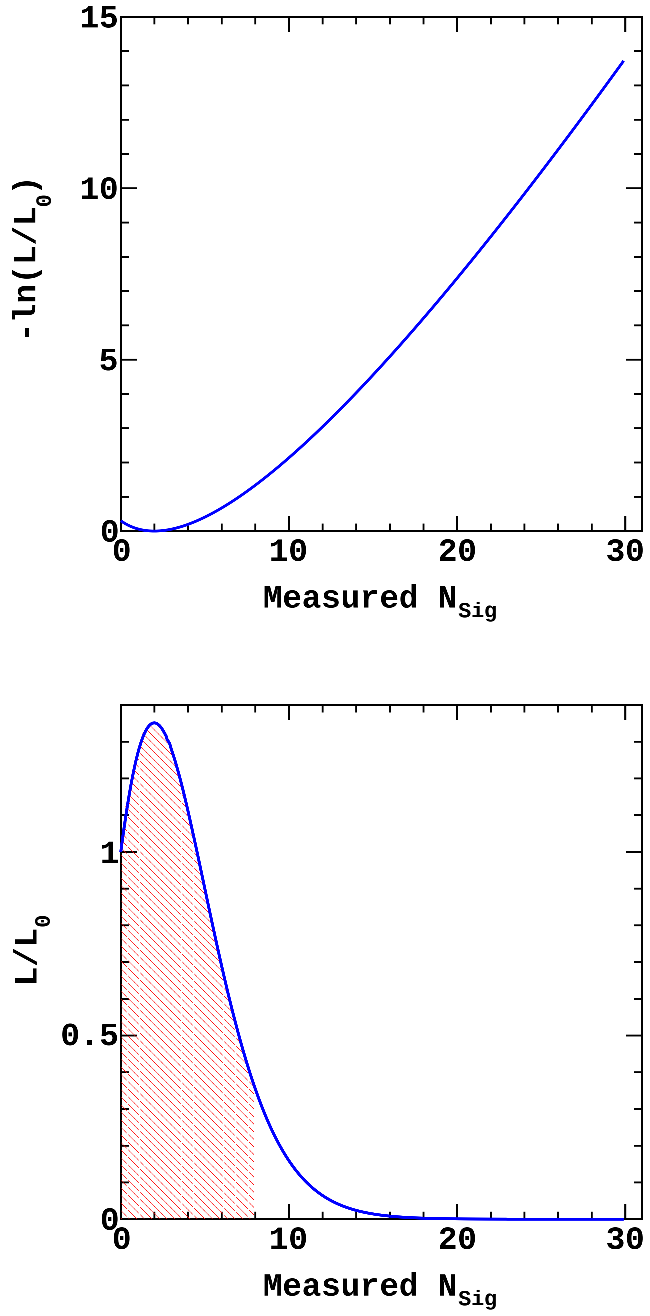

Figure 5.24.: An example of the result of likelihood as a function of signal yield at $M_{A^0} =$ 2.0 GeV ($E^*_\gamma \approx 4.5$ GeV).

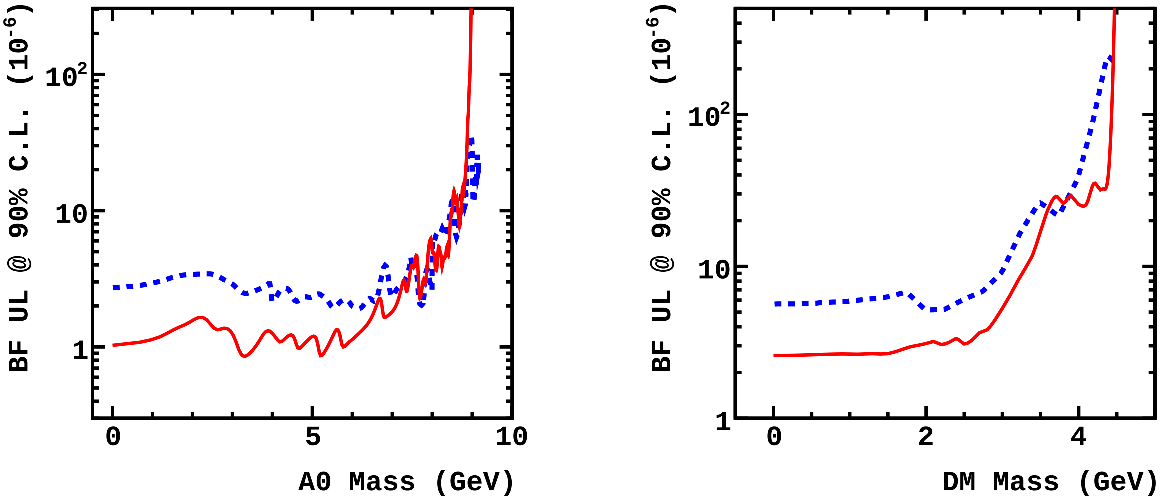

Figure 5.25.: Expected upper limits for the branching fraction at 90% C.L. (red solid line). Blue dashed lines show BaBar's limit [54]. Left: on-shell signal and right: off-shell signal.

Likelihood scan on the $\Upsilon(2S)$ data

Using the entire $\Upsilon(2S)$ data set, we perform the unbinned 2D likelihood fit to search for peaks as a function of M_{A^0} and M_χ in the photon energy spectrum. We observe the largest local significance as 2.078 σ (statistical uncertainty only) at M_{A^0}=2.946 GeV/c^2 and 2.067 σ (statistical uncertainty only) at M_{A^0}=8.487 GeV/c^2 which shown on Figure 5.27 and 5.28. We also perform the background only fit which results in $N_{\Upsilon(1S)} = 6.0 \pm 4.6$ and $N_{cont} = 60.9 \pm 8.7$.

We compared the experimental data with the pseudo-experimental data using all the triggers, shown in Figure 5.29 and 5.30. Pseudo-experimental data in the plots the are re-normalized with yields obtained from the background only fit to $\Upsilon(2S)$ experimental data.

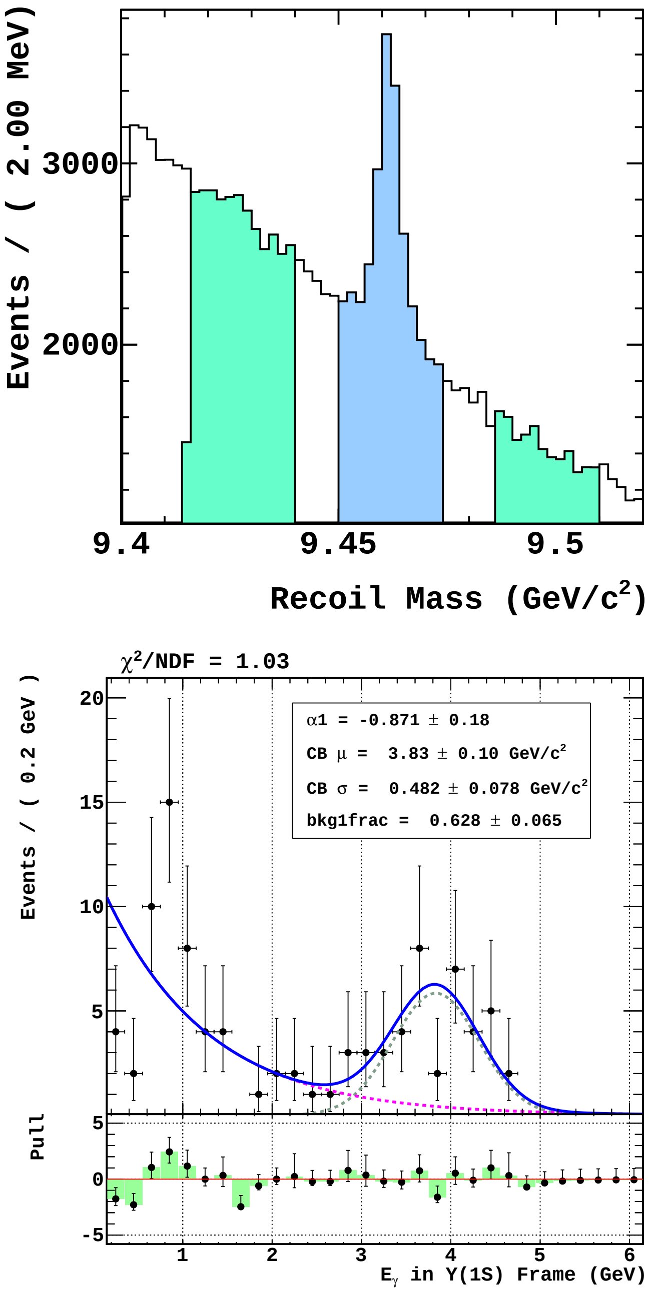

Figure 5.26.: Recoil mass distribution with a loose selection (top). The sideband regions are defined as $9.415 < M_{recoil} < 9.44$ GeV/c^2 and $9.485 < M_{recoil} < 9.51$ GeV/c^2 shown in green and the signal region is shown in blue. Photon energy spectrum of continuum background from the sideband regions (bottom).

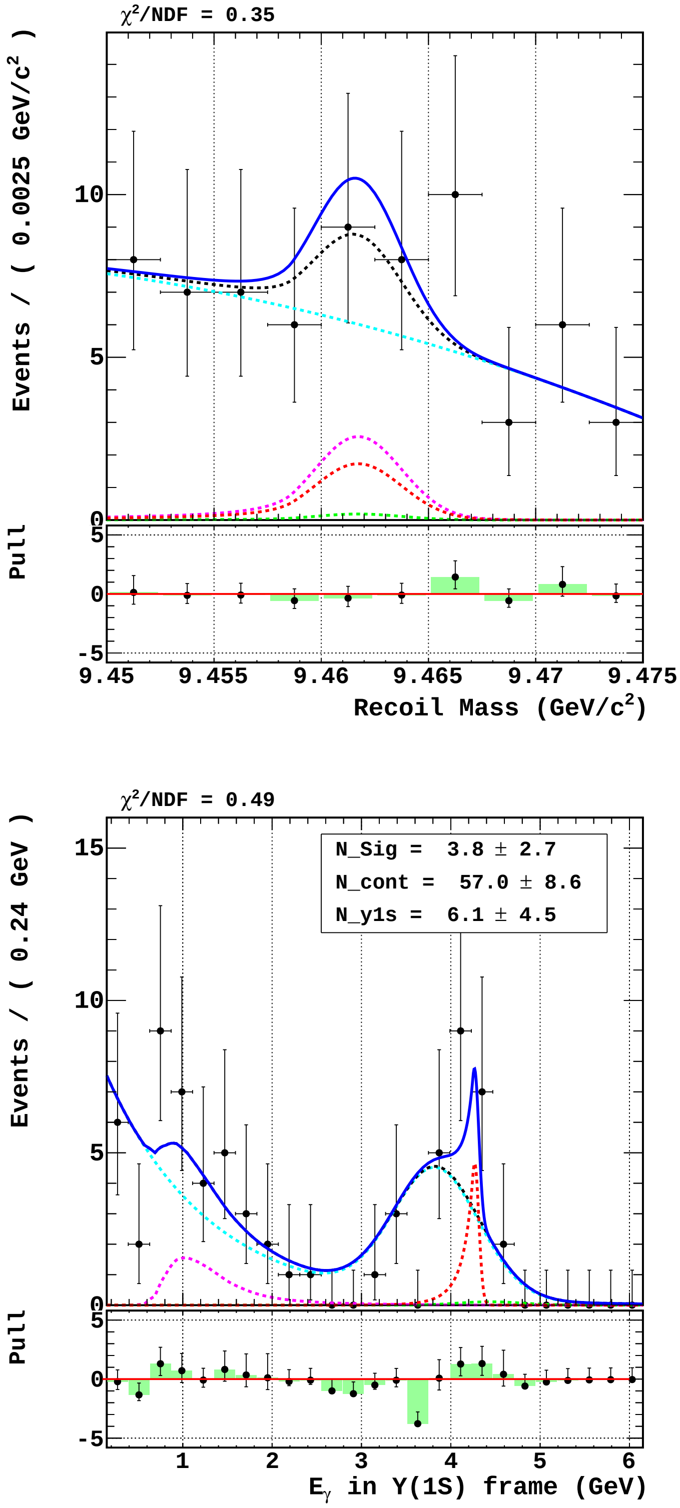

Figure 5.27.: An example of the fit results in the experimental data with M_{A^0}=2.946 GeV signal: M_{recoil} (top) and E^*_γ (bottom) distribution. The fitted lines are continuum backgrounds (cyan dashed line), $\Upsilon(1S)$ decay backgrounds (magenta dashed line), and the on-shell signal (red dashed line), which corresponds to the 2.078σ significance.

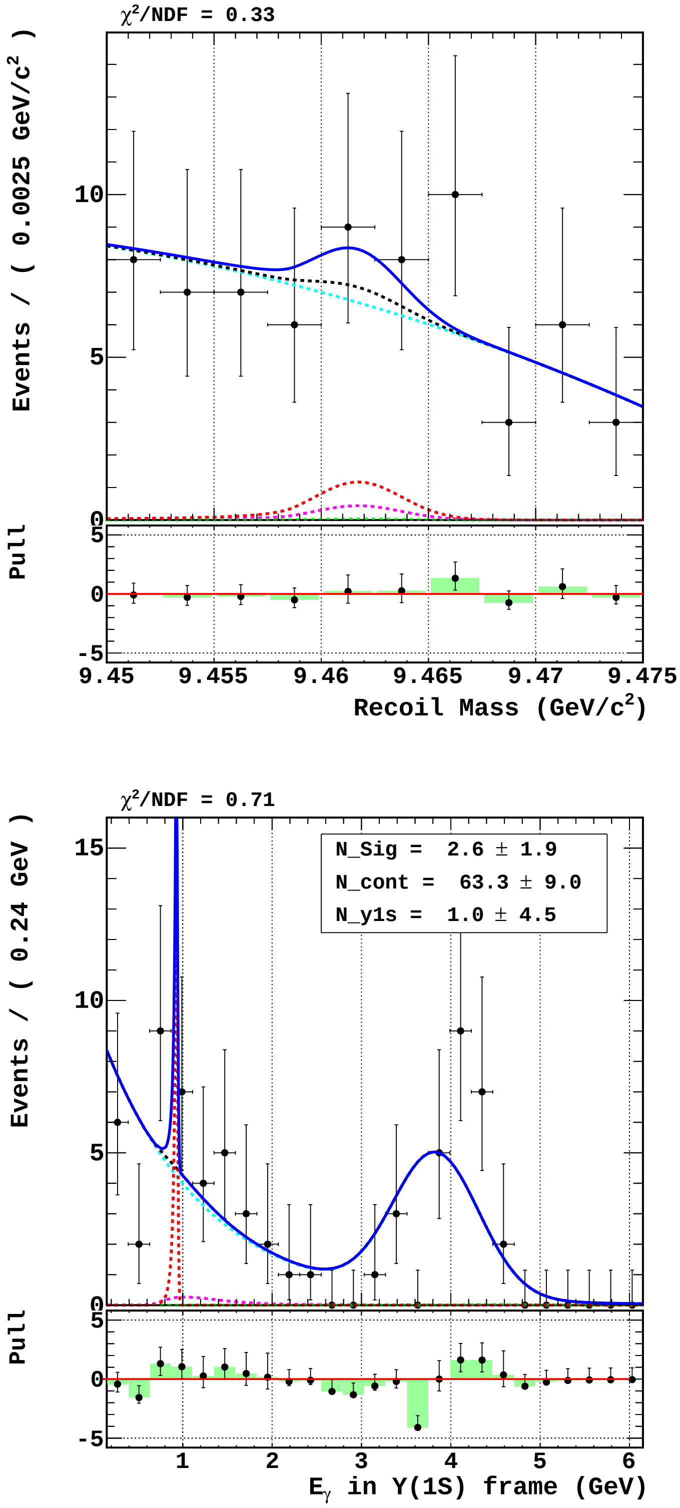

Figure 5.28.: An example of the fit results in the experimental data with M_{A^0}=8.487 GeV signal: M_{recoil} (top) and E^*_γ (bottom) distribution. The fitted lines are continuum backgrounds (cyan dashed line), $\Upsilon(1S)$ decay backgrounds (magenta dashed line), and the on-shell signal (red dashed line), which corresponds to the 2.067σ significance.

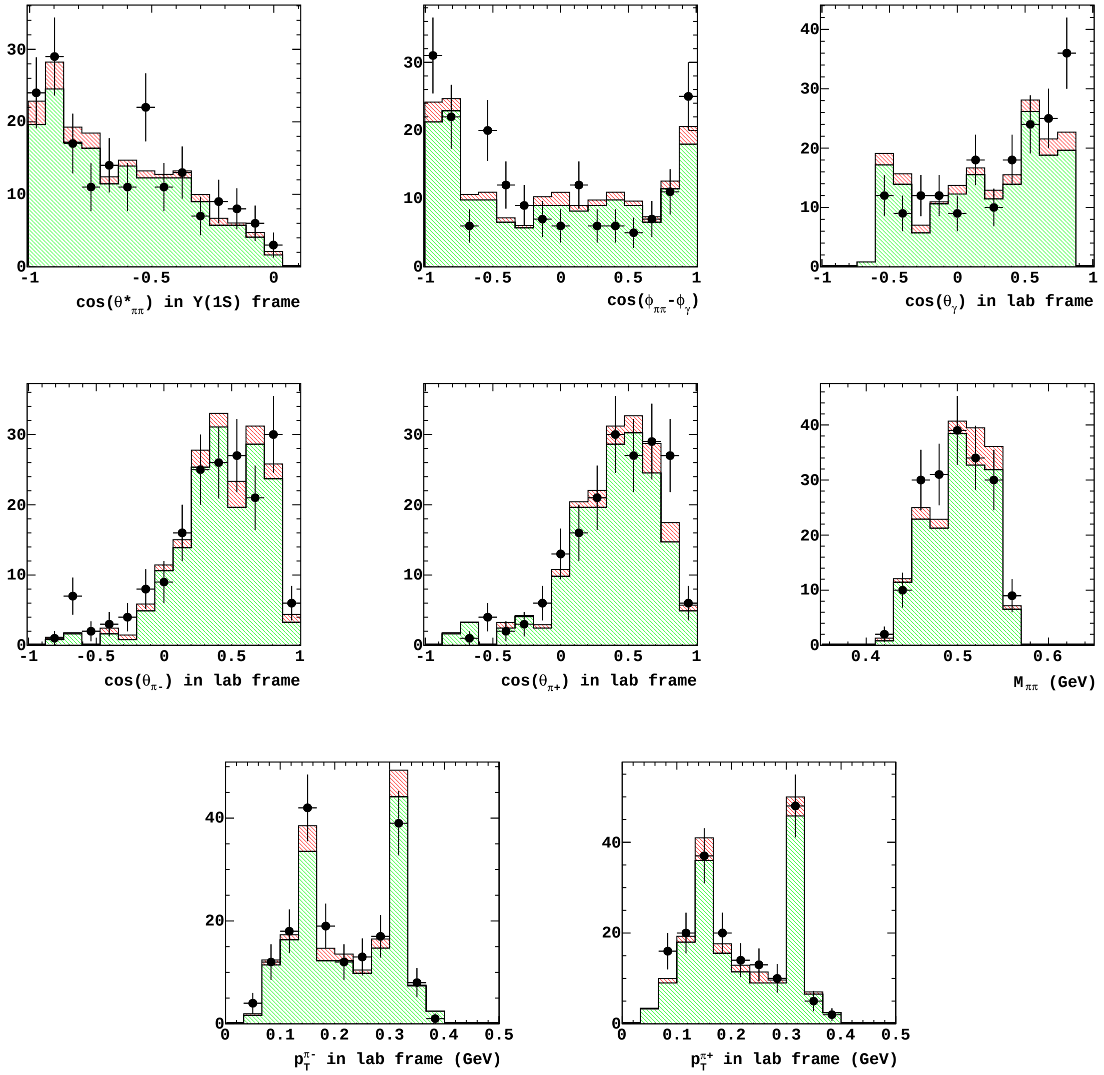

Figure 5.29.: Results of comparison between experimental and pseudo-experimental data with all triggers. Black dots are $\Upsilon(2S)$ on-resonance data and filed histograms are pseudo-experimental data, which is mixed with the $\Upsilon(4S)$ off-resonance (green) and $\Upsilon(2S)$ inclusive MC sample (red)

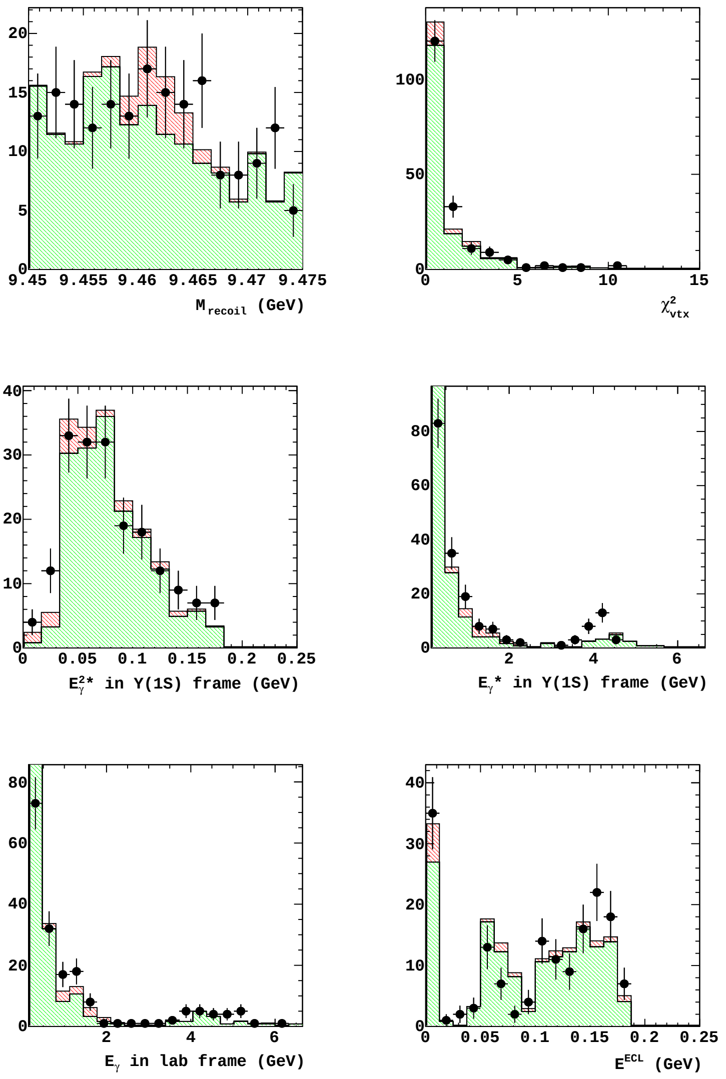

Figure 5.30.: Results of comparison between experimental and pseudo-experimental data with all triggers. Black dots are Υ(2S) on-resonance data and filed histograms are pseudo-experimental data, which is mixed with the Υ(4S) off-resonance (green) and Υ(2S) inclusive MC sample (red)

5.8. Systematic uncertainties

Most of observed N_{sig} is small, thus multiplicative uncertainties does not affect significantly. Main sources of systematic uncertainty arise from fit bias and PDF shape parameters. Systematic uncertainties are listed in order of least significant to most significant.

Branching fraction

The branching fraction of $\Upsilon(2S) \to \pi^+\pi^-\Upsilon(1S)$ is used to obtain the upper limits for the on-shell and off-shell signal. The systematic uncertainty due to the finite accuracy of the branching fraction is estimated to be 1.46% based on the PDG value.

Number of $\Upsilon(2S)$ events

The uncertainty of the number of the $\Upsilon(2S)$ events is 2.3% measured by the Belle collaboration [63].

Pion reconstruction

Systematic uncertainties of the reconstruction efficiency of pions are studied by the Belle collaboration [64, 65]. The uncertainties are estimated by comparing the efficiencies of MC and data. They report 1.4% and 0.35% systematic uncertainties per track in $P <$200 MeV/c and $P >$200 MeV/c, respectively. Instead of correcting the signal efficiency, we apply a systematic uncertainty of 1.4% per track.

Photon detection

Systematic uncertainties of photon detection are 2% in $3 > E_\gamma > 2$ GeV and 3% at $E_\gamma \approx 150$ MeV, reported by the Belle collaboration [?, 66]. Instead of applying different uncertainties depending on E_γ, we apply a systematic uncertainty of 3% in the entire E_γ region.

Signal MC Statistics

Systematic uncertainties of signal statistics are varying from 0.2% to 0.7% at $\leq$ 8.5 GeV/c^2 A^0 and from 0.7% to 30% at 8.5 GeV/c^2 $< M_{A^0} <$ 9.0 GeV/c^2 for the on-shell signal; and from 0.3% to 0.8% at $\leq$ 4.0 GeV/c^2 χ and from 0.8% to 38% at 4.0 GeV $< M_\chi <$ 4.5 GeV/c^2 for the off-shell signal.

Trigger efficiency

The systematic uncertainty due to the triggers is taken to be the difference in means of the e_had relative efficiency. The means of e_had relative efficiency of the data and MC samples are obtained at the $E^{trg}_{ECL} >$ 3.5 GeV range, and it results in 13.5% error. We also investigate the difference in the signal efficiency due to the beam background contribution in TSIM. We observe the variation of 0.001 % - 8.1% from excluding the highest signal mass region, which retains less than 10 events in any cases. Therefore, we assign 13.5% as the systematic uncertainty for the trigger efficiency.

Fit bias

A possible bias in the fit is checked with toy MC samples. Fit bias is tested for the same masses used to generate the signal MC samples. For each signal mass, a toy MC is generated using the background and signal PDFs. The number of backgrounds to generate a toy MC is obtained from the background-only fit to the $\Upsilon(2S)$ experimental data, and the signal yields are varied from 0 to 11. 1000 toy MC samples are generated for each signal mass and each yield.

Each toy MC sample is fitted with the likelihood function and N_{sig} distribution is obtained for each signal yield and each mass. In the photon energy spectrum, there are regions having zero events, where the fits are only constrained by the total number of events. These ranges make large negative yields, especially for the on-shell signal process, due to the narrow shape of PDF. Thus, the N_{sig} distributions are fitted with a Gaussian function by neglecting the tail of distribution; and the results are used to test a linearity of the signal yields for each mass. The results of the tests for $M_{A^0} = 0.1$ and 9.0 GeV are shown in Figure 5.31 with a constant fit function. Other results are shown in Figure D.1 and Figure D.2.

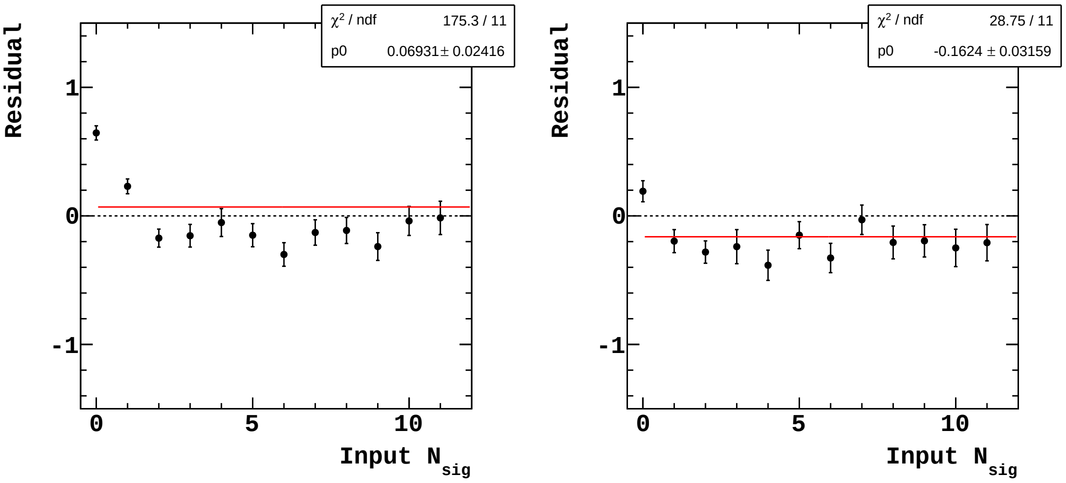

Figure 5.31.: Measured N_{sig} from toy MC as a function of input N_{sig}. Black dashed line shows the expected value and red solid line is the linear fit result. Left: for M_{A^0} = 0.1 and right: 9.0 GeV.

The constant fitting results for each mass are used to determine the average fit bias shown in Figure 5.32. We observe the fit bias of 0.001 in the on-shell signal and observe the bias with the M_χ dependency in the off-shell signal. The large fit bias in the off-shell process occurs around $M_\chi = 3.5$ GeV, which corresponds to the photon energy $1 < E^*_\gamma < 2$ GeV. In this range, the leptonic decay background influences the measured signal yield. Therefore, we generate more mass samples around the mass with the largest bias to extract the fit bias as a function of M_χ. This fit bias is used as systematic uncertainties instead of corrections.

PDF shape parameters

Systematic uncertainties of PDF shapes are estimated by varying 22 shape parameters with $\pm 1\sigma$, which corresponding to their uncertainty. The shape parameters of continuum background are the main source of uncertainty. The signal yields extracted with a negative value are considered to zero when estimating variations. We add every variation of a signal yield at each signal mass in quadrature and select the largest ΔN_{sig} in the entire mass range as a systematic uncertainty to get the most conservative limit. We estimate the systematic uncertainties due to the PDF shapes as $\Delta N_{sig} = 2.5$ and $\Delta N_{sig} = 2.8$ for the on-shell and off-shell signal, respectively.

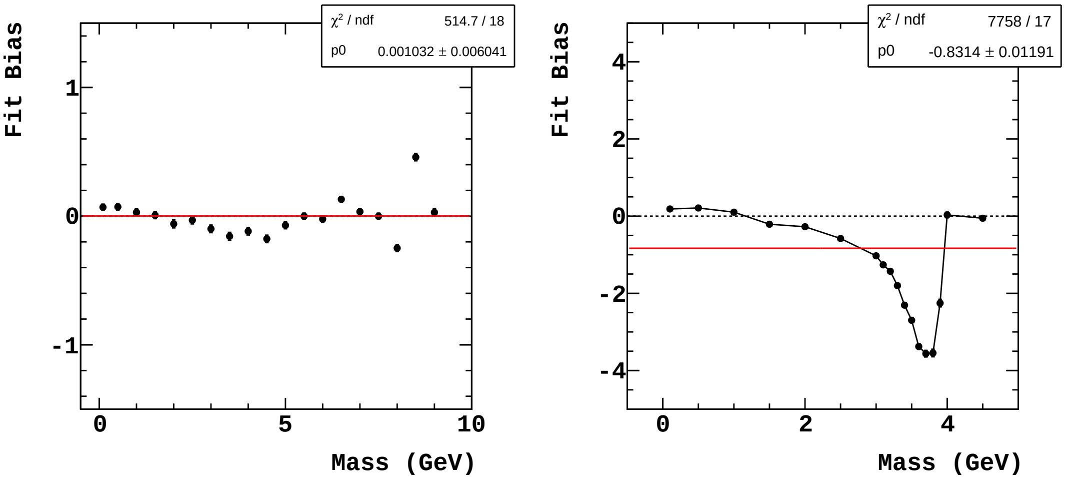

Figure 5.32.: Average fit bias for the on-shell signal (top) and the off-shell (bottom).

The total systematic uncertainty is obtained by the quadratic sum of the additive and multiplicative errors. The total systematic uncertainty, σ_{syst}, is included to the likelihood function by convolving with a Gaussian which has the width of the σ_{syst}:

$$\mathcal{L}(N_{sig}) = \int \mathcal{L}(N'_{sig}) \frac{\exp\left(-\frac{(N'_{sig}-N_{sig})^2}{2\sigma_{syst}^2}\right)}{\sqrt{2\pi\sigma_{syst}^2}}\, dN'_{sig} \quad . \tag{5.21}$$

Chapter 6

Conclusion and implication

6.1. Upper limits on branching fractions

90% C.L. upper limits on the BFs for $\Upsilon(1S) \to \gamma A^0, A^0 \to \chi^0\chi^0$ and $\Upsilon(1S) \to \gamma\chi^0\chi^0$ are measured in the mass range of $M_{A^0} < 8.97$ GeV/c^2 and $M_\chi < 4.44$ GeV/c^2 using 157.3×10^6 $\Upsilon(2S)$ decays at Belle. The results are shown in Figure 6.2. The solid orange and dash-dotted purple lines are the Belle limits with and without including the systematic uncertainty, respectively. Blue dashed lines are the BaBar results, which used 98×10^6 $\Upsilon(2S)$ decays [54]. In the result of the on-shell, the Belle result is similar or worse sensitivity compared the BaBar's result, this is due to the worse signal efficiency than the BaBar experiment.

6.2. WIMP-nucleon cross section limit

The limit on the branching fraction of the off-shell process can be converted into a WIMP-nucleon cross section limit by using the procedure in [34]. Using the contact operator approximation, the limit on the off-shell process is translated into a WIMP-nucleon scattering limit, which is a complementary to the results of WIMP direct detection experiments. Our off-shell signal samples are generated with the PHSP model. This corresponds to the S1 operator in [34], and given by

$$\frac{m_q}{\Lambda^2}\,\phi^\dagger\,\phi\,\bar{q}\,q\,, \qquad (6.1)$$

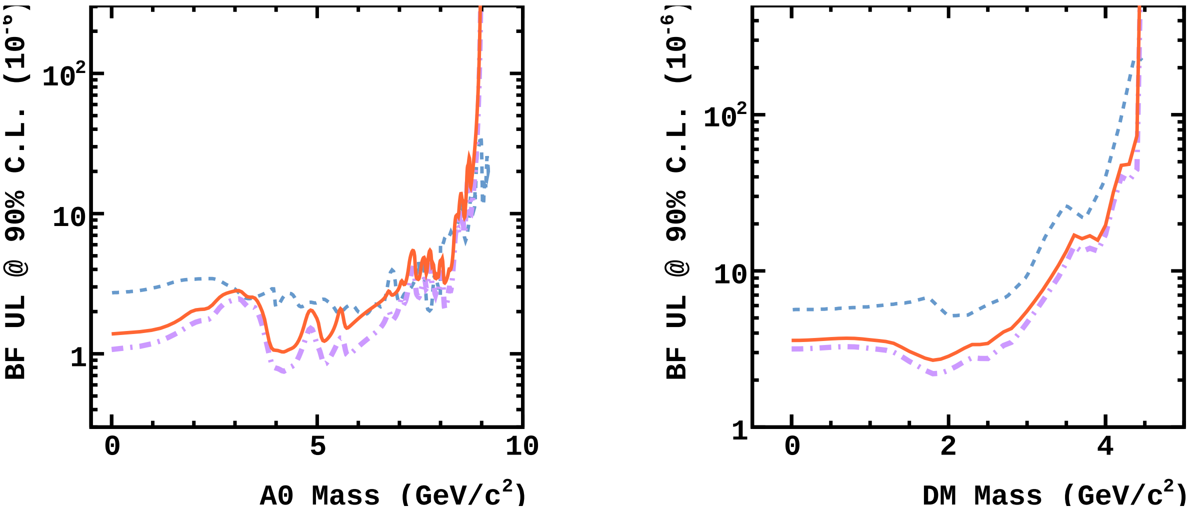

Figure 6.1.: 90% C.L. upper limits on the BFs for $\Upsilon(1S) \to \gamma A^0, A^0 \to \chi^0\chi^0$ (left) and $\Upsilon(1S) \to \gamma\chi^0\chi^0$ process (right). Blue dashed lines are the results of Babar and orange solid lines and dash-dotted purple lines are the Belle limits with and without including the systematic uncertainty.

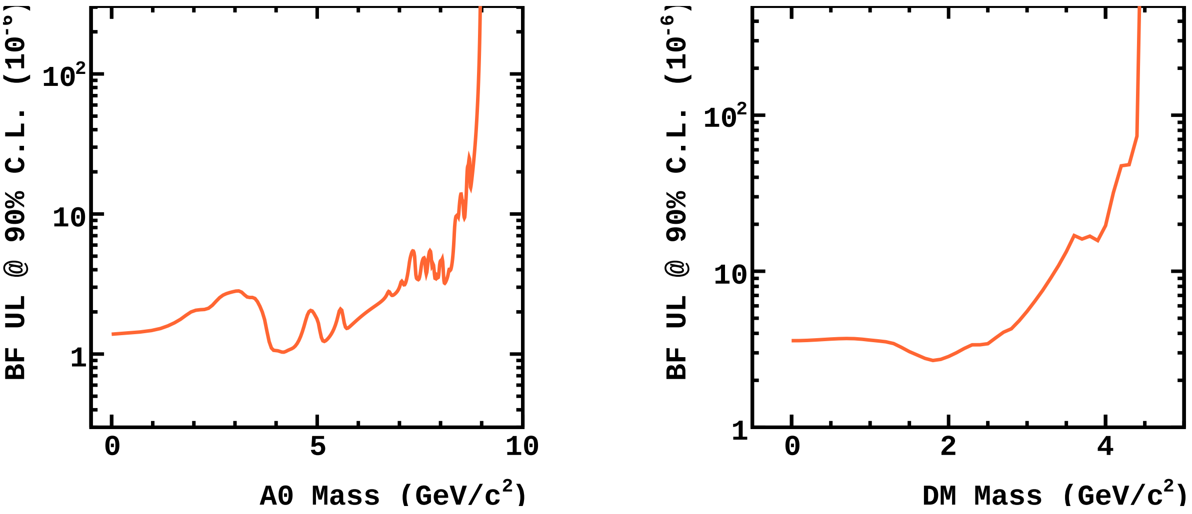

Figure 6.2.: Belle 90% C.L. upper limits on the BFs for $\Upsilon(1S) \to \gamma A^0, A^0 \to \chi^0\chi^0$ (left) and $\Upsilon(1S) \to \gamma\chi^0\chi^0$ process (right).

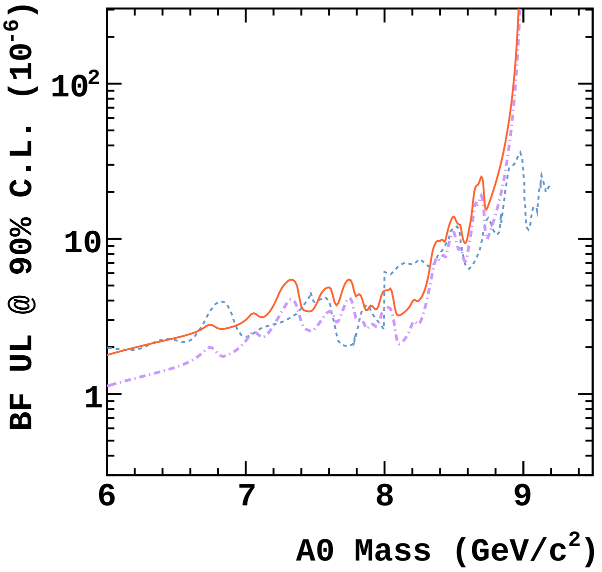

Figure 6.3.: Zoomed plot of the 90% C.L. upper limit on the BF for $\Upsilon(1S) \rightarrow \gamma A^0, A^0 \rightarrow \chi^0\chi^0$ in the M_{A^0} region of 6 - 9.5 GeV. Blue dashed lines are the results of Babar and orange solid lines and dash-dotted purple lines are the Belle limits with and without including the systematic uncertainty.

where m_q is the mass of quarks, Λ is the mediator scale, ϕ is the scalar DM field, and q is the quark field. The relevant branching fraction is given as

$$\mathcal{B}_{S1}(\Upsilon(1S) \rightarrow \gamma\chi\bar{\chi}) = \frac{\mathcal{B}(e^+e^-)M^2_{\Upsilon(1S)}M^2_{\chi}}{32\pi^3\alpha\Lambda^4}\left[I^0_{1/2} - 4\frac{M^2_{\chi}}{M^2_{\Upsilon(1S)}}I^1_{1/2}\right], \quad (6.2)$$

where $M_{\Upsilon(1S)}$ is the mass of $\Upsilon(1S)$, and $\alpha = 1/137$ is the fine-structure constant. I^m_n is defined as

$$I^m_n(x) = \int_1^x \left(1 - \frac{1}{x'}\right)^n x'^{\,m} dx', \quad (6.3)$$

where $x \simeq M^2_{\Upsilon(1S)}/4m^2_{\chi}$. From equation 6.2, we can obtain a lower limit on Λ with respect to M_{χ} and the result is shown in Figure 6.4. The contact operator approximation is only valid for a mediator mass larger than the momentum transfer in the given system. The mediator mass can be expressed by $M_{med} \sim g\,\Lambda$, where g is a coupling constant for the given interaction, thus if we assume g is of the order of 1, the limit on Λ would valid for all WIMP masses.

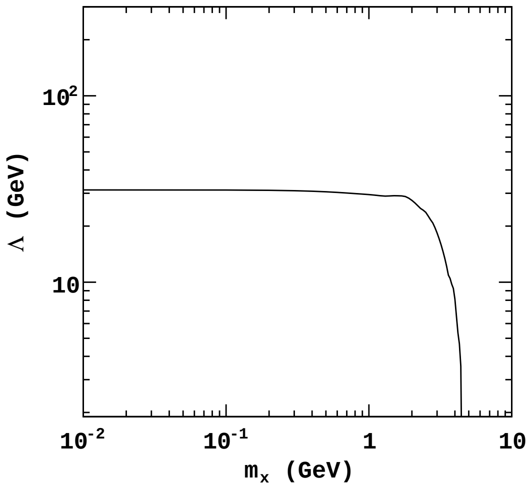

Figure 6.4.: Lower limit on the mediator scale Λ as a function WIMP mass M_χ.

Based on the estimated Λ, the WIMP-nucleon cross section can be obtained by:

$$\sigma_{SI}^{S1} = \frac{\mu_p^2 m_p^2}{4\pi\Lambda^4 M_\chi^2}\left(\sum_{q=u,d,s} f_q^p + \frac{2}{27}\sum_{c,b,t} f_g^p\right)^2, \tag{6.4}$$

where m_p is the proton mass, μ_p is the reduced mass of the dark matter and proton system. The nucleon form factors are assumed as $f_u^p = f_d^n = 0.024$, $f_d^p = f_u^n = 0.035$, $f_s^{p,n} = 0.051$, and $f_g^{p,n} = 1 - \sum_{q=u,d,s} f_q^{p,n}$ based on [67]. The exclusion limit on the WIMP-nucleon cross-section for this analysis is obtained and the result is shown in Figure 6.5. The black solid and dashed lines are the 90% C.L. limits by assuming interactions with all quarks and only b quarks, respectively. The Belle result with current data is not comparable with results of direct detection experiment. However, we uniquely constrain low mass dark matter region where direct detection experiments can not. In future experiment, such as the Belle II experiment, we can searches for a a signal with various contact operators discussed in [34] and can provide competitive limits on WIMP-nucelon scattering cross sections as shown in Figure 6.6 and 6.7

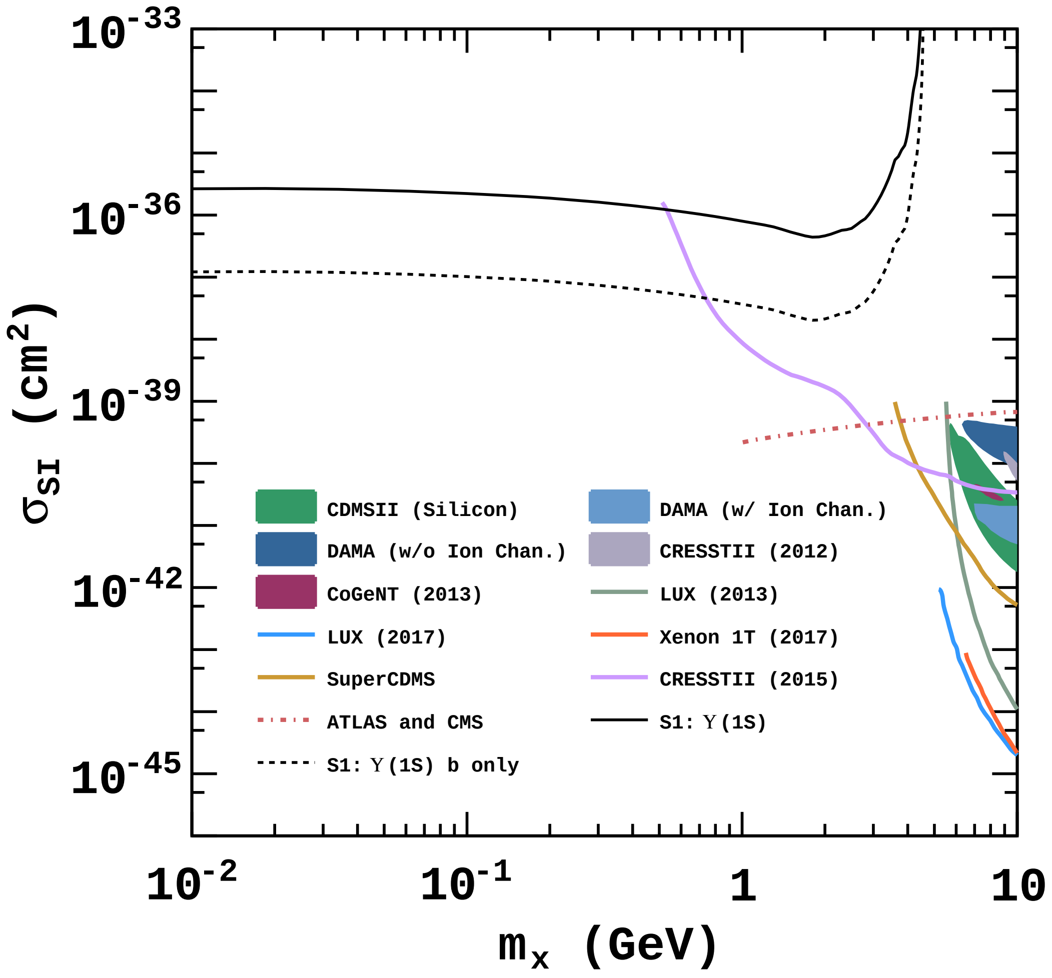

Figure 6.5.: WIMP-nucleon spin-independent scattering cross-section limit at 90% C.L. The black solid and dashed lines are the exclusion limits by assuming the coupling to all quarks and only b-quarks, respectively. The 90% C.L. exclusion limits of LUX [68], CRESST II [69], SuperCDMS [70], and ATLAS [29,30] and CMS [31, 32] are shown for reference; and the 90% C.L. signal regions of CRESST II [22], CoGeNT [71], DAMA/LIBRA [72], and CDMS II (Silicon) [23] are also shown.

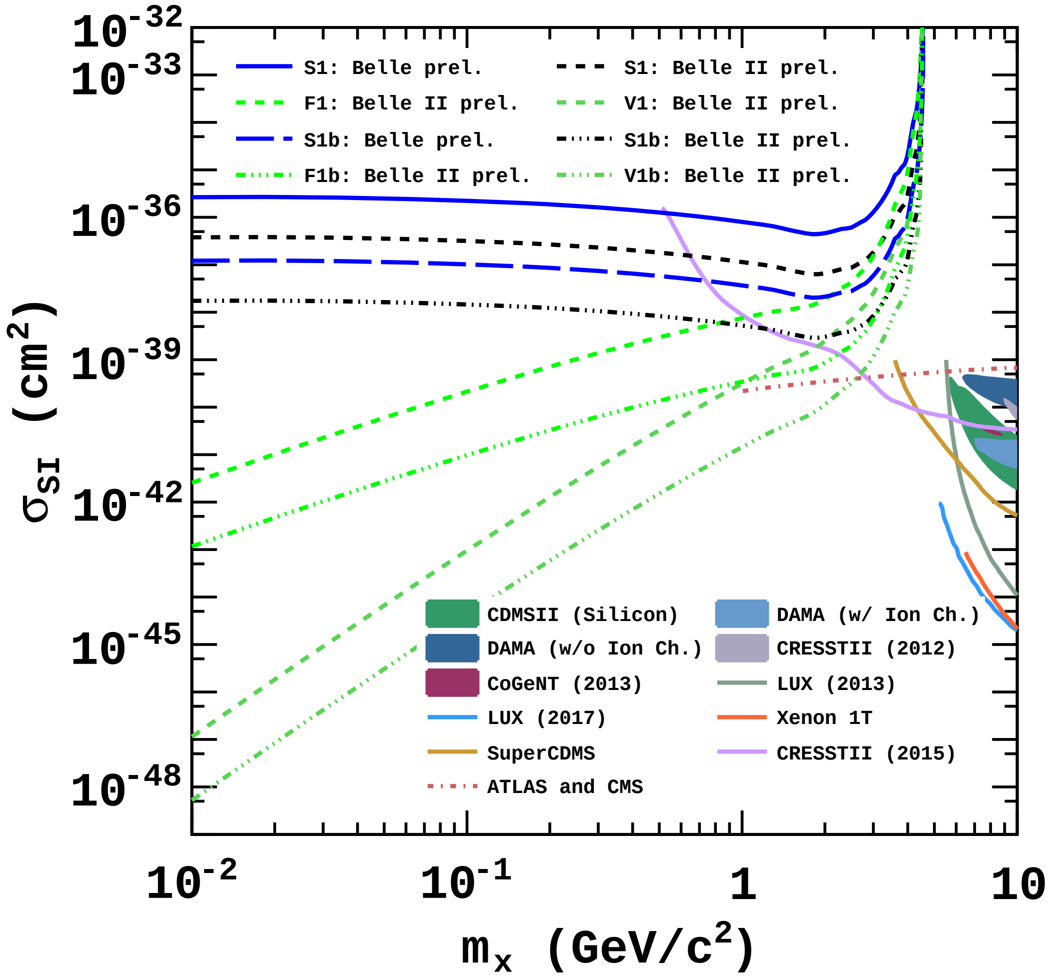

Figure 6.6.: Belle II prospects for WIMP-nucleon spin-independent scattering cross-section limit at 90% C.L. The blue solid and dashed lines are the Belle limits by assuming the coupling to all quarks and only b-quarks, respectively. Black, light-green, and green short-dashed and dash-dotted lines are Belle II prospects with various contact operators.

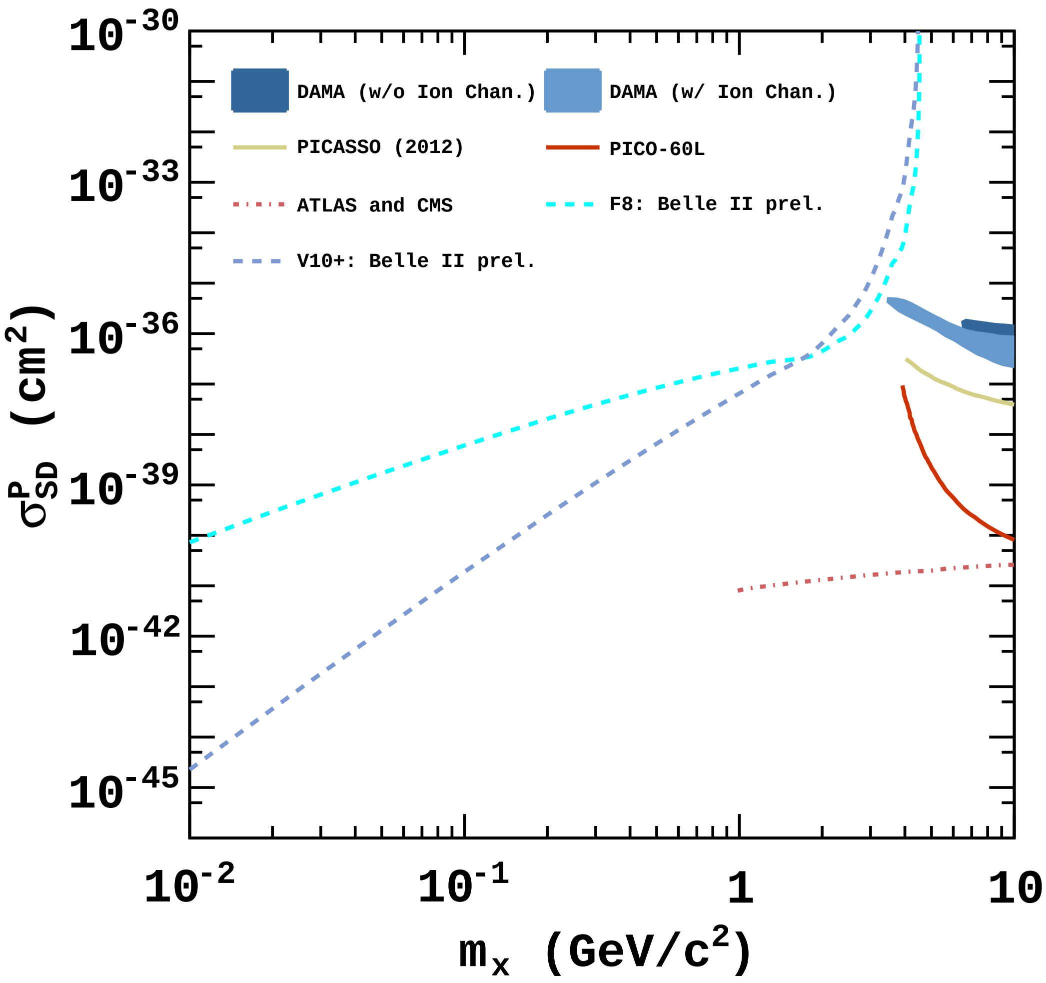

Figure 6.7.: Belle II prospects for WIMP-nucleon spin-dependent scattering cross-section limit at 90% C.L. The cyan and sky-blue dashed lines are Belle II prospect limits. The exclusion limits of PICO-60L [26], PICASSO [73], and ATLAS [29,30] and CMS [31,32] are shown; and signal region of DAMA/LIBRA [72] is also shown.

Appendix A

Decay table for the $\Upsilon(2S)$ inclusive MC sample

This decay table is used to generate the $\Upsilon(2S)$ inclusive MC samples.

```
Decay Upsilon(2S)
0.019100000 e+      e-                     PHOTOS  VLL;
0.019300000 mu+     mu-                    PHOTOS  VLL;
0.020000000 tau+    tau-                   VLL;
0.181000000 Upsilon pi+     pi-            VVPIPI;
0.086000000 Upsilon pi0     pi0            VVPIPI;
0.038000000 gamma   chi_b0                 HELAMP 1. 0. +1. 0.;
0.069000000 gamma   chi_b1                 HELAMP 1. 0. 1. 0. -1. 0. -1. 0.;
0.071500000 gamma   chi_b2                 HELAMP 2.4494897 0. 1.7320508 0.
                                     1. 0. 1. 0. 1.7320508 0. 2.4494897 0.;
0.00500         d       anti-d             PYTHIA          32;
0.02000         u       anti-u             PYTHIA          32;
0.00500         s       anti-s             PYTHIA          32;
0.02000         c       anti-c             PYTHIA          32;
0.42160         g       g       g          PYTHIA          4;
0.01600         gamma   g       g          PYTHIA          4;
0.000210000 Upsilon eta                    PHSP;
0.000390000 gamma   eta_b                  PHSP;
Enddecay

Decay Upsilon
0.024800000 e+      e-                     PHOTOS  VLL;
0.024800000 mu+     mu-                    PHOTOS  VLL;
0.026000000 tau+    tau-                   VLL;
0.014959973 d       anti-d                 PYTHIA          32;
```

```
0.044879919 u        anti-u                     PYTHIA            32;
0.014959973 s        anti-s                     PYTHIA            32;
0.044879919 c        anti-c                     PYTHIA            32;
0.774328202 g        g        g                 PYTHIA            4;
0.028922614 gamma    g        g                 PYTHIA            4;
0.000063000 gamma    pi+      pi-               PHSP;
0.000017000 gamma    pi0      pi0               PHSP;
0.000011400 gamma    K+       K-                PHSP;
0.000290000 gamma    pi+      pi-      K+       K-                         PHSP;
0.000250000 gamma    pi+      pi+      pi-      pi-                        PHSP;
0.000250000 gamma    pi+      pi+      pi+      pi-      pi-      pi-      PHSP;
0.000240000 gamma    pi+      pi+      pi-      pi-      K+       K-       PHSP;
0.000150000 gamma    pi+      pi-      p+       anti-p-                    PHSP;
0.000040000 gamma    pi+      pi+      pi-      pi-      p+       anti-p-  PHSP;
0.000020000 gamma    K+       K+       K-       K-                         PHSP;
0.000037000 gamma    f'_2                       PHSP;
0.000101000 gamma    f_2                        PHSP;
Enddecay
```

Appendix B

Figure of merits for the selection

The results of FOMs are present here. To optimize selection, we used all triggers to increase statistics. Figure B.1 is FOMs for $M_{A^0} = 0.1$ GeV/c^2 and Figure B.2 is FOMs for $M_{A^0} = 9.2$ GeV/c^2.

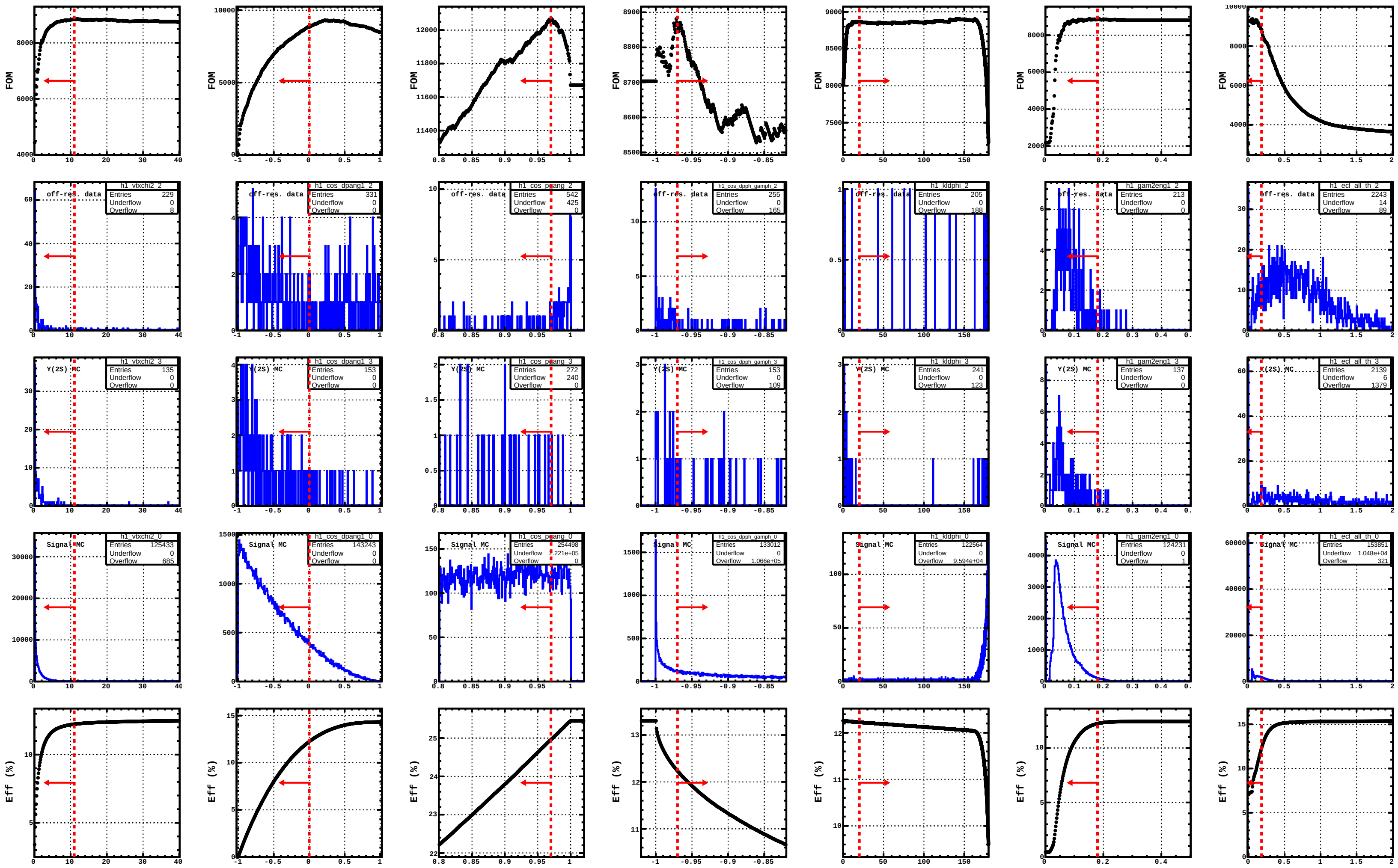

(a) χ^2_{vtx} (b) $cos(\theta^*_{\pi\pi})$ (c) $cos(\theta_{\pi^\pm\gamma})$ (d) $cos(\phi_{\pi\pi} - \phi_\gamma)$ (e) $|\Delta\phi_{\gamma N}|$ (f) E^{2*}_γ (g) E^{remains}_{ECL}

Figure B.1.: Figure of Merit and efficiency with N-1 calculation for $M_{A^0} = 0.1$ GeV/c^2. The rows are listed as follows: the FOM, Υ(4S) off-resonance data, the Υ(2S) inclusive MC sample, the signal sample, and the efficiency of the signal sample.

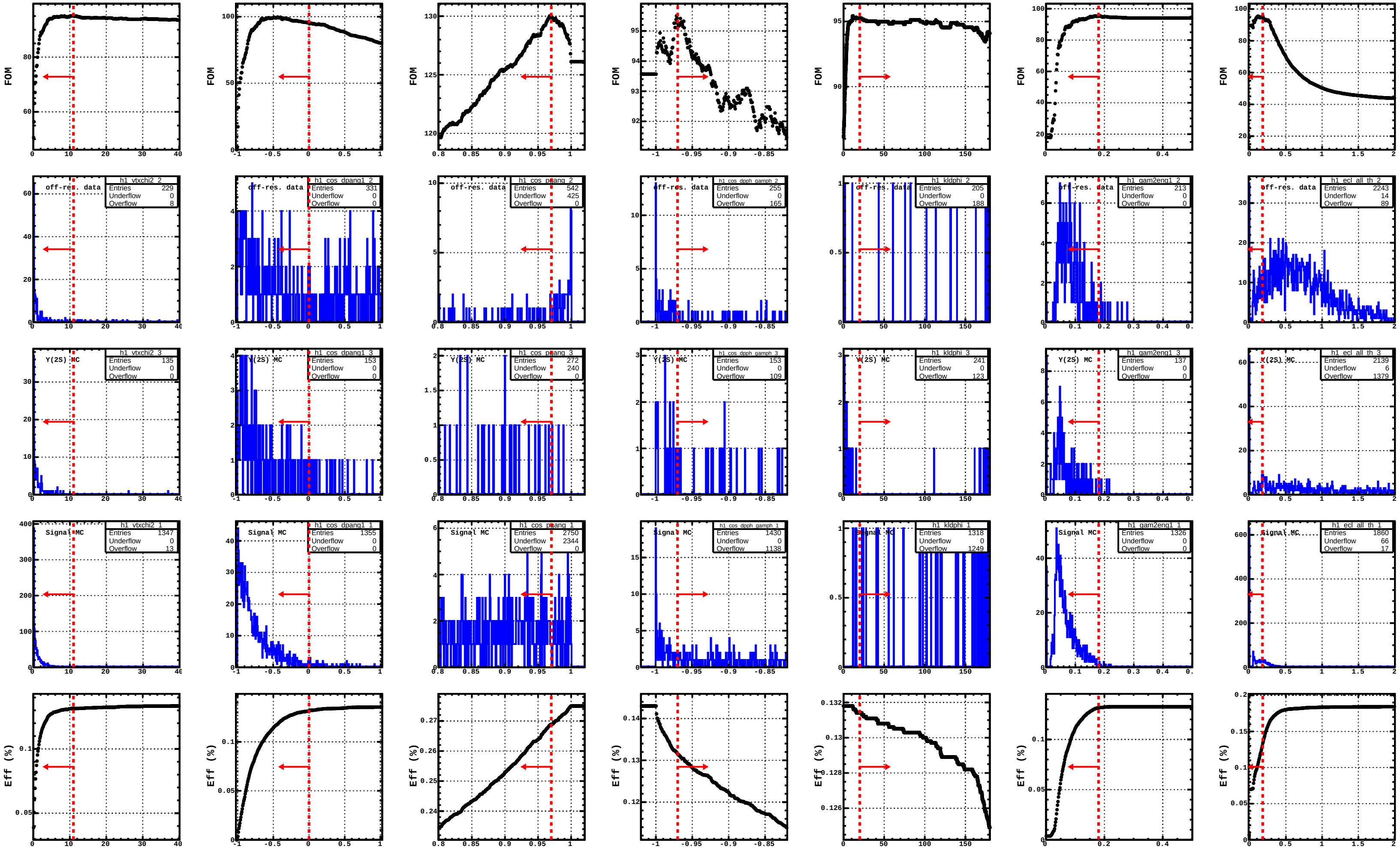

(a) χ^2_{vtx} (b) $cos(\theta^*_{\pi\pi})$ (c) $cos(\theta_{\pi^\pm\gamma})$ (d) $cos(\phi_{\pi\pi}-\phi_\gamma)$ (e) $|\Delta\phi_{\gamma N}|$ (f) E^{2*}_γ (g) $E^{\mathrm{remains}}_{ECL}$

Figure B.2.: Figure of Merit and efficiency with N-1 calculation for $M_{A^0} = 9.2$ GeV/c^2. The rows are listed as follows: the FOM, Υ(4S) off-resonance data, the Υ(2S) inclusive MC sample, the signal sample, and the efficiency of the signal sample.

Appendix C

Photon energy spectrum for the signal MC samples

The signal photon energy spectrum with its PDF is present here.

C.1. On-shell signal sample

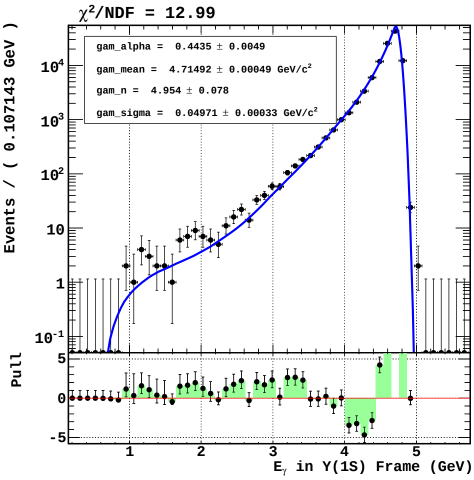

(a) M_{A^0} = 0.5 GeV/c^2

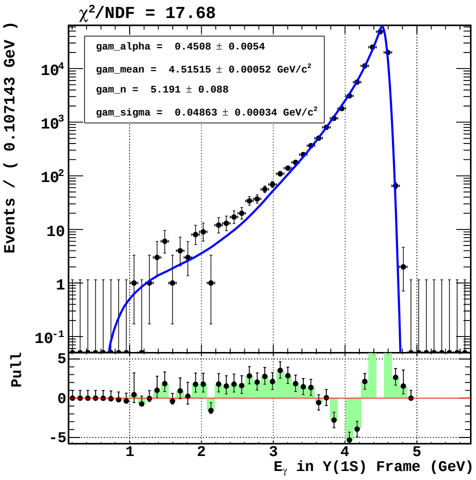

(b) M_{A^0} = 2.0 GeV/c^2

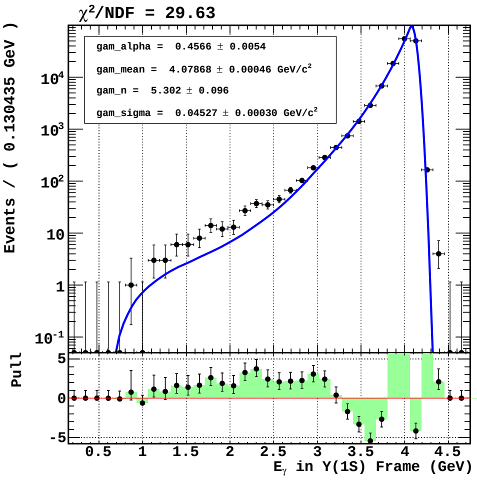

(c) M_{A^0} = 3.5 GeV/c^2

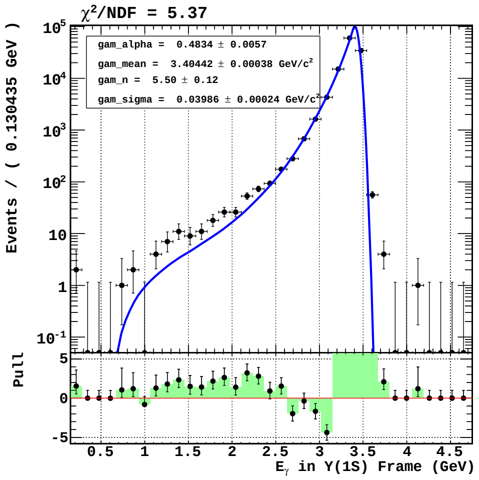

(d) M_{A^0} = 5.0 GeV/c^2

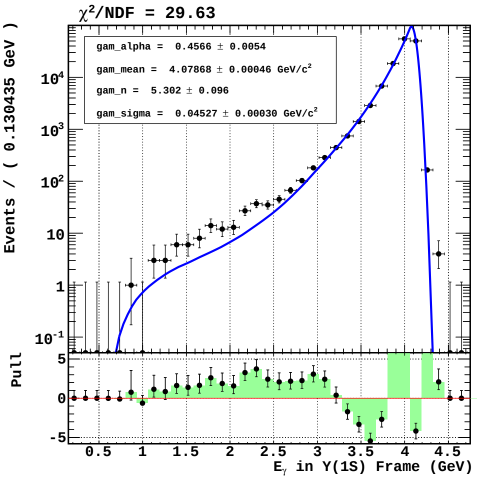

(e) M_{A^0} = 3.5 GeV/c^2

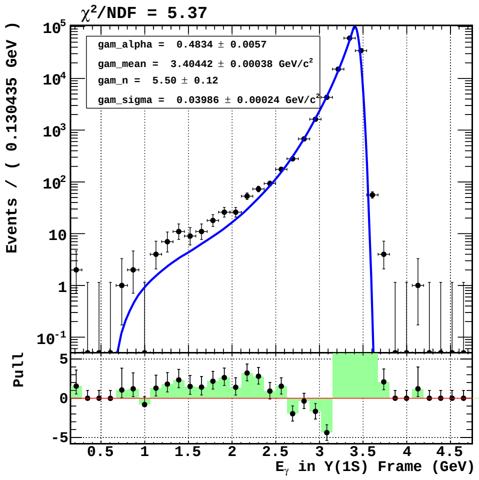

(f) M_{A^0} = 5.0 GeV/c^2

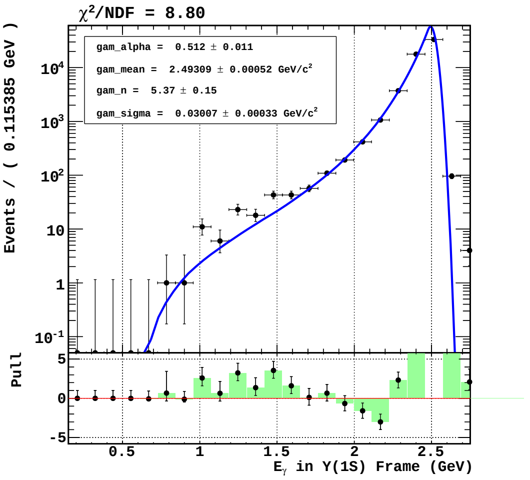

(g) M_{A^0} = 6.5 GeV/c^2

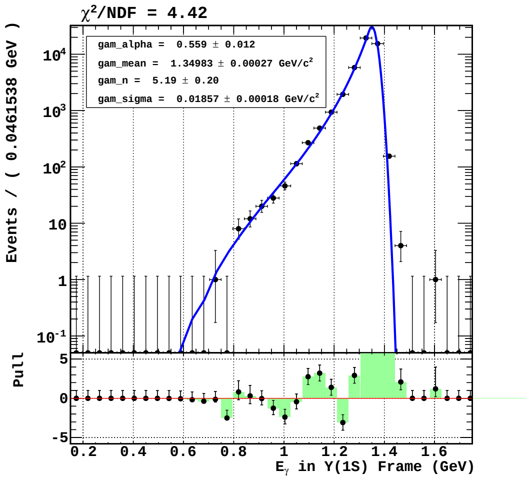

(h) M_{A^0} = 8.0 GeV/c^2

C.2. Off-shell signal sample

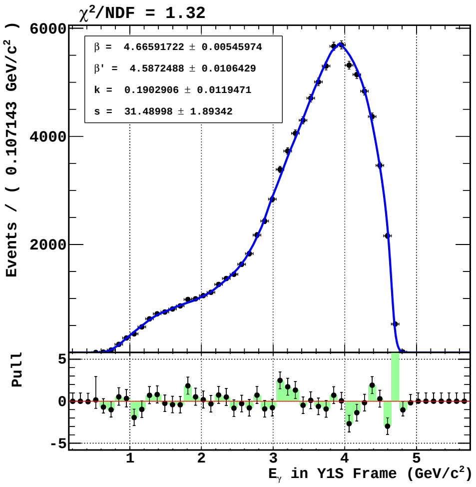

(a) M_χ = 0.5 GeV/c^2

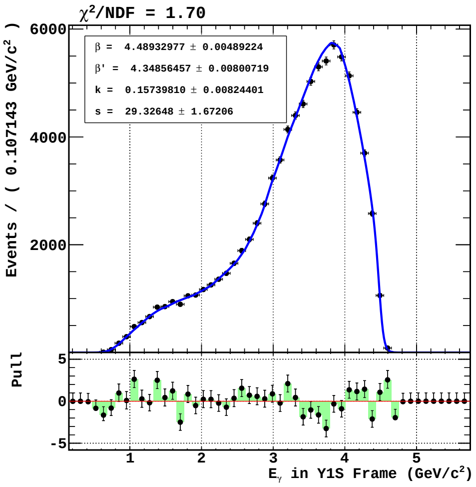

(b) M_χ = 1.0 GeV/c^2

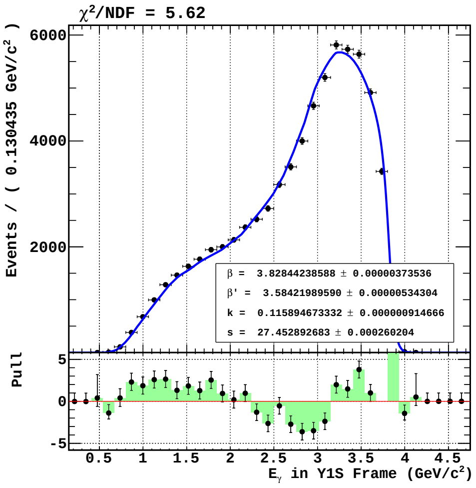

(c) M_χ = 2.0 GeV/c^2

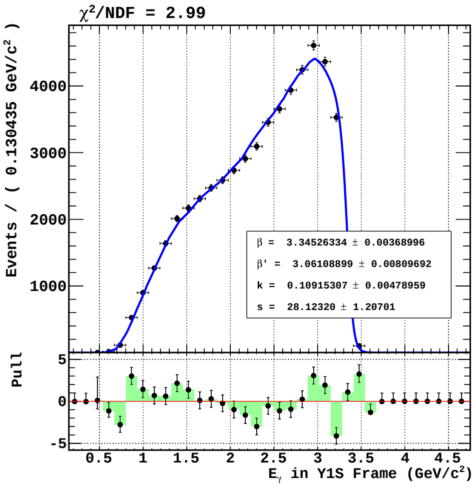

(d) M_χ = 2.5 GeV/c^2

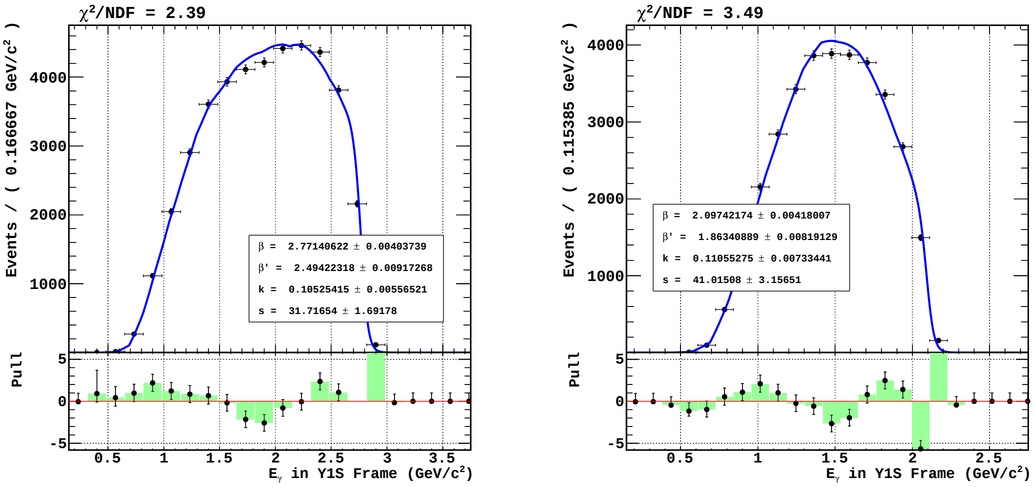

(e) M_χ = 3.0 GeV/c^2

(f) M_χ = 3.5 GeV/c^2

Figure C.-2.: Photon energy spectrum with the final PDF for the off-shell production

Appendix D

Results of fit bias test

Results of fit bias as a function of N_{sig} at each signal mass are present here. Red lines are fitted line with a constant function. The results of constant functions are used to obtain average fit bias.

D.1. Fit bias for the on-shell signal

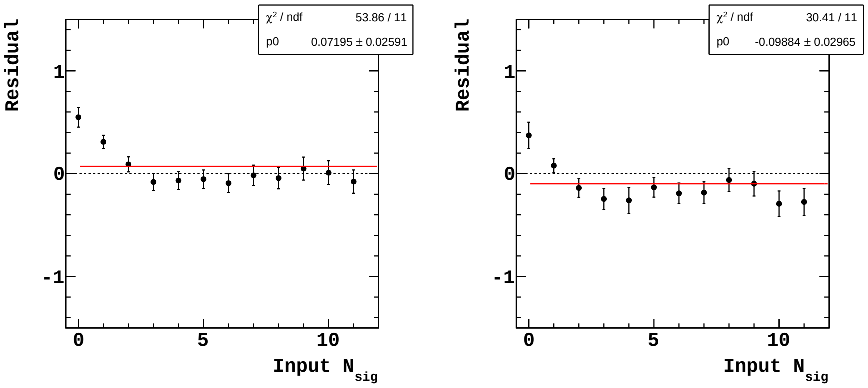

(a) $M_{A^0} = 0.5$ GeV (b) $M_{A^0} = 3.0$ GeV

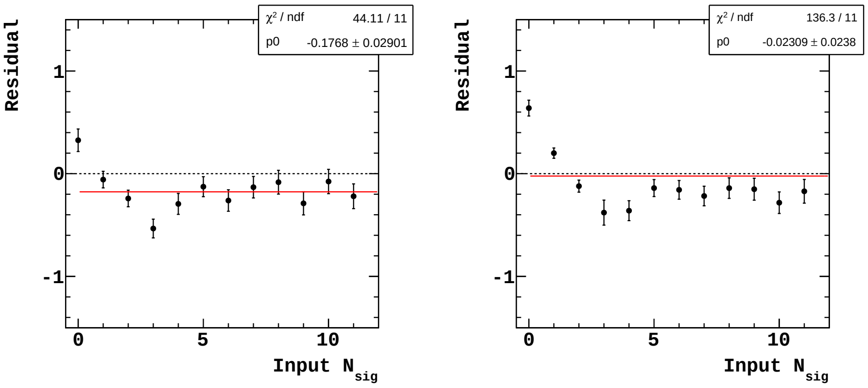

(c) $M_{A^0} = 4.5$ GeV (d) $M_{A^0} = 6.0$ GeV

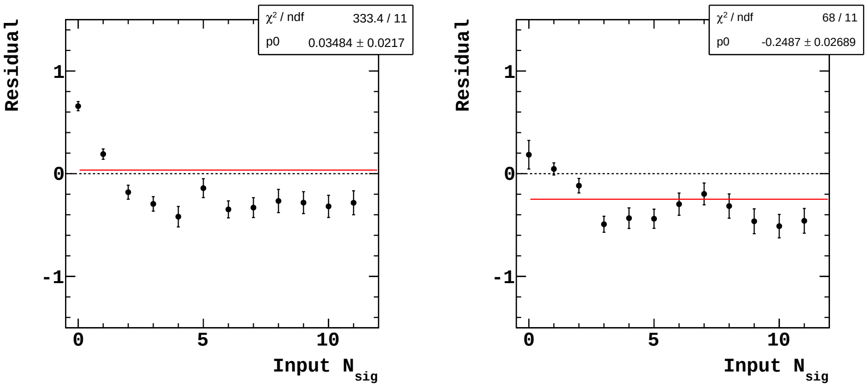

(e) $M_{A^0} = 7.0$ GeV (f) $M_{A^0} = 8.0$ GeV

Figure D.1.: Results of toy MC for the on-shell signal

D.2. Fit bias for the off-shell signal

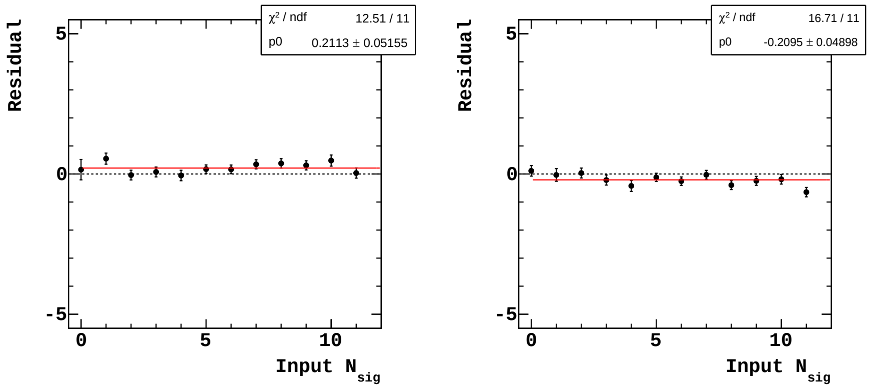

(a) M_χ = 0.5 GeV (b) M_χ = 1.5 GeV

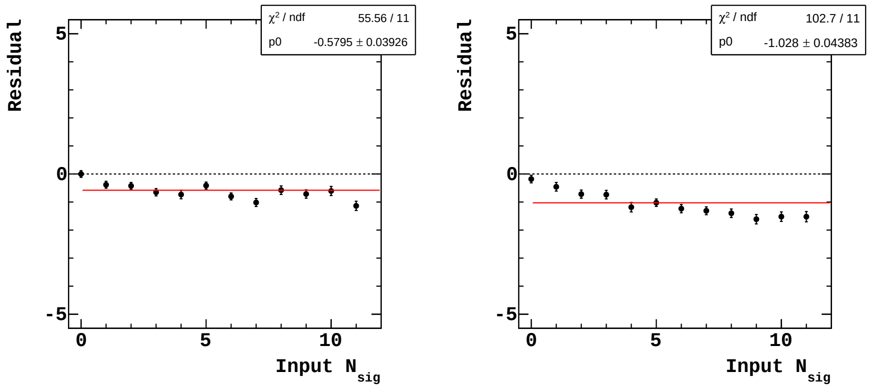

(c) M_χ = 2.5 GeV (d) M_χ = 3.0 GeV

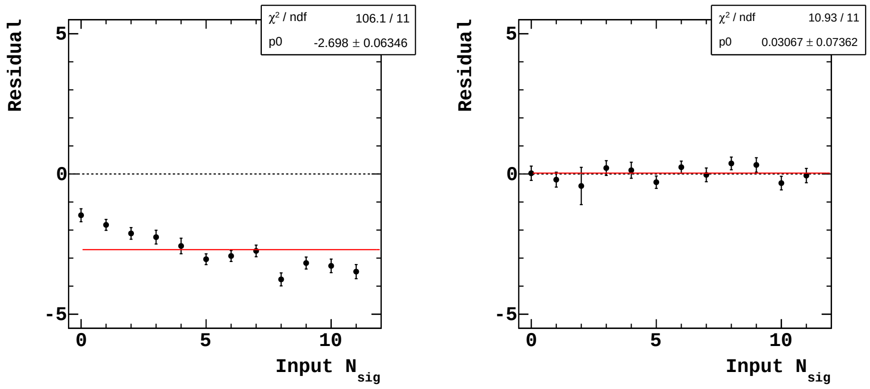

(e) M_χ = 3.5 GeV (f) M_χ = 4.0 GeV

Figure D.2.: Results of toy MC for the off-shell signal

Bibliography

[1] F. Zwicky, Helv. Phys. Acta 6, 110 (1933), [Gen. Rel. Grav.41,207(2009)].

[2] K. G. Begeman, A. H. Broeils, and R. H. Sanders, Mon. Not. Roy. Astron. Soc. 249, 523 (1991).

[3] D. Clowe *et al.*, Astrophys. J. 648, L109 (2006), astro-ph/0608407.

[4] Planck, P. A. R. Ade *et al.*, Astron. Astrophys. 594, A13 (2016), 1502.01589.

[5] Planck, P. A. R. Ade *et al.*, Astron. Astrophys. 571, A16 (2014), 1303.5076.

[6] K. Griest, Astrophys. J. 366, 412 (1991).

[7] T. D. Brandt, Astrophys. J. 824, L31 (2016), 1605.03665.

[8] K. Griest, A. M. Cieplak, and M. J. Lehner, Astrophys. J. 786, 158 (2014), 1307.5798.

[9] S. Dodelson and L. M. Widrow, Phys. Rev. Lett. 72, 17 (1994), hep-ph/9303287.

[10] L. Bergstrom, New J. Phys. 11, 105006 (2009), 0903.4849.

[11] R. D. Peccei and H. R. Quinn, Phys. Rev. Lett. 38, 1440 (1977).

[12] R. D. Peccei and H. R. Quinn, Phys. Rev. D16, 1791 (1977).

[13] J. E. Kim, Phys. Rev. Lett. 43, 103 (1979).

[14] M. A. Shifman, A. I. Vainshtein, and V. I. Zakharov, Nucl. Phys. B166, 493 (1980).

[15] M. Dine, W. Fischler, and M. Srednicki, Phys. Lett. B104, 199 (1981).

[16] A. R. Zhitnitsky, Sov. J. Nucl. Phys. 31, 260 (1980), [Yad. Fiz.31,497(1980)].

[17] J. E. Kim and G. Carosi, Rev. Mod. Phys. 82, 557 (2010), 0807.3125.

[18] J. L. Feng, Ann. Rev. Astron. Astrophys. 48, 495 (2010), 1003.0904.

[19] G. Jungman, M. Kamionkowski, and K. Griest, Phys. Rept. 267, 195 (1996), hep-ph/9506380.

[20] DAMA, R. Bernabei *et al.*, Eur. Phys. J. C56, 333 (2008), 0804.2741.

[21] CoGeNT, C. E. Aalseth *et al.*, Phys. Rev. D88, 012002 (2013), 1208.5737.

[22] G. Angloher *et al.*, Eur. Phys. J. C72, 1971 (2012), 1109.0702.

[23] CDMS, R. Agnese *et al.*, Phys. Rev. Lett. 111, 251301 (2013), 1304.4279.

[24] XENON, E. Aprile *et al.*, (2017), 1705.06655.

[25] LUX, D. S. Akerib *et al.*, Phys. Rev. Lett. 118, 021303 (2017), 1608.07648.

[26] PICO, C. Amole *et al.*, Phys. Rev. Lett. 118, 251301 (2017), 1702.07666.

[27] Super-Kamiokande, K. Choi *et al.*, Phys. Rev. Lett. 114, 141301 (2015), 1503.04858.

[28] IceCube, R. Abbasi *et al.*, Phys. Rev. D85, 042002 (2012), 1112.1840.

[29] ATLAS, G. Aad *et al.*, Phys. Rev. D91, 012008 (2015), 1411.1559, [Erratum: Phys. Rev.D92,no.5,059903(2015)].

[30] ATLAS, G. Aad *et al.*, Eur. Phys. J. C75, 299 (2015), 1502.01518, [Erratum: Eur. Phys. J.C75,no.9,408(2015)].

[31] CMS, V. Khachatryan *et al.*, Phys. Lett. B755, 102 (2016), 1410.8812.

[32] CMS, V. Khachatryan *et al.*, Eur. Phys. J. C75, 235 (2015), 1408.3583.

[33] N. Fernandez, J. Kumar, I. Seong, and P. Stengel, Phys. Rev. D90, 015029 (2014), 1404.6599.

[34] N. Fernandez, I. Seong, and P. Stengel, Phys. Rev. D93, 054023 (2016), 1511.03728.

[35] CMS, S. Chatrchyan *et al.*, Phys. Lett. B716, 30 (2012), 1207.7235.

[36] ATLAS, G. Aad *et al.*, Phys. Lett. B716, 1 (2012), 1207.7214.

[37] S. P. Martin, (1997), hep-ph/9709356, [Adv. Ser. Direct. High Energy Phys.18,1(1998)].

[38] R. Dermisek and J. F. Gunion, Phys. Rev. Lett. 95, 041801 (2005), hep-ph/0502105.

[39] R. Dermisek and J. F. Gunion, Phys. Rev. D75, 075019 (2007), hep-ph/0611142.

[40] ALEPH, S. Schael *et al.*, JHEP 05, 049 (2010), 1003.0705.

[41] BaBar, B. Aubert *et al.*, Phys. Rev. Lett. 103, 181801 (2009), 0906.2219.

[42] BaBar, B. Aubert *et al.*, Phys. Rev. Lett. 103, 081803 (2009), 0905.4539.

[43] BaBar, J. P. Lees *et al.*, Phys. Rev. D88, 071102 (2013), 1210.5669.

[44] BaBar, J. P. Lees *et al.*, Phys. Rev. D87, 031102 (2013), 1210.0287, [Erratum: Phys. Rev.D87,no.5,059903(2013)].

[45] R. Dermisek and J. F. Gunion, Phys. Rev. D81, 075003 (2010), 1002.1971.

[46] J. F. Gunion, D. Hooper, and B. McElrath, Phys. Rev. D73, 015011 (2006), hep-ph/0509024.

[47] D. B. Kaplan, Phys. Rev. Lett. 68, 741 (1992).

[48] D. E. Kaplan, M. A. Luty, and K. M. Zurek, Phys. Rev. D79, 115016 (2009), 0901.4117.

[49] K. Petraki and R. R. Volkas, Int. J. Mod. Phys. A28, 1330028 (2013), 1305.4939.

[50] P. Fayet, Phys. Rev. D74, 054034 (2006), hep-ph/0607318.

[51] G. K. Yeghiyan, Phys. Rev. D80, 115019 (2009), 0909.4919.

[52] R. Dermisek, J. F. Gunion, and B. McElrath, Phys. Rev. D76, 051105 (2007), hep-ph/0612031.

[53] CLEO, R. Balest *et al.*, Phys. Rev. D51, 2053 (1995).

[54] BaBar, P. del Amo Sanchez *et al.*, Phys. Rev. Lett. 107, 021804 (2011), 1007.4646.

[55] BaBar, B. Aubert *et al.*, Search for Invisible Decays of a Light Scalar in Radiative Transitions $\upsilon_{3S} \to \gamma$ A0, in *Proceedings, 34th International Conference*

on High Energy Physics (ICHEP 2008): Philadelphia, Pennsylvania, July 30-August 5, 2008, 2008, 0808.0017.

[56] S. Kurokawa and E. Kikutani, Nucl. Instrum. Meth. A499, 1 (2003).

[57] T. Abe *et al.*, PTEP 2013, 03A001 (2013).

[58] D. Besson and T. Skwarnicki, Ann. Rev. Nucl. Part. Sci. 43, 333 (1993).

[59] A. Abashian *et al.*, Nucl. Instrum. Meth. A479, 117 (2002).

[60] Belle, Y. Ushiroda *et al.*, Nucl. Instrum. Meth. A438, 460 (1999).

[61] D. J. Lange, Nucl. Instrum. Meth. A462, 152 (2001).

[62] R. Brun, F. Bruyant, M. Maire, A. C. McPherson, and P. Zanarini, (1987).

[63] Belle, X. Wang, Belle Note 1185 (2011).

[64] Belle, W. Dungel, Belle Note 1176 (2011).

[65] Belle, B. Bhuyan, Belle Note 1165 (2010).

[66] Belle, N. J. K. Trabelsi and T. Aziz, Belle Note 995 (2010).

[67] C. Kelso, J. Kumar, P. Sandick, and P. Stengel, Phys. Rev. D91, 055028 (2015), 1411.2634.

[68] LUX, D. S. Akerib *et al.*, Phys. Rev. Lett. 112, 091303 (2014), 1310.8214.

[69] CRESST, G. Angloher *et al.*, Eur. Phys. J. C76, 25 (2016), 1509.01515.

[70] SuperCDMS, R. Agnese *et al.*, Phys. Rev. Lett. 112, 241302 (2014), 1402.7137.

[71] C. E. Aalseth *et al.*, (2014), 1401.6234.

[72] C. Savage, G. Gelmini, P. Gondolo, and K. Freese, JCAP 0904, 010 (2009), 0808.3607.

[73] PICASSO, S. Archambault *et al.*, Phys. Lett. B711, 153 (2012), 1202.1240.